**Title**
Principle and applications of quantum metrology in diamond anvil cells using the Nitrogen Vacancy color center



**Author**
Bhattacharyya, Prabudhya

**Publication Date**
2022

Peer reviewed|Thesis/dissertation

# Principle and applications of quantum metrology in diamond anvil cells using the Nitrogen Vacancy color center

by

Prabudhya Bhattacharyya

A dissertation submitted in partial satisfaction of the

requirements for the degree of

Doctor of Philosophy

in

Physics

in the

Graduate Division

of the

University of California, Berkeley

Committee in charge:

Professor Norman Yao, Chair
Professor Raymond Jeanloz
Professor Joel Moore

Fall 2022

Principle and applications of quantum metrology in diamond anvil cells using the Nitrogen Vacancy color center

Abstract

Principle and applications of quantum metrology in diamond anvil cells using the Nitrogen Vacancy color center

by

Prabudhya Bhattacharyya

Doctor of Philosophy in Physics

University of California, Berkeley

Professor Norman Yao, Chair

Tuning pressure using diamond anvil cells (DACs) provides an interesting playground for exploring novel condensed phases and understanding important geophysical processes. However, the extension of conventional probes for materials characterization to extreme pressure environments is often constrained by large stress gradients and limited signal strengths. Here, I outline a novel platform for high pressure metrology in DACs based on the Nitrogen Vacancy (NV) color center in diamond. By integrating the NV center, a robust and versatile quantum sensor, directly into the diamond culet, we demonstrate *in situ* vector magnetometry and tensorial stress imaging with high sensitivity and diffraction-limited sub-micron spatial resolution. Proof of principle measurements demonstrate the platform's versatility by imaging the dipole strength of Iron (Fe) across the $\alpha \leftrightarrow \epsilon$ structural transition, mapping the full stress tensor across the culet surface, and exploring the pressure-temperature phase diagram of gadolinium (Gd). Applying this technique in synergy with piezoelectric displacement sensing and X-ray diffraction (XRD) to study the amorphization of chrysotile Serpentine, we observe phase transformational nanoseismicity driven by shear stress - a possible mechanism underpinning deep earthquakes. Furthermore, we explore surprising qualitative changes in the behavior of the NV center up to megabar pressures, motivating further studies to understand the spin-orbit, and spin-spin coupling in the excited electronic state and the inter-system crossing mechanism. We demonstrate the viability of using the NV center as a robust pressure calibrant capable of easily measuring spatial gradients in multiple stress components. By playing with different crystal cuts of diamond anvils, we extend continuous wave and pulsed NV sensing to pressures nearing $\sim 150\,\mathrm{GPa}$ achieving excellent signal contrast and sensitivity. Finally, we use simultaneous transport measurements and NV magnetometry to probe the dual hallmarks superconductivity in a superhydride material at megabar pressures. Our work constitutes the first spatially resolved measurement of the Meissner effect and provides clear evidence of flux trapping in these novel compounds.

To my family,
near and far

# Contents

**Contents** **ii**

**List of Figures** **iv**

**1 The NV center in diamond** **1**
1.1 Description . . . . . 1
1.2 Physics of the NV center . . . . . 3
1.3 Measurements using the NV center . . . . . 11
1.4 NV sensing: Vector Magnetometry . . . . . 13
1.5 What is this thesis about? . . . . . 15

**2 The diamond anvil cell** **16**
2.1 A (very) brief history . . . . . 16
2.2 The design of a diamond anvil cell . . . . . 18
2.3 The apparatus of high pressure NV experiments . . . . . 19
2.4 Using high-pressure tools... . . . . 25

**3 NV sensing at high pressure: proof of principle** **26**
3.1 Stress Response of the NV center . . . . . 26
3.2 Early promise . . . . . 28
3.3 Other Techniques . . . . . 37
3.4 Looking forward . . . . . 38

**4 The NV center at ambient conditions: strain and electric fields** **40**
4.1 NV spectra at $B = 0$ . . . . . 41
4.2 Intrinsic electric fields in bulk diamonds . . . . . 42
4.3 Vector imaging electric fields in single NV centers . . . . . 44
4.4 Conclusion . . . . . 46

**5 Imaging stress across nanoseismic faulting events in chrysotile Serpentine** **47**
5.1 Deep Earthquakes . . . . . 47
5.2 Displacement sensing of nanoseismic events . . . . . 48

5.3 XRD characterization of failure mechanims . . . . . 51
5.4 The role of stress in sample failure and nanoseismicity . . . . . 53
5.5 Conclusion . . . . . 63

**6 The road to megabar pressures** **64**
6.1 Microdiamonds in hydrostatic pressure . . . . . 65
6.2 Sensing with a [100] cut culet . . . . . 67
6.3 Positive Contrast . . . . . 70
6.4 The home run... . . . . . 74
6.5 The road ahead... . . . . . 76

**7 Imaging magnetism in hydride superconductors at megabar pressures** **79**
7.1 Sample preparation . . . . . 81
7.2 Experimental setup . . . . . 84
7.3 Magnetism in a hydride superconductor . . . . . 88
7.4 Conclusion . . . . . 97

**8 Next steps...** **99**

**Bibliography** **101**

# List of Figures

1.1 **NV center in diamond:** (a) A ball and stick diagram of the NV center. The repeating tetrahedra of carbon atoms (grey) form the diamond lattice. The NV center comprises a substitutional nitrogen atom (blue) adjacent to a vacant lattice site (shown with a broken line) (b) One of the defining properties of the NV center is its fluorescence. A diamond rich in NV centers glows bright red, as the sample shown in this picture. . . . . 2

1.2 **NV orbitals and level structure:** (a) A diagram of the NV center showing the Nitrogen orbital ($\sigma_N$) with an electron lone pair (black dots) and the dangling bonds of the Carbon atoms ($\sigma_i$) with one electron each. The NV orbitals are built out of linear combinations of the four atomic orbitals and populated by a total of six electrons for the $NV^-$ center. The additional electron gained from the lattice is shown near the vacant site. (b) In the ground state of the $NV^-$, the degenerate $|e_x\rangle$ and $|e_y\rangle$ orbitals are each populated by one electron. Together they form an orbital singlet spin triplet state to minimize the coulomb interaction energy of the two electrons. Therefore, the ground state of the NV center is spin 1. The energies of the NV orbitals relative to the band structure of the diamond are shown [29]. (c) In the electronic excited state of the $NV^-$ center, an electron may be promoted from the $|a_1\rangle$ orbital to either of the $|e_{x,y}\rangle$ orbitals. As a result, there are six possible states in this manifold ($^3E$). . . . . 4

1.3 **NV ground state spin:** (a) The coordinate system associated with the NV center showing the quantization axis of the electronic spin. The NV center is symmetric with respect to 120° rotations around the $\hat{z}$ axis, and the reflections across planed formed by the Nitrogen-Vacancy-Carbon lattice points. The ground state $|e_x\rangle$ and $|e_y\rangle$ orbitals are linear combinations of the Carbon dangling bonds. Therefore, the ground state electronic configuration is dominantly distributed across the planar region formed by the carbon orbitals with their spin oriented along the $\hat{z}$ axis. As a consequence, when the spins are aligned ($|m_s = \pm 1\rangle$ states), their dipole-dipole interaction energy is higher than when they are anti-aligned. (b) The ground state spin sublevels are split by $D_{gs} \approx (2\pi) \times 2.87\,\text{GHz}$ GHz with the $|m_s = \pm 1\rangle$ states being degenerate to each other. Given that $D_{gs}$ corresponds to a temperature of 140 mK, the ground state spins are fully mixed at room temperature with 1/3 of the population in each spin state. The ground state hamiltonian is $H = D_{gs} S_z^2$ where $D_{gs}$ is called the zero-field splitting.
**Note:** I will use lower case $(\hat{x}, \hat{y}, \hat{z})$ to refer to the reference frame of the NV center and upper case $(\hat{X}, \hat{Y}, \hat{Z})$ to refer to the lab frame. This will be important in the discussion of stress sensing and vector magnetometry. In some cases, the two reference frames are coincident, but this may not be true in general. . . . . 6

1.4 **NV ISC mechanism:** Electrons in the ground $^3A_2$ state are off-resonantly excited using a 532 nm beam to the $^3E$ excited state. The excited state has a lifetime of $\sim 10$ ns at cryogenic temperature, and the electrons can fluoresce back into a ground state, releasing a red photon (637−900 nm). For the $|^3E,\, m_s = \pm 1\rangle$ states, complementary to this radiative spin conserving process, the electron can non-radiatively transition into the $^1A_1$ state in the singlet manifold. An additional fluorescence line at 1024 nm in the singlet manifold is filtered out in the experiments. The branching ratio of the second non-radiative relaxation path from the single $^1E$ states back to the ground state marginally favors the electronic population in the $|^3A_2\, m_s = 0\rangle$ state. The microscopic mechanism for this process is believed to be due to a stimulated phonon emission process [100]. This intersystem crossing mechanism, occurring over a timescale of $\sim 300$ ns, is crucial for optical pumping and spin state readout of the NV center. In addition to optical transitions, the NV center also shows ground-state spin coherence. Using MW radiation, we can induce coherent oscillations among the $|^3A_2, m_s\rangle$ spin states (blue dashed arrow) - a mainstay of the NV center's room temperature quantum applications. . . . . 8

1.5 **Schematic of a confocal NV fluorescence microscope:** The beam of a 532 nm laser (Coherent Compass 315M or Coherent Verdi V-2), switched by a double pass AOM (Gooch & Housego AOMO 3110-120) setup, is directed towards a pair of scanning galvo mirrors (Thorlabs GVS212) using a dichroic beamsplitter (Semrock FF552-Di02). Following the galvo, a $4f$ telescope comprising two converging lenses is used to focus the excitation beam (green) onto the rear window of a high NA objective lens (typically a Mitutoyo M Plan APO long working distance objective). The voltage-controlled galvo mirrors raster the excitation beam in XY while the $4f$ system fixes the focus of the beam at the objective entrance enabling one to scan the excitation laser over the sample region. Scanning in the Z axis is enabled by a piezo objective mount (Edmond Optics nanopositioning piezo actuator) with 100 $\mu$m range. The NV fluorescence (red beam) at the sample captured over some solid angle by the objective counter propagates along the excitation path. The dichroic beam splitter transmits the fluorescence beam, and additional filters are used to chop out parasitic excitation photons and $NV^0$ fluorescence. The fluorescence beam is then coupled to a fiber (the fiber core acts as the pinhole in our confocal setup). In all experiments, a single photon counter (Excelitas SPCM-AQRH-64-FC) was used to measure the fluorescence signal. (bottom left) A sample NV fluorescence scan of a pressure loading is shown. One can clearly see the culet and facets of the diamond anvil as well as the sample chamber and ruby pressure marker. White scale bar shows 100 µm. 10

1.6 **MW setup**: A microwave signal generator (SRS SG386 or SG384) is used for both pulsed and continuous wave experiments. A MW switch (Minicircuits ZASWA-2-50DR) is used to shutter any spurious leakage in the MW channel. A high-power class A amplifier (Minicircuits ZHL-15W-422-S+) is used to amplify the MW prior to channeling the radiation to the NV sample. Downstream from the sample, a 50Ω terminated high power attenuator (Minicircuits BW-N40W50+) is used to absorb the MW signal to prevent any reflection back to the sample. . . . . 11

1.7 **NV measurements at $\sim$ 120 GPa:** (a) A room temperature cwODMR spectrum at high pressure showing the resonances between the ground state $|m_s = 0\rangle$ and $|m_s = \pm 1\rangle$ states. The $|m_s = \pm 1\rangle$ states are shifted, split, and mixed due to crystal stress. (b) A low-temperature Rabi measurement at the same pressure: The pulse sequence for a Rabi experiment (inset) starts with a polarization pulse to prepare the NV center in the $|m_s = 0\rangle$ state. Following a short wait time, a MW pulse at the resonance frequency is applied for a variable time. A state readout pulse shows rabi oscillations as a function of the length of the MW pulse. A second reference readout pulse (not shown) can control for drift in NV counts over the course of the data taking. . . . . 13

1.8 **Vector magnetometry:** There are four groups of NV centers in diamond with the N-V axis oriented along each of the four diamond bonds. The ground state spin of each group is quantized along its respective NV axes ($\hat{z}$). In this figure, the four groups are depicted in terms of their crystal orientation (top). The application of a generic $\vec{B}$ field (shown in the crystal frame on the top left) will result in eight resonance lines (two for each NV group) in a cwODMR spectrum. This is because the magnitude of the field projection in the frame of each NV group will determine the shift and splitting of these lines. In the ODMR spectrum, the lines from each group are paired and denoted by the color associated with each group. The four groups are ordered according to the magnitude of the field projection in their respective frames. . . . . 14

2.1 **Valkenburg's original pictures of DAC loadings (images adapted from [12])**: (a) A loading of copper bromide nucleation of a high pressure phase (dark). (b) A pressure loading with water at room temperature showing an octahedron phase of ice VI. . . . . 17

2.2 **DAC design:** (a) A standard gem cut diamond anvil showing the base (table side) and a flat culet. Most of our experiments used this kind of anvil design with 200 $\mu$m culets with 16 facets. At its widest, the girdle of the diamond anvil can be $\sim$ 3.25 mm. (b) A cartoon of a DAC loading with two opposing anvils and a gasket. The diamonds are glued to backing plates (seats) and subsequently aligned with the cell body of the DAC (not shown). An optical window allows us to perform confocal scanning through the table side of the diamonds. (c) a Pasternak DAC showing two plates with guiding rods and a cubic boron nitride (black) backing plate at the center. (d) 10 mm and 17 mm PPMS DACs designed by Viktor Struzhkin and Alex Gavriliuk [41] (c) a BeCu mini BX90 cell [56] showing the cylinder (left) and piston (right). Diamond anvils are glued to backing plates in both parts . . . . . 19

2.3 **Gluing anvils**: (Left) An Almax Diacell easyGlue jig holding a cubic boron nitride (cBN) backing plate and a diamond anvil. (Right) The optical window of the backing plate is aligned to the diamond culet using the four adjustment screws of the jig. To avoid parallax, we iteratively rotate the jig by 90° and vertically center the culet on the optical window. Even after full alignment, parallax in the microscope does not show the culet and window aligned along the horizontal axis. The diamond is glued to the backing plate by applying Stycast® 2850 FT around the table side of the anvil after alignment. . . . . 20

2.4 **Culet Alignment:** (a) The cylinder (left) and piston (right) of the mini BX90 cell show anvils glued to the cBN backing plates. (b) Closing the cell *very carefully*, we can inspect from the side to check for positional alignment of the culet. Diamond contact at this step can easily cause the culets to crack. (c) Inspecting through the optical window shows two misaligned culets. One can perform positional alignment by moving the *bottom* culet. (d) Two culets aligned in position and parallelism, as evidenced by a single interference fringe spread out over the culet. . . . . 21

2.5 **Making insulating gaskets:** (a) A Rh foil is first pre-indented up to $\sim 30\,\mathrm{GPa}$. (b) The majority ($\sim 90\%$) of the culet area is drilled to avoid shorting under high pressure due to gasket flow. (c) The sample chamber is then packed with a powdered mixture of cBN (LANDS Superabrasives, Co.) and epoxy (EPO-TEK® 353 ND/A). This mixture is prepared by combining $2 \times 10^6$ mesh powdered cBN with epoxy in a $4:1$ ratio by mass. The dried paste is subsequently powdered in a mortar and pestle. (d) The mixture is compressed to $\sim 30\,\mathrm{GPa}$, and the sample chamber is punched out using a laser drill. . . . . 22

2.6 **MW delivery:** (Left) In our loadings, we used a wire cut out of $4\,\mu\mathrm{m}$ platinum (Pt) foil. The wire was draped over the anvil facets as close as possible to the sample chamber. The two ends of the wire were soldered to brass pins glued to the backing plate. Insulated copper (Cu) magnet wires were used to connect these pins to coax (SMA) cables for MW delivery to the DAC. (Right) For performing pulsed measurements, it is imperative to have MW wires as close as possible to the target NV centers in the sample chamber. . . . . 23

2.7 **Loading with salt:** Although fairly straightforward, loading with salt proved to be tricky for me in my first few attempts. The trick, as shown by Dr. Zachary Geballe, is outlined above. (a) A piece of salt roughly $\sim 80\%$ of the volume of the sample chamber is used. Filling the chamber with salt can cause the gasket to flow outward under pressure leading to the expansion of the sample chamber and failure of the pressure loading. Instead, this technique ensures the gasket flows inward, maintaining the integrity of the sample chamber. (b) The metalization of cesium iodide (CsI) can lead to absorption of $532\,\mathrm{nm}$ excitation light above $\sim 50\,\mathrm{GPa}$. Under white light illumination, the sample chamber appears red because of the absorption of short wavelengths at the onset of metalization. . . 24

2.8 **Crystal cut of culet [75]:** The three main crystal cuts for diamond anvils are shown along with the orientation of the four NV groups therein. As a convention in this thesis, $\{\hat{X}, \hat{Y}, \hat{Z}\}$ represents the lab frame, whereas $\{\hat{x}, \hat{y}, \hat{z}\}$ represents the reference frame of a single NV group. The $\hat{Z}$ axis in the lab frame is the loading axis in all cases. In each case, the local frame $\{\hat{x}, \hat{y}, \hat{z}\}$ of one of the NV groups is shown. (a) In a [100] cut anvil, the four NV groups are degenerate with respect to the loading axis. (b) In a [110] cut anvil, two sets of NV groups are each doubly degenerate with respect to the loading axis. One set is oriented in the plane of the culet, whereas another set projects strongly on the loading axis. (c) In a [111] cut culet, one NV group is fully oriented along the loading axis. Note that the local frame of this [**111**] **NV group** is coincident with the lab frame. The other three NV groups are degenerate with respect to the loading axis.
**Note:** The [100], [110] and [111] directions are represented in the crystal frame of diamond which is not shown in this figure. . . . . 25

3.1 **Stress coupling of the NV center:** A symmetry preserving stress (left) shown as a compression along the N-V axis shifts the NV resonance line. In contrast, a symmetry breaking stress (right) shown as a bending of a carbon dangling bond lifts the degeneracy of the $|m_S = \pm 1\rangle$ states and splits the NV resonance line. In addition, the admixture of the $|m_S = \pm 1\rangle$ states under a symmetry breaking stress can have different transition matrix elements with the $|m_S = 0\rangle$ state under linearly polarized microwave radiation. . . . . 28

3.2 **Imaging local magnetic fields under high pressure [49]:** (a) A schematic of the loading showing a ruby pressure marker, the iron pellet, and a layer of NV centers 50 nm below the culet surface. In the presence of an applied external field $H_{ext} \sim 180\,\mathrm{G}$, the magnetic domains of $\alpha$-Iron roughly align to the field to yield a dipole field pattern (shown in broken black arrows). (b) A white light microscope image of the Iron pellet (scale bar on the bottom left shows 10 µm). (c) At each point of this image, we can take a cwODMR spectrum to determine the local magnetic field. The projection of the local field in the frame of the four NV groups determines the magnitude of the splitting and shifting of their resonances. **Note:** The spectrum shown is a sample cwODMR resonance and is not belong to this data set. (d) By taking a line cut along the vertical (white broken line in (b)) we can follow the change in the NV resonances with position to make a map of the local field. . . . . 29

3.3 **Reconstructing the dipole field of Iron [49]:** Following the procedure in Fig. 3.2 (d), we can map out the NV resonances over the sample region (a). (b) Fitting to the local magnetic field, we directly see a dipole field pattern around the location of the pellet. Directly on top of the Iron pellet (black pixels), cwODMR resonances are obscured due to large field gradients. (c) Nevertheless, the obtained field pattern can be fit to a point dipole model to fully reconstruct the field over the sample region (see section 5.2 of supplementary information in [49] for full details). . . . . 30

3.4 **Structural transition between $\alpha \leftrightarrow \epsilon$ Iron [49]:** Mapping out the dipole pattern at each pressure point on both compression and decompression we can quantitatively ascertain the dipole strength of the Iron sample under pressure. (a) cwODMR data taken along a line cut in the sample area (black broken line in (b)) at three demonstrative pressure points on compression. The spatial variation of the local magnetic field diminishes on compression from 9.6 GPa to 17.2 GPa and effectively disappears at 20.2 GPa. (b) Extracted dipole maps show a marked reduction in dipole field strength with increasing pressure. (c) A plot of the dipole strength against applied pressure (measured using ruby fluorescence) shows a clear transition from $\alpha \rightarrow \epsilon$ with the onset at $\sim$ 15 GPa and completion at $\sim$ 22 GPa. On decompression, the transition from $\epsilon \rightarrow \alpha$ iron shows and onset at $\sim$ 15 GPa and completion at $\sim$ 9 GPa. The pressure gradients in the sample chamber exacerbate the intrinsic hysteresis associated with this first-order structural transition. **Note:** The large error bar associated with the decompression pressure point at 11 GPa is due to relaxation in the sample chamber during data acquisition. A drift pressure in the chamber resulted in a significant change in the sample dipole moment. . . . . 31

3.5 **Gadolinium (Gd) loading [49]:** (a) Fluorescence scan showing a Gd sample and ruby pressure marker. cwODMR from culet NVs were taken at a 'probe' point close to the Gd sample. A 'control' point further away from the sample was used to monitor changes in the applied background magnetic field. White scale bar shows 50 µm. (b) On cooling below the Curie temperature with an applied background field, we notice a dramatic increase in the splitting at the probe point suggesting a contribution to the local magnetic field from the ferromagnetic ordering in hcp-Gd. In contrast, we observe no change at the control point. . . 32

3.6 **Probing structural and magnetic transitions in Gd [49]:** (a) Profile of the Curie transition in hcp-Gd shows a decreasing transition temperature with an increase in pressure. Inset shows no perceptible hysteresis associated with this transition at 0.5 GPa consistent with its second order nature. (b) A path in the $PT$ phase diagram (dark blue) starting in the hcp structural phase at near $\sim 2$ GPa shows a clear increase in splitting at the Curie transition point. However, increasing pressure on further cooling results in an abrupt loss of ferromagnetic signal at $\gtrsim 6$ GPa suggesting a structural transition into the dhcp phase. Retracing the $PT$ path after this change in crystal structure into the dhcp phase (red and light blue) shows no recovery of the ferromagnetic signal underpinning the metastability of the dhcp phase on quenching pressure. However, the signal associated with magnetic ordering in the hcp phase is recovered if the dhcp phase boundary at $\sim 6$ GPa is not crossed (inset). . . . . 33

3.7 $PT$ **phase diagram of Gadolinium [49]:** Each cooldown takes a diagonal path through the $PT$ phase space. [a] The curie transition in hcp-Gd (red squares) is observed well beyond the boundary of the hcp and Sm-type structural phases suggesting sluggish transition dynamics between these two crystal structures. [b] Starting in the paramagnetic hcp phase, we observe a Curie transition followed by a complete loss of magnetic signal at the boundary of the dhcp crystal phase (detailed in Fig. 3.6 (b)). Significantly weaker signals are obtained in the transition from the paramagnetic Sm-type to paramagnetic dhcp-Gd (orange diamonds in [c]) and the Neel transition within the Sm-type phase (green triangle in [d]). The magnetic phase boundaries within the Sm-type and dhcp structural phases are taken from [87]. . . . . 34

3.8 **Imaging Culet stress [49]:** Maps of the uniaxial $\sigma_{ZZ}$ stress (left) and the biaxial $\sigma_{\perp} = (\sigma_{XX} + \sigma_{YY})/2$ (right) in a [111] cut culet. The outer region shows stress at the gasket and the inner region shows stress within the sample chamber when using 16:3:1 methanol/ethanol/water pressure medium. The ruby pressure of 4.9 GPa agrees closely with the $\sigma_{ZZ}$ stress value in the sample chamber. A linecut of the stress (along the white broken line in the culet) is shown at the bottom. The $\sigma_{ZZ}$ and $\sigma_{\perp}$ stress profiles are qualitatively different. We observed a uniform stress profile in the former case due to a quasihydrostatic pressure medium. In the latter case, we observe a convex spatial profile due to the 'cupping' of the diamond culet. In both cases, finite element simulations (broken lines) fit the measured stress. . . . . 35

3.9 **Glass transition in Methanol/Ethanol/Water [49]:** A comparison of all six stress components is plotted along a linecut in the sample chamber region for two pressure points (denoted by the ruby pressures of 4.9 GPa and 13.6 GPa). The right inset shows a comparison of the $\sigma_{ZZ}$ stress below and above the glass transition of the pressure medium. We see a clear development of a spatial pressure gradient at 13.6 GPa. . . . . 36

3.10 **Sensing superconductivity using diamonds particles in high pressure chamber (figure reproduced from Yip *et al.* [107]):** (a) A comparison of white light (left) and fluorescence (right) images showing MW driving coil and diamond particles in the sample chamber of the pressure loading. Scattered diamond particles can serve both pressure calibration and spatially resolved magnetic sensing. (b) Warming up across a superconducting transition with an applied magnetic field, the authors perform vector magnetometry at three points to show local changes due to Meissner expulsion of the applied field from the interior of the superconducting sample. Above the superconducting transition ($T_C$), all three locations measure the same applied field. . . . . 37

3.11 **A survey of magnetic sensing at high pressure [49]:** spatial resolution is defined as the length scale over which the sensor can probe variations in magnetism. For the case of the superconducting quantum interference device (SQUID) and pick-up coils, the spatial resolution is the size of the coil over which the entire signal is integrated. The performance of this work and projected sensitivity for future work shows the ability of NV centers to outperform several conventional high pressure probes of magnetism. . . . . 39

4.1 **Zero field cwODMR spectra in type Ib diamond [75]:** cwODMR spectra of NV centers in type Ib diamond show a clear splitting with features that do not fit to Gaussian or Lorentzian lineshapes. In particular, the inner slope at the splitting is sharper than expected based on inhomogeneous broadening. In addition, we observe consistent heavy tails away from the center. The inset shows a naive expectation based on zero field splitting term ($H_0 = D_{gs}S_z^2$, where $D_{gs} = (2\pi) \times 2.87\,\mathrm{GHz}$) and inhomogeneous broadening coming from magnetic noise. . . . . 40

4.2 **A comparison of random electric fields and strain in ensemble NV spectra [75]:** Strain and electric field couple in similar fashion to the ground state spin of the NV center. (a) A symmetry conserving term $\Pi_z$ causes the $|m_S = \pm 1\rangle$ manifold to shift. (b) In contrast, a symmetry breaking term $\Pi_\perp$ leads to a splitting and mixing of the $|m_S = \pm 1\rangle$ states. (c) Due to comparable susceptibility parameters, a random strain is likely to both shift and split the NV spectra by the same order. In the presence of random local strain, the spectra of NV ensembles should consequently show an overall broadening (at large strain values). (d) In contrast, the splitting due to a transverse field is about fifty times larger than that due to an axial field of the same strength. Consequently, at large field strengths, ensemble averaging of random electric fields is more likely to yield a splitting in cwODMR spectra. A simulation on the right shows the evolution of the NV cwODMR spectrum with the strength of a random local vector electric field. Based on this evolution, one can earmark typical field strengths for Type Ib and Type IIa samples. A microscopic charge model based on this qualitative picture can allow us to extract the density of charged defects in different samples (see [75] for full details).
**Note:** This figure (taken from [75]) has been doctored for illustrative purposes only. . . . . 43

4.3 **Typical spectra of ensemble NV centers due to local electric fields [75]:** (a) An illustration of the microscopic charge model wherein NV centers are surrounded by charge defects yielding an effective electric field. The ensemble averaging of random fields (due to different local charge environments of each NV center) results in the spectra in (b-c). (b) In a high density (type Ib) sample, a higher concentration of charge defects causes the $H_E$ term in the NV Hamiltonian to dominate the hyperfine coupling with the $^{14}$N spin. (c) In a low density (type IIa) sample, a lower concentration of charge defects results in qualitatively different spectra resembling the expectations from the hyperfine coupling with the $^{14}$N nucleus. The extremal resonances for $|m_I = \pm 1\rangle$ (where I represent the nuclear spin) split quadratically with the strength of the electric field. However, for $|m_I = 0\rangle$, the NV spin evolves linearly with the electric field strength showing a clear splitting. . . . . 44

4.4 **Vector imaging of local electric fields by modulating MW polarization [75]:** (a-b) The application of linearly polarized microwaves allows us to modulate the transition amplitudes between $|m_S = 0\rangle \leftrightarrow |\pm\rangle$ (eigenstates under electric field) for single NV centers. In the case of low electric field strength (a), we look at the modulation of the inner two peaks ($|m_I = 0\rangle$). In the case of higher electric field strength (b), we look at the modulation of the two resonances. The inset in (a) is an illustration showing the orientation of the microwave polarization ($\phi_{MW}$) relative to the transverse electric field ($\phi_E$) in the frame of the NV center. The rotation of the MW polarization results in modulation of the resonance amplitudes allowing us to measure $\phi_E$. (c) A illustration showing the eigenstates in the presence of an electric field yielding a shift ($\Pi_z$) and splitting ($2\Pi_\perp$). MW polarization along $\phi^A_{MW}$ ($\phi^B_{MW}$) yield maximal resonance amplitude for $|-\rangle$ ($|+\rangle$). (d) Measuring the change in imbalance ($\mathcal{I}$) of resonance amplitudes on rotating the MW polarization allows us to extract $\phi_E$. Data is shown for a single NV center in (a). Dashed lines indicate the $\phi_{MW}$ values for spectra plotted in (a). . 45

5.1 **Source mechanism of an earthquake (reproduced from [39]):** The moment tensor of an earthquake is a signature of its focal mechanism. This schematic in Frohlich's book [39] shows the three possible source mechanisms. An **isotropic source** shows uniform tension (or compression) as one would expect in a structural phase transition resulting in volume collapse. In contrast, a **double couple source** shows simultaneous tension and compression along mutually perpendicular directions. Finally, a **CLVD source** mimics the bursting of a water balloon, wherein tension along a plane is accompanied by compression (at twice the rate) along the normal direction. Seismic data from deep earthquakes point towards double couple sources, which rule out focal mechanisms driven by simple volume collapse. . . . . 49

5.2 **Displacement sensing of acoustic emissions:** (a) A illustration of the DAC loading showing in-plane displacement sensors P1, P2, and P3 (orange, green, and red) and axial sensor A (blue). The sensors shown are color-coded with their respective signal traces. All sensors are coupled orthogonally to the DAC. (b) Top-down view of the DAC illustrating the determination of source mechanism. Simultaneous detection of compression (+ sign) on the P2 and P3 and tension (o sign) on P1 and A allow us to constrain the orientation of the double couple source. The most likely boundary between compressional and tensional regions of the source is shown by the convex solid black line in the center with possible angular error (broken black line). A concave broken line shows an alternative (but unlikely) source mechanism. (c) Time series data of displacement signals show clusters of acoustic emissions. (d) Full waveform of a typical acoustic emission. First, motion analysis can identify five categories of source mechanisms for this data set. Each acoustic emission in (c) is thereby ascribed to its particular first motion group (colored bars) (e) Example traces from each first motion type are color-coordinated to the colored bars under the emission cluster (c). Focal mechanisms (insets) show relative motions as viewed orthogonal to the compression axis, viewed along sensor 1. Data was collected and analyzed by Thomas Smart and Jes Parker. . . . . 50

5.3 **X-ray diffraction:** (Right) XRD intensity versus $2\theta$ (diffraction angle) for a mixture of clino- and ortho-Chrysotile Serpentine on compression and decompression between $0 - 25\,\mathrm{GPa}$. An orange (blue) background indicates that acoustic emissions (AE) were observed on compression (decompression). The color bar shows the ruby pressure for each XRD measurement. Miller indices for the relevant peaks are indicated on the ambient pressure diffraction pattern. Indices for $[00l]$ peaks are italicized. (Left) Illustrations show structural changes based on the interpretation of XRD data. Under ambient conditions, the stacked magnesium-silicate sheets in Serpentine are aligned in the $[hk0]$ plane and are held together with weak hydrogen bonding in the $[00l]$ direction. In the amorphous phase, there is disordering within each layer and a loss of inter-layer hydrogen bonding. On quenching the pressure, there is partial recrystallization of the magnesium silicate sheets, evidenced by the recovery of $[hk0]$ peaks. Preserved peaks ($[020], [130], [205], [060]$) are associated with the magnesium-silicate sheets. Peaks associated with the inter-layer stacking $[00l]$ are not recovered, suggesting the irreversible loss of inter-layer hydrogen bonding. The apparent doubling of the [020], [204], and [060] peaks is caused by the mixture of orthorhombic and monoclinic chrysotile in the sample. Data collected and analyzed by Thomas Smart and Jes Parker. . . . . 52

5.4 **Widefield Setup and Data:** (a) The 2 W 532 nm excitation laser from a Coherent Verdi V-2 is passed through an optical diffuser (Optotune LSR-3005-6D-VIS) and directed towards the sample. The diffuser reduces the spatial coherence of the laser and improves image quality. An aspheric lens curbs the beam's divergence after the diffuser. The sample's fluorescence is separated from the excitation path by a dichroic beam splitter (AVR Optics FF556-SDi01-25x36) and focused on an EMCCD camera (Princeton Instruments ProEM-HS: 512BX3). A condenser lens before the camera helps increase the field of view (FOV) of the setup to 200 µm × 200 µm and capture the full culet surface. The MW setup for the widefield apparatus is identical to Fig. 1.6. A $\vec{B}$ field was applied using three electromagnets oriented along the $\hat{X}, \hat{Y}$, and $\hat{Z}$ axes in the lab frame (b) A sample widefield fluorescence image of a 200 µm diamond culet (black scale bar shows 25 µm). One can make out the high pressure sample chamber and bright ruby pressure markers distributed across the culet. A widefield data set comprises a cwODMR spectrum at each pixel on this image. Taking a vertical linecut at the center of this image (broken white line), we can look at a so-called 'waterfall plot' (c), showing the spatial variation of the ODMR resonances along the column. In the waterfall plot, we observe two types of resonances. 'Background resonance lines' coming from NV centers in the facets show no spatial dependence. In contrast, resonances from NV centers at the culet show clear spatial dependence. 54

5.5 **Fitting Background Resonances (compression pressure point $\sim 6.75$ GPa):** (a) We can identify the seven background resonances (white dashed lines) and resonances of the [111] NV group in the culet (blue arrows) in the waterfall plot. Identifying pixels showing the low overlap between the background and culet resonances, we can generate the background resonance profile. The center frequency of the background resonances is used to determine the applied magnetic field. (b) The resulting profile of background lines (with fixed relative contrast) can be scaled when fitting to resonances of the [111] NV group in the culet (blue arrow) to extract the stress parameters. (Note how much easier it is to identify and follow resonances in the waterfall plot (a) compared to the cwODMR signal for a single pixel (b)) (c) Restricting ourselves to the sample chamber region (white box), we fitting the resonances of the [111] NV group in the culet. (d) and (e) Fits of the center frequency for the left and right [111] peaks in (a,b) clearly show the sample-gasket boundary. White scale bars on (c-e) denote 25 µm . . . . . 56

5.6 **Extracting stress parameters:** (a) For this study, we used a [111] cut diamond anvil. The orientation of the four NV groups with respect to the lab frame is shown. Note that the [111] group is oriented along $\hat{Z}$, and the applied B field is largely pointed along this direction. This allows us to ascribe the outermost background resonances to the [111] NV group. (b) We fit for the applied $\vec{B}$ field in the [111] NV frame (coincident with the lab frame). The solution is overconstrained because we have three free parameters $(B_x, B_y, B_z)$ and seven center frequencies from the background resonances (for this particular data point, an eighth resonance is neglected due to low contrast). Fitting to the $\vec{B}$ field, we plot the predicted eight resonances (dashed red lines). (c) and (d) It is straightforward to extract the stress parameters $(D, E)$ given a known background field. The $D$ and $E$ maps show qualitatively different features, but the sample-gasket boundary can be distinguished in both cases. White scale bars on (c) and (d) denote 25 µm. . . . . 58

5.7 **Magnetite impurities in the sample:** (a) Fluorescence widefield image of the high pressure chamber shows ruby particles (bright spots) scattered throughout the culet surface. (b) A white light image shows grains in the sample chamber at points that do not show marked ruby fluorescence but instead show dipole patterns in the map of the $E$ parameter in (c). This suggests that these grains are magnetite impurities creating a parasitic local field. Since it is invalid to attribute the splitting entirely to culet stress near these particles, we sample the stress parameters at select points (red squares) around the high-pressure chamber to get an estimate of the true values of $D$ and $E$. . . . . 59

5.8 **Studying changes in** $(D, E)$ **across acoustic emission events:** (a) The $D$ (shift) parameter shows a linear increase with applied pressure (measured using ruby fluorescence). An empirical conversion of $dD/dP \approx 8\,\mathrm{MHz/GPa}$ gives a precise correspondence between the ruby and NV pressure gauges (the grey line shows $x = y$ between the two pressure axes). Crucially, we see no clear change in the shift parameter across acoustic emission (AE) events on both compression (orange) and decompression (blue). **Note:** In the case of [111] cut culet, it is not possible to decouple the $\sigma_{zz}$ and $\sigma_{\perp}$ terms based on the shift alone. We use an empirical conversion to simplify the challenge of pressure calibration using the NV center. Nevertheless, the exact value of $dD/dP$ may depend on the material (or pressure medium) in the sample chamber. (b) Tracking the $E$ (splitting) parameter, sampled across the high pressure chamber, we see a qualitatively different behavior compared to the shift. On compression, there is a consistent accumulation of symmetry breaking stress up to AE events (the inset shows an AE trace). Concurrent with AE, we see a clear drop in the $E$ parameter suggesting a relaxation of this stress. (c) The behavior of the $E$ parameter is the same for samples that have already undergone a cycle of compression and decompression. In this plot, we track the $E$ parameter on such a sample, seeing jumps in the splitting parameter on further compression and decompression.
**Note:** Modelling $E = 2\beta_2\sqrt{\sigma_{xz}^2 + \sigma_{yz}^2}$, we can extract the shear stress (shown in (b) and (c)) from the splitting parameter. Error bars show a range in the $D$ and $E$ parameters instead of standard deviation. . . . . 61

5.9 **Spatial analysis of pressure and shear stress:** Maps of pressure (top row) and shear stress (bottom row) extracted from the $(D, E)$ stress parameters. Image correlated maps of the NV pressure across the sample chamber for pressure points (a) 8.7 GPa and (b) 8.9 GPa on compression. We see clear acoustic emissions between the pressure points (shown on the top left). (c) Difference map of NV pressure: (b)-(a) We do not see telling micron scale features in the stress maps, perhaps because of the equilibration of local stress perturbations during data acquisition. Shear stress maps for the same pressure points are shown in (d) and (e). (f) Difference in shear stress: (d) - (e) (the order is changed because the pressure point at 8.7 GPa shows higher shear stress before AE). We see a clear build-up of shear at the sample gasket boundary (lower right). The simple difference does not remove features stemming from parasitic magnetic fields because splittings due to stress and magnetism add in quadrature. . . . . 62

6.1 **Preliminary studies of NV centers under pressure (figures reproduced from [28]):** Doherty *et al.* [28] conducted an early study of the dependence of the electronic and spin properties of the NV center under hydrostatic pressure. (a) In their experiments, the cwODMR line showed a drastic reduction in contrast with the increase in pressure. (b) Based on data acquired in [28], the shift in the optical zero phonon line (ZPL) was projected to cross 532 nm (green line) at $\sim 66$ GPa potentially precluding standard excitation schemes for NV experiments. 64

6.2 **NV response to hydrostatic pressure:** (a) (Top left inset) A loading of microdiamond using salt (CsI) as a pressure medium was used to study the NV response to hydrostatic pressure. cwODMR data obtained for excitation wavelengths 532 nm (green) and 405 nm (violet) are shown at all pressure points. The data clearly shows an appearance of a cwODMR resonance under 405 nm excitation at higher pressures. (Bottom right inset) A fluorescence scan shows the ruby pressure marker and a microdiamond. White scale bar denotes $\sim 10$ µm. (b) cwODMR spectra at $\sim 17$ GPa shows a clear resonance for 532 nm excitation and no clear resonance for 405 nm excitation. In contrast, (c) shows a clear resonance for both excitation wavelengths at $\sim 100$ GPa. (d) Photoluminescence (PL) spectra at $\sim 17$ GPa show strong $NV^-$ emission $> 637$ nm and low $NV^0$ emission for 532 nm excitation. At these lower pressures, 405 nm emission shows a stronger $NV^0$ contribution to the PL spectrum. (e) At $\sim 100$ GPa, PL spectra for both excitation wavelengths show better correspondence with a clear $NV^-$ contribution. 66

6.3 **Comparison of cwODMR signal with multiple excitation wavelengths:** (a) A comparison of cwODMR spectra with different excitation wavelengths for a [100] cut culet at $\sim 50$ GPa. (b) A comparison SNR $\sim$ contrast $* \sqrt{\text{counts}}$ in cwODMR for 532 nm and 450 nm excitation wavelengths shows no distinct advantage of working with higher energy excitation at high pressures for [100] cut culets. . . . . 68

6.4 **Stress calibration using NV centers in a [100] cut culet:** (a) cwODMR measurements at the culet center show a pressure-induced shift ($D$) and splitting ($2E$) in the NV resonance due to symmetry preserving and symmetry breaking components in the stress. Note that there is a marked reduction in contrast with increasing pressure. (Inset) The measured shift in the resonance frequency is 9.8 MHz/GPa. (b) Using the shift and splitting measured at the center of the culet, the extracted crystal stress $\sigma_{ZZ}$ and $\sigma_{\perp}$ is plotted against the ruby/Raman pressure marker. There is a clear correspondence between the $\sigma_{ZZ}$ stress and the sample pressure (consistent with the continuity of this stress component across the diamond-sample interface). The grey line simply plotting $x = y$ (without any fitting to the data) demonstrates the viability of the NV center as a pressure calibrant. (Inset) The measured ratio of $\sigma_{\perp}$ to $\sigma_{ZZ}$ at each pressure step. There is a clear increase in the relative magnitude of $\sigma_{\perp}$ with pressure suggesting a cupping of the diamond culet with an increase in pressure [65]. . . . . 69

6.5 **Imaging stress in a [100] cut culet:** (a) and (d) show widefield fluorescence images of the sample chamber at 2.8 GPa and 42 GPa respectively (white scale bars show 10 µm). At low pressures, ruby microspheres scattered throughout the culet are markedly brighter than NV centers. Furthermore, due to the geometry of the loading, only NV centers in the sample chamber of the culet were optically accessible, restricting our study to this region. The ruby fluorescence is markedly diminished at high pressures relative to the NV centers. (b) and (e) are maps of the $\sigma_\perp$ stress in the sample chamber at the two pressure points. At low pressure, the stress distribution is comparatively uniform across the chamber. At high pressure, the $\sigma_\perp$ stress is concentrated at the center of the culet. (c) and (f) are maps of the $\sigma_{ZZ}$ stress in the sample chamber.
**Note:** The extracted stress maps neglect the presence of $\sigma_{RZ}$ stress terms. While this is a reasonable assumption at the center of the culet for centrosymmetric systems (yielding the measurements in Fig. 6.4), it may not be accurate for the entire culet (and certainly not in the gasket region). Although a pressure medium may alleviate significant shear stresses in the sample chamber region, the extracted $\sigma_\perp$ and $\sigma_{ZZ}$ values likely represent an upper bound in the absence of any shear stress. . . . . 70

6.6 **Contrast inversion under pressure:** The shift of the cwODMR resonance (circle) and the center frequency of the two peaks (triangles) is plotted against the ruby/Raman pressure. (Insets) We see a clear shift and splitting of the resonance lines (3 GPa and 42 GPa data points). The differential contrast at 42 GPa is due to the mixing of the $|S = 1, m_S = \pm 1\rangle$ states under a symmetry breaking stress. All points above $\sim 60$ GPa show inverted (positive) for the left resonance (70 GPa data point shown in inset). Despite contrast inversion, the linear trend in the center frequency of both the right and left resonance peaks is maintained up to the highest pressures. Measurements of the stress components $\sigma_{ZZ}$ and $\sigma_\perp$ detailed in Fig. 6.4 are based on this data. . . . . 71

6.7 **Contrast inversion in [110] cut culets:** (a) . Fluorescence widefield image of a [110] cut culet at $\approx 30$ GPa with white scale bar showing 50 µm. The profile of NV resonance for a vertical line cut (broken white line in image) is shown in (b). A cwODMR resonance line (blue) generally has lower fluorescence than the background (green). However, we see three resonance lines with higher fluorescence (yellow) than the background. White arrows point to these positive contrast lines. Rabi measurements on a positive contrast peak (d) show a phase difference of $\pi$ compared to that on a negative contrast peak (c). Insets show cwODMR resonances on which the rabi measurements were performed.
**Note:** Pulsed measurements (c,d) were performed on a separate loading of a [110] cut culet at $\approx 40$ GPa. Data in (a,b) taken by Satcher Hsieh. . . . . 72

6.8 **Possible mechanism for positive contrast:** (a) Under stress, the excited state orbitals shifting ($\Pi_z$) and splitting ($\Pi_\perp$) is on the scale of $\sim$ THz/GPa [26]. The stress term dominates the orbital fine structure leading to two orbital branches with spin-1 manifolds in each branch. The spin sub-levels within each branch may be further split (and mixed) by spin-spin and spin-stress coupling terms of the order $\sim$ GHz/GPa (the latter being largely unknown). The interplay of orbital and spin degrees of freedom under stress likely mixes the symmetry-dictated spin states ($|A_1\rangle$, $|A_2\rangle$, $|E_{x,y}\rangle$, $|E_{1,2}\rangle$) that exist under ambient conditions [45]. Consequently, $|\pm\rangle$ spin states in each orbital branch has $|A_1\rangle$, $|A_2\rangle$, and $|E_{1,2}\rangle$ character whereas the $|0\rangle$ spin state has $|E_{x,y}\rangle$ character. (b) Under ambient conditions, spin-orbit coupling mediates the intersystem crossing pathway from the excited $|^3E\rangle$ state to the singlet manifold [45]. The transition is strongest (first order) for the $|A_1\rangle$ state. However, under the influence of stress, modifications to the spin-orbit coupling term may facilitate further transitions terms $\Gamma^+_{A_1}, \Gamma^-_{A_1}$ and $\Gamma_{x,y}$. Speculating that spin-stress coupling terms in the $^3A_2$ and $^3E$ states yield similar spin eigenstates under stress, it is conceivable that electronic excitation will spin conserving. In the regime $\Gamma^-_{A_1} < \Gamma_{x,y} < \Gamma^+_{A_2}$, we are going to get a combination of positive and negative contrast peaks (necessarily assuming that $|^1A_1\rangle \rightarrow |^3A_2\rangle$ transition rates are unaltered under stress). Future experiments may probe aspects of this ISC picture (proposed by Bryce Korbin and Maxwell Block). Current collaborations with Benchen Huang (in the group of Prof. Giulia Galli) aim to understand modifications to the spin-orbit coupling under different stress profiles. . . . . 73

6.9 **Contrast, Stress, and the intersystem crossing:** (a) A detailed schematic of the intersystem crossing (ISC) reproduced from [45]. $\Gamma_{A_1}$ and $\Gamma_{E_{1,2}}$ represent the transition rates from the sublevels of the $^3E$ excited state to the $|^1A_1\rangle$ singlet state. Goldman *et al.* modeled the former transition ($|A_1\rangle \rightarrow |^1A_1\rangle$) as a first-order process driven by spin-orbit coupling. The latter transition occurs at second order due to the electron-phonon mixing within the $^3E$ manifold and subsequent spin-orbit transition to the $|^1A_1\rangle$ state. (b) The channel to the singlet state was modeled as a resonant transition from the $^3E$ manifold to the phononic excitations of the $|^1A_1\rangle$ state. The transition rate depends on the density of phononic excitation states $\rho(\Delta)$ resonant with the $^3E$ manifold (shown here as a vibrational overlap function $F(\omega)$ computed using the optical spectrum of the $|^3E\rangle \rightarrow |^3A_2\rangle$ emission). A decrease in $\Delta$ increases the density of states on resonance and enhances the ISC transition. (c) Studies by Davies and Hammer [26] show that stress along the [111] crystal axis reduces the energy of the $^3E$ orbital for one of the NV groups (blue), likely decreasing $\Delta$ in the ISC channel shown in (b). Based on the ISC picture, this NV group may show contrast retention at the highest pressures.
**Note:** Image (a) and (b) are reproduced from [45]. . . . . 75

6.10 **NV sensing up to megabar pressures using [111] cut anvils:** (a) A comparison of cwODMR contrast for [111] cut culet at $\sim 80\,\mathrm{GPa}$ with that for [100] cut culet at the same pressure range shows clear contrast retention in the former case. (b) Applying an axial magnetic field ($B_Z$) in a [111] cut culet shows a clear evolution of the Zeeman splitting in the [111] NV group verifying the integrity of our high-pressure signal. A low fields, the splitting due to symmetry breaking stress adds in quadrature with the Zeeman splitting, giving a total splitting of $\Delta\nu = \sqrt{(2E)^2 + (2\gamma B_Z)^2}$. At large fields, the splitting due to the magnetic field dominates and grows linearly. The inset shows the cwODMR spectra for this data set. cwODMR and pulsed measurements at $\sim 120\,\mathrm{GPa}$ for a [111] cut culet are shown in Fig. 1.7. . . . . 76

6.11 **A comparison of culet cuts for high-pressure sensing:** (a-c) Based on measurements by Davies and Hammer [26], we can predict the splitting and shifting of $^3E$ orbitals of the NV center for different stress profiles (Insets show the orientation of different NV groups relative to the loading axis $\hat{Z}$). (a) A [100] uniaxial stress projects equally on all four NV groups. (b) A [110] uniaxial stress gives two sets of doubly degenerate NV groups. For groups in the culet plane (red), the $^3E$ orbitals are blue-shifted to higher energies. In contrast, for NV groups in the plane perpendicular to the culet (blue), the $^3E$ orbitals are red-shifted to lower energies. In the former case, we expect a reduction in the ISC rate and consequent loss of contrast. In the latter case, we expect some contrast retention up to high pressures. (c) For a [111] cut culet, the symmetry is preserved for one of the NV groups (blue), and the orbital energies are red-shifted. Increase in orbital energies for the other three groups (red) leads to a loss of contrast. (d-f) cwODMR spectra for different stress profiles. (d) In the [100] case, all groups are degenerate, showing a shift and a splitting due to stress. (e) cwODMR spectrum at $\sim 40\,\mathrm{GPa}$ for a [110] cut culet shows resonances from two nearly degenerate NV groups. An applied magnetic field often shows four clear resonances (see Fig. 6.7), possibly belonging to the NV groups oriented in the plane perpendicular to the culet. (f) For a [111] cut culet, the resonance of the [111] NV group survives above megabar pressures.
**Note:** The spectrum in (f) was taken with an applied $\vec{B}$ field. The spectra in (d,e) were taken with zero background field. . . . . 78

7.1 **Phase diagram of type I and type II superconductors:** Type I superconductors (left) expel magnetic fields from the sample interior (Meissner phase). Applying fields larger than $H_C(T)$ destroys superconductivity in the material. In contrast, type II superconductors (right) have two critical fields. Below $H_{C_1}(T)$, these materials are in the Meissner phase showing complete field expulsion in the bulk. However, for $H_{C_1}(T) < H < H_{C_2}(T)$, these materials exhibit field penetration through the bulk sample in the form of vortices (mixed phase). Type II materials can remain superconducting up to much higher fields of $H_{C_2}(T)$. . . . 81

7.2 **Loading and sample synthesis:** (a) A schematic of the sample showing type Ib anvil with NV centers (above), a Pt wire, and the opposing type Ia anvil (below) with transport leads. The Ce metal sample was positioned to make electrical contact with the leads. An insulating gasket using Calcium Fluoride ($CaF_2$) was fashioned out of a rhenium foil. The sample chamber was filled with Ammonia Borane ($NH_3BH_3$). (b) An optical image showing the Ce sample and transport leads. The sample was heated by rastering a 10 W laser (red spot) to induce the decomposition of Ammonia Borane. The emitted hydrogen can combine with the sample to form hydrides. (c) Confocal fluorescence scan taken after laser heating over the same sample region as (b). Interference fringes show the four transport leads in the corners of the sample. Distinct bright regions around the sample show markedly higher fluorescence suggesting the creation of NV centers due to laser heating. In (b) and (c), white scale bars denote 10 µm. 82

7.3 **Verification of sample synthesis using transport:** (a) Fluorescence scan of the sample showing leads used for current flow and voltage pickup. (b) Transport measurements performed using the delta technique at Jilin University (by Wuhao Chen). The sample shows a clear drop in resistance at $\sim 90$ K. Application of $\sim 1$ T scale magnetic fields suppresses $T_C$, suggesting superconducting behavior. The noise source in the high field measurements is not completely understood (likely due to inductive pickup or hall currents). (Inset) Illustrations show the projected magnetic response of the sample to applied magnetic fields in the normal state (right) and superconducting state (left) (images sourced from [24]). The sample expels the applied field from the interior in the Meissner phase (left). . 83

7.4 **NV creation through laser heating:** (a) Confocal fluorescence scan of the sample. (b) A cut along the $xz$ plane across laser heated points (grey box) shows dense pockets of NV centers. (c) NV centers in the laser heated regions show markedly higher contrast. Furthermore, the stress splitting ($2E = 2\sqrt{E_x^2 + E_y^2}$) is lower in these regions, likely due to local stress relaxation on laser heating. . 84

7.5 **Calibrating magnetic fields:** (a) Schematic of the experimental apparatus showing the vacuum shield of the cryostat and the electromagnet. The electromagnet is coaxial with the cryostat and the DAC, with the dominant field component along the $\hat{z}$ axis. The applied field aligns with the quantization axis of the [111] NV group. (b) Calibration of the magnetic field, performed at the start of every cooldown, involved studying the cwODMR splitting as a function of the applied current (inset shows the measured cwODMR spectra). The Zeeman splitting due to the magnetic field ($B_z$) adds in quadrature with the splitting due to the symmetry breaking stress ($2E$), giving a hyperbolic profile ($\Delta\nu = \sqrt{(2E)^2 + (2\gamma B_z)^2}$). The measured splitting shows excellent agreement with the model with comparable $B_z/I$ values at several points on the culet. . . 85

7.6 **Thermal linking:** (a) A custom thermal link (Four Nine Design) between the cell body and the cold finger of the cryostat allowed for better thermalization. The thermal link was secured to the cell body using a girdle machined out of a copper plate. (b) A second thermal link was attached between the metal gasket and the cell body to account for the diminishing thermal conductivity of diamond below 100 K. The link was cut out from Indium (In) foil and attached at either end by cryogenic epoxy (Stycast® 2850FT). (c) Lock-in measurements show a drop in sample resistance at $\sim 70$ K at zero applied magnetic field. This resistance drop is accompanied by a jump in the measured phase from 0° to $\sim 150°$ deep in the superconducting state. The transition point is $\sim 20$ K lower than the true $T_C$ of the sample due to the thermal gradient between the cold finger (location of temperature reading) and the high pressure sample. . . . . 87

7.7 **Observation of Meissner effect on ZFC:** (a) Phase diagram of a type II superconductor. The ZFC path (green broken arrow) involves cooling below $T_C$ at zero applied background field. Deep in the superconducting state following ZFC, the sample resists the permeation of applied fields (Meissner effect). We test this by ramping up a background $H_z$ field (solid green arrow) and studying the evolution of the splitting. (b) Confocal scan of the sample showing laser heated regions (bright areas). The NV splittings at two representative points show markedly different behavior on ZFC. White Scale bar denotes 10 µm. (c) A study of NV splitting with applied $H_z$ field (green arrow on abscissa connects to the path taken in phase map). At this spatial point, the NV splitting data follows the expectation based on the calibrated applied field. This behavior is consistent with no superconductivity (SC) in this region (grey line) where $B_z \approx H_z$. Insets show the cwODMR data (top) and illustration of the inferred sample behavior at this point (bottom) [24]. (d) A study of NV splitting with applied $H_z$ field shows clear suppression. We can extrapolate the expected (no SC) response (gray line) in this sample region by noting the splitting ($2E$) at zero applied field. However, the observed splittings (blue data points) show a marked deviation from this expectation , suggesting local suppression of the applied field due to the Meissner response of the sample. Fitting a hyperbolic profile to the splitting $\Delta\nu = \sqrt{(2E)^2 + (2\gamma\, B_z)^2}$ (blue line) gives $B_z/H_z \approx 0.7$. Insets show cwODMR spectra and inferred magnetic response of the sample [24]. . . . . 89

7.8 **Spatial studies of Meissner suppression:** (a) Optical microscope image of sample 1 showing Cerium metal and transport leads. (b) Confocal image of sample 1 (partially rotated with respect to (a)). Performing ZFC measurements of the type in Fig. 7.7 along a line cut (white points) allows us to observe the spatial extent of the Meissner suppression. (c) The ratio of $B/H$ obtained along the line cut in (b). The white arrow in (b) gives the direction of increasing distance. The measurement shows that the sample size is of the order of $\lesssim 10$ µm. Studies on sample 2 (d-f) yield similar results. In all images, white scale bars denote 10 µm. . . . . 90

7.9 ***Simultaneous*** **transport and magnetism studies on ZFC:** (a) Path taken in phase space. Green broken arrows show preparatory steps. Starting in the normal state, we perform ZFC and then apply a background $H_z$ field. Fixing the applied field at $\sim 80\,\mathrm{G}$, we increase the temperature (green solid arrow). (Inset) Due to the Meissner effect, the NV splitting is suppressed near the superconductor with the difference in observed and expected splitting being $\gtrsim 100\,\mathrm{MHz}$. (b) Simultaneous transport and magnetometry measurements show an increase in the NV splitting and a sharp rise in the sample resistance. Image in the inset shows the spatial point (white square) at which the NV splitting was monitored. White scale bar denotes $10\,\mu\mathrm{m}$. . . . . 91

7.10 **FC studies across the superconducting transition:** (a) The path taken along the phase diagram for FC temperature sweep. (b) Confocal scan of the sample showing the superconducting (SC) region enclosed in white broken lines. White scale bar denotes $10\,\mu\mathrm{m}$. The NV splitting was surveyed at four spatial points (color-coded to data in (c)). (c) On field cooling, we observe a decrease in the NV splitting at points on the superconducting region (blue and red) and an increase in the NV splitting at the edge of this region (green). The onset of these changes roughly corresponds to a drop in the resistance of the sample (grey). There is no perceptible change in the splitting across $T_C$ for a point far away from the superconducting region. Colored broken lines are a guide to the eye showing the splitting profile at each spatial point. . . . . 93

7.11 **Comparison of measurements at $H_z = 0$ after ZFC and FC:** cwODMR spectra on ZFC (FC) shown in blue (red) at four spatial points. Insets show the spatial point (white dot) corresponding to the measured spectra. Details of the confocal map in the inset are identical to Fig. 7.10 (b). Points (a) and (b) on the SC region clearly show a larger splitting on FC compared to ZFC, suggesting the presence of a local magnetic moment due to trapped flux in the sample. In contrast, points (c) and (d) do not show any perceptible difference between ZFC and FC, serving as a control for parasitic background fields. The right inset in (c) shows the path taken in the phase map for these measurements. . . . . 94

7.12 **Flux trapping in negative fields:** (a) The measurement protocol comprises field cooling (FC) deep into the superconducting phase and then quenching the background field. Subsequently, we tuned both magnitude and direction of $H_z$, applying both positive (blue) and negative (green) fields. (b) An illustration showing the application of negative fields. The direction of the applied $H_z$ during FC is frozen into the sample as a trapped flux. A negative applied field is oriented opposite to this direction and therefore competes with the 'effective' magnetic moment of the sample. (c-d) Plots showing the spatial location where the study was performed (top) and the observed profile of the NV splitting in different cases (bottom). Spatial points in (c) and (d) probe the SC region of the sample, while point (e) is located away from this region and serves as a control. For points (c) and (d), we see clear suppression of the applied magnetic field on ZFC (orange data points) relative to the expectation in the absence of a superconductor (grey line). In contrast, the splitting at point (e) closely follows the 'no SC' expectation. On FC and quenching the magnetic field, we measure NV splitting to be higher than $2E$ (given by the symmetry breaking stress) at points (c) and (d) due to trapped fluxes in this region. On applying positive fields (blue), we do not see a clear suppression of the splitting until the applied field magnitude exceeds the value at which field cooling was performed ($\sim 80\,\mathrm{G}$ shown by red arrow). Most interestingly, on applying negative fields, we directly see the competition between the trapped flux and the background field manifest in the NV splitting. At small magnitudes of negative field, the NV splitting (green) at points (c) and (d) first decreases down to $\sim 2E$. On further increasing the magnitude of the negative field, the splitting increases but is suppressed with a $B/H$ ratio comparable to the case of ZFC. Crucially for the control point (e), we do not see any difference between the three scenarios, and the splitting closely follows the 'no SC' expectation in all cases. . . . . 95

7.13 **Temperature sweep at negative fields after FC:** (a) Path taken in the phase map. We sweep the temperature after applying negative fields to a FC sample. The applied background field $H_z$ competes with the trapped flux in the superconductor. (b) We survey two spatial points on the sample (inset). A point away from the SC region of the sample yields an NV splitting consistent with the applied background field ($H_z$) (orange data points). This is the same spatial point measured in Fig. 7.12 (e). The splitting does not show any marked change on increasing temperature across the transition point. A point in the SC region (surveyed in Fig. 7.12(c)) shows a clear increase in splitting reaching values consistent with $H_z$ at $T \sim 70\,\mathrm{K}$. (c) Simultaneous lock-in measurements of transport yield sample resistance and phase consistent with the superconducting transition at $T \sim 70\,\mathrm{K}$. In (b) and (c), $T$ is the temperature measured at the cold finger of the cryostat. The true sample temperature is $\sim 20\,\mathrm{K}$ higher due to a thermal gradient in the DAC. . . . . 96

7.14 **Sweeping magnetic fields on field cooling:** (a) The path taken in the phase map involves field cooling at $\sim 100\,\mathrm{G}$ to a fixed temperature below the transition point followed by sweeping the magnetic field - first to negative and then back to positive values. (b) The evolution of the NV splitting in comparison to cases of ZFC (broken red line) and no SC expectation (broken gray line) is shown for three temperature points. At $T \ll T_C$ ($45\,\mathrm{K}$ and $50\,\mathrm{K}$), we see the retention of the trapped flux in the sample even on changing sweeping the fields to large (negative values). However, for $T \sim 65\,\mathrm{K}$, the trapped flux at positive fields is not as strongly pinned when the background field is swept to negative values. At large negative values of the field, flux lines along the negative field direction permeate the sample. Sweeping the field back to the positive direction, we now see the opposite effect wherein the trapped flux along the negative field direction competes with the background field at the NV location. . . . . 97

7.15 **Looking ahead:** Spin echo measurement performed on sample 2 at $\sim 130\,\mathrm{GPa}$. A simple exponential fit gives $T_2^{\mathrm{echo}} \approx 3\,\mu\mathrm{s}$ at these pressures. The inset shows the microwave pulse sequence for the measurement. Coherent measurements are a powerful way to perform AC magnetometry to diagnose interesting features such as critical noise across phase transitions [18]. I am sure that future work on superhydrides and other high pressure systems, using a plethora of quantum sensing techniques such as this, will uncover exciting insights! . . . . . 98

## Acknowledgments

I want to acknowledge my parents Kumkum Bhattacharyya and Pinak Pani Bhattacharyya, my first teachers. It's only after leaving home for study, that I have come to realize and appreciate the lessons that I was raised with. I am fortunate to have my elder brother, Pathikrit Bhattacharyya, help and guide me in various endeavors. Without his push, I would not have considered applying for study in the United States and, most likely, would not be writing this thesis. I owe a lot to Srikumar Sengupta, Nilesh Katiyar, and Arunava Chakravarti for their inspiration and encouragement to pursue higher studies in physics. As an international student, I am indebted to Soma and Sukanto Deb, Barna and Saibal Dey, and Rinku and Tapas Majumdar for being my *de facto* guardians over the last decade as I adjusted to a new country. I also want to thank my undergraduate research advisor, Michael Niemack, without whose help and guidance I would not be pursuing graduate study!

It has been an amazingly profound experience working and learning at UC Berkeley! The energy and drive of the students continue to amaze and inspire me every day. I feel proud to see so many of my peers taking leadership in driving forward conversations on transparency, equity, and diversity in science. I feel hopeful seeing the department's engagement and receptivity to these conversations over time.

The rotation program was one of the primary reasons I decided to apply to Berkeley for graduate studies. Ironically, however, the majority of my years in graduate school were spent trying to secure my role as a Ph.D. candidate. I am grateful to Norman Yao for giving me the opportunity to work in his research group. My meandering path during the initial years in the group gave me a much-needed peek into the multifaceted process of scientific research. I learned the value of having ideas of one's own, taking charge of executing them, and defending them through cogent argumentation. I am certain that my years in graduate school would not have been so transformative in any other group.

The department would be incomplete without the tireless work of the staff. I am grateful to Joelle Miles and Beth McCleary for patiently helping me with my many questions about work, pay, and visas throughout the years. I thank Carlos Bustamante for being an ever-cheerful friend and coordinating package logistics worldwide between Japan, China, and Germany (sometimes with last-minute requests). I spent many enjoyable hours in the student machine shop. I thank Jesse Lopez for *very* patiently teaching and supporting me through this process, often taking charge of the machining when I had broken one too many tools.

Over this time, I was fortunate to find myself with many gracious mentors, talented colleagues, and supportive friends. Thomas Smart was the first to teach me the ins and outs of diamond anvil cells and Raymond Jeanloz was open to meeting when I found myself stuck on several aspects of the project. I thank Raymond, Dan Stamper-kurn and Joel Moore for being part of my Qual Committee. My serendipitous meeting with Zachary Geballe was a turning point in my effort to make insulating gaskets and push to megabar pressures. Viktor Struzhkin and Alex Gavriliuk were instrumental in sending us new cells and suggesting feasible studies (Viktor, in particular, directed us to look at Cerium hydride). Xiaoli Huang and Wuhao Chen were crucial collaborators in our final study of superhydrides, being open

to trying new ideas and ensuring the work was pushed forward despite various setbacks. Chris Laumann and Shubhayu Chatterjee provided theory support in the final months of the megabar project. Much of our work was enabled by the stellar team at Attocube Systems for designing an incredibly versatile AttoDRY 800 cryostat for us. I thank Biplab Bhawal and Juergen Dienstmeyer for their unfailing assistance in troubleshooting many aspects of the system over the years.

I am fortunate to have crossed paths with a number of impeccably talented scientists and immeasurably kind friends, including Neil Glikin, Donez Horton-Bailey, Nikola Maksimovic, Conrad Stansbury, Emma Regan, Qinqin Yu, Jakob Dahl, Kamphol Akkaravarawong, Tim Hoehn, Francisco Machado, Tommy Schuster, Maxwell Block, Bryce Kobrin, Thomas Mittiga, Yuanqi Lyu, Emma Diest, Jon Kruppe, Satcher Hsieh, Greg Meyer, Chong Zu, Emily Davis, and Soonwon Choi during my time in graduate school. I thank Gamila Kanew for being a good friend at a tough time and for introducing me to the excitement and community of BJJ at Ralph Gracie Berkeley. I am very grateful to Kayleigh Cassella for being my friend and mentor throughout graduate school. My summer working with Kayleigh, Eli Megidish, Thomas Mittiga, TJ Wilkason, Xin Xie, Stanimir Kondov, Aaron Smull, Joeseph Lauigan, Tsung Yao Wu, Robin Coxe, Katy Barnes, Miro Urbanek, Krish Kotru, and others at Atom computing was both exciting and deeply educational. It is incredible to watch the space of quantum technologies transition from the research lab to the industry.

I want to end by thanking my wife Amanda, whose kindness and brilliance inspire me every day. Without her love and support, I would not have continued my work in graduate school.

# Citations to previously published work

Parts of Chapter 3 have been published as

> S. Hsieh*, P. Bhattacharyya*, C. Zu*, T. Mittiga, T. J. Smart, F. Machado, B. Kobrin, T. O. Hohn, N. Z. Rui, M. Kamrani, S. Chatterjee, S. Choi, M. Zaletel, V. V. Struzhkin, J. E. Moore, V. I. Levitas, R. Jeanloz, N. Y. Yao. Imaging stress and magnetism at high pressures using a nanoscale quantum sensor. *Science* **366**, 1349 (2019).

Parts of Chapter 4 have been published as

> T. Mittiga*, S. Hsieh*, C. Zu*, B. Kobrin, F. Machado, P. Bhattacharyya, N. Z. Rui, A. Jarmola, S. Choi, D. Budker, N. Y. Yao. Imaging the local charge environment of nitrogen-vacancy centers in diamond. *Phys. Rev. Lett.* **121**, 246402 (2018).

Content of Chapter 5 is in preparation for publication as

> T. Smart, J. Parker, P. Bhattacharyya, S. Hsieh, B. Kobrin, Y.Lyu, S. Glaser, N. Y. Yao, R. Jeanloz. Nano-seismic shear sources and imaging of shear stress from serpentine at lower mantle pressures (in preparation, 2023).

Content of Chapter 7 is in preparation for publication as

> P. Bhattacharyya*, W. Chen*, Shubhayu Chatterjee, Maxwell Block, Yuanqi Lyu, Bryce Kobrin, Satcher Hsieh, Chong Zu, Thomas Smart, Zachary Geballe, Benchen Huang, He Ma, Zhipan Wang, Bijuan Chen, Emily Davis, Viktor Struzhkin, Raymond Jeanloz, Giulia Galli, Bertrand Halperin, Chris Laumann, Xiaoli Huang, Norman Yao. Imaging magnetism in a hydride superconductor at megabar pressures using a nanoscale quantum sensor (in preparation, 2023).

# Chapter 1

# The NV center in diamond

My goal for this chapter is to provide a working knowledge of nitrogen vacancy (NV) centers in diamond for a beginning student. There is no dearth of papers, reviews, and theses detailing the various facets of this topic [29, 73, 9]. Rather than being exhaustive, my objective is to ensure that the reader can get the ground up and running and get 'first light' from their experiment.

**Why care?**

There is much excitement about "quantum technologies" spanning a wide gamut of platforms in atomic and condensed matter physics. The overarching goal is to leverage the quantum properties of these systems (such as coherence, superposition, or entanglement) to outperform classical techniques in measurement and computation. While there is no silver bullet (yet), each platform has the scope and particular strengths catered toward specific tasks.

The NV center is one such emerging platform with promising prospects as a robust and versatile quantum sensor. NV sensing is a burgeoning field encompassing a vast array of work. In this thesis, I will focus on the application of NV sensing at high pressures [70]. I believe this will be a unique and exciting use case that can enable several scientific investigations in condensed matter and geophysical systems.

## 1.1 Description

The diamond crystal is a lattice of tetrahedrally bonded carbon atoms [82]. The nitrogen vacancy color center is a point defect in diamond comprising a substitutional nitrogen atom adjacent to a vacant lattice site. The following sections illustrate some of the unique properties of the NV center that render it particularly useful among the numerous defects that can (and invariably do) occur in natural as well as lab-grown diamonds.

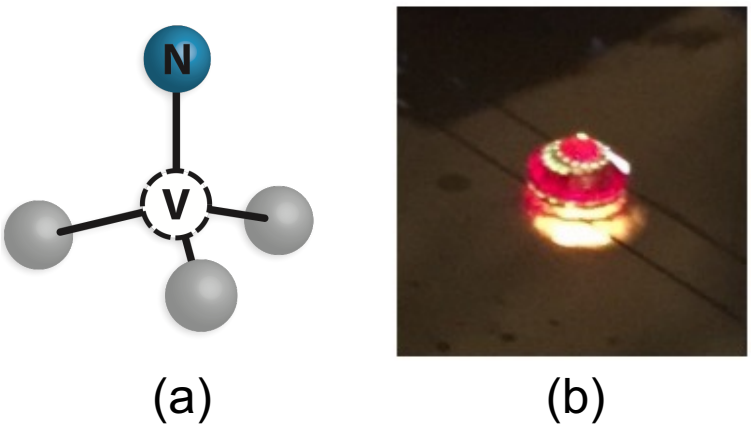


Figure 1.1: **NV center in diamond:** (a) A ball and stick diagram of the NV center. The repeating tetrahedra of carbon atoms (grey) form the diamond lattice. The NV center comprises a substitutional nitrogen atom (blue) adjacent to a vacant lattice site (shown with a broken line) (b) One of the defining properties of the NV center is its fluorescence. A diamond rich in NV centers glows bright red, as the sample shown in this picture.

## Synthesis

There are several techniques for synthesizing NV centers catering to the specifics of the application in mind. The following parameters can help determine the appropriate diamond sample and synthesis recipe:

- Required concentration of NV centers
- Depth of NV centers from the diamond surface
- Presence of other magnetic or charge defects (such as $^{13}$C and substitutional nitrogen defects)

For all of the experiments in this thesis, I worked with high-pressure high-temperature (HPHT) synthesized Type Ib diamond procured directly from the vendor (Almax Easylab or SYNTEK Corp). Type Ib diamond is concentrated with single substitutional nitrogen defects ($\gtrsim$ 10 ppm of P1 centers) [108] and is pale yellow in color. For our applications, we required a high concentration of NV centers near the surface. To achieve this, we used SRIM [112] to simulate the necessary energy and dosage of implanted ($^{12}C^{+}$) ions to create $\sim$10 ppm concentration of vacancies up to 50 nm beneath the surface. Our implantation recipe was the following:

- A dosage of $2.25 \times 10^{11}$ ions/cm$^2$ at energies near 12 keV

- A dosage of $6.75 \times 10^{11}$ ions/cm$^2$ at energies near 30 keV

The final synthesis step was to anneal the sample at temperatures above 850 °C in high vacuum ($< 10^{-6}$ mbar). At these temperatures, the vacancies become mobile in the lattice and may migrate to sites adjacent to naturally occurring P1 centers. Although stochastic, the formation of NV centers in this manner is energetically favorable and impedes further migration of vacancies. Anecdotally, the overall conversion efficiency of P1 centers is $\approx 10\%$ yielding a concentration of $\approx 1$ ppm of NV centers in our samples.

## 1.2 Physics of the NV center

One of the defining properties of the NV center is its fluorescence. A diamond enriched with NV centers is pink in color and, when illuminated, has a beautiful bright red glow (Fig. 1.1(b)). In practice, experiments harvest these fluorescent photons to measure the spin state of the NV center. Therefore, it is imperative to understand the level structure of the NV center and its associated dynamics if one is to employ it as a sensor. **The physics of the NV center is (for the most part) the physics of the electrons that it hosts.** Consequently, we can get a good understanding of its properties by considering the quantum mechanics of the orbital and spin degrees of freedom of the NV electrons.

### Level structure of the NV electrons

Pure diamond with no defects has a bandgap of 5.5 eV (corresponding to deep UV wavelengths of 225 nm) [29]. Generically, defect centers in such high band gap materials can have localized orbitals whose energies lie within the gap. Color centers are a class of such defects that can fluoresce owing to electronic transitions between these orbitals. By virtue of their fluorescence, such color centers paint a transparent diamond in their unique hues.

In the case of the NV center, these localized orbitals can be constructed from the atomic orbitals of the constituent Nitrogen and Carbon atoms. These atomic orbitals are denoted as $\sigma_N$ for the Nitrogen orbital and $\sigma_i$ ($i = 1, 2, 3$) for the three dangling bonds of the lattice Carbon atoms (Fig. 1.2(a)). The NV center is symmetric under operations of the $C_{3V}$ point group. This group is generated by a 120° rotation around the NV axis and a reflection across the plane formed by the NV axis and a Carbon dangling bond. The irreducible representations of the $C_{3V}$ group dictate how these four atomic orbitals mix with each other to render the molecular orbitals of the NV center [29]. These localized molecular orbitals of

the defect center can be written as follows:

$$|a_1\rangle = \alpha\ |\sigma_N\rangle + \frac{\beta}{\sqrt{3}}\Big(\ |\sigma_1\rangle + |\sigma_2\rangle + |\sigma_3\rangle\ \Big) \tag{1.1}$$

$$|a_1'\rangle = \frac{\alpha}{\sqrt{3}}\Big(\ |\sigma_1\rangle + |\sigma_2\rangle + |\sigma_3\rangle\ \Big) + \beta\ |\sigma_N\rangle \tag{1.2}$$

$$|e_x\rangle = \frac{1}{\sqrt{6}}\Big(2\,|\sigma_1\rangle - |\sigma_2\rangle - |\sigma_3\rangle\ \Big) \tag{1.3}$$

$$|e_y\rangle = \frac{1}{\sqrt{2}}\Big(\ |\sigma_2\rangle - |\sigma_3\rangle\ \Big) \tag{1.4}$$

In essence, $|a_1\rangle$ and $|a_1'\rangle$ orbitals are symmetric under all $C_{3V}$ operations and correspond to the one dimensional (trivial) representation of this group. In contrast, the degenerate $|e_x\rangle$ and $|e_y\rangle$ orbitals correspond to the two dimensional irreducible representation of the $C_{3V}$ group [73].

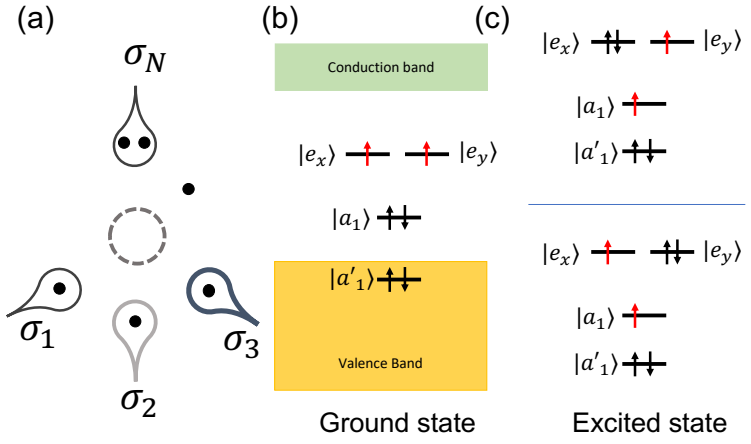


Figure 1.2: **NV orbitals and level structure:** (a) A diagram of the NV center showing the Nitrogen orbital ($\sigma_N$) with an electron lone pair (black dots) and the dangling bonds of the Carbon atoms ($\sigma_i$) with one electron each. The NV orbitals are built out of linear combinations of the four atomic orbitals and populated by a total of six electrons for the $NV^-$ center. The additional electron gained from the lattice is shown near the vacant site. (b) In the ground state of the $NV^-$, the degenerate $|e_x\rangle$ and $|e_y\rangle$ orbitals are each populated by one electron. Together they form an orbital singlet spin triplet state to minimize the coulomb interaction energy of the two electrons. Therefore, the ground state of the NV center is spin 1. The energies of the NV orbitals relative to the band structure of the diamond are shown [29]. (c) In the electronic excited state of the $NV^-$ center, an electron may be promoted from the $|a_1\rangle$ orbital to either of the $|e_{x,y}\rangle$ orbitals. As a result, there are six possible states in this manifold ($^3E$).

The energies of these orbitals can be determined by *ab initio* simulations considering kinetic energies of the orbital wavefunctions as well as electrostatic energies between the electrons and the nitrogen and carbon nuclei. For practical purposes, it is sufficient to think about the $(|e_x\rangle, |e_y\rangle, |a_1\rangle)$ orbital degrees of freedom since the $|a_1'\rangle$ state is believed to lie in the valence band of diamond [29].

### The NV ground state

Knowing the energies of the orbitals, we understand the electronic structure of the ground state. We have two electrons from the Nitrogen lone pair and one each from the Carbon dangling bonds, making a total of five electrons. At this point, it is important to note that the NV center can exist in one of two charge states:

- the neutral $NV^0$ charge state with 5 electrons
- the negatively charged $NV^-$ state with 6 electrons (the extra electron coming from a charge donor in the lattice)

Practically all applications of the NV centers deal with the negatively charged $NV^-$ center as shown in Fig. 1.2(a). Populating the NV orbitals according to the pairing rules, we can construct the electronic configuration of the NV ground state (see Fig. 1.2(b)). The $|a_1'\rangle$ and $|a_1\rangle$ orbitals are fully occupied, and there are two unpaired electrons in the degenerate $|e_x\rangle$ and $|e_y\rangle$ states. Considering the orbital and spin degrees of freedom, we can construct the following candidate antisymmetric states for the NV electrons:

$$|orbital\, singlet\rangle \otimes |spin\, triplet\rangle$$
$$|orbital\, triplet\rangle \otimes |spin\, singlet\rangle$$

The energies of the six states are determined by the coulomb interaction and the spin-spin dipole interaction between the two electrons. Knowing that the coulomb interaction is stronger, we can infer that the orbital singlet $(|e_x\, e_y\rangle - |e_y\, e_x\rangle)$ state, with lower spatial overlap, will have lower energy than the orbital triplet state. **Therefore, the electronic ground state of the NV center is an orbital singlet and spin triplet ($S = 1$) state**:

$$\left|^3A_2\right\rangle = (|e_x\, e_y\rangle - |e_y\, e_x\rangle) \otimes |S = 1,\, m_s\rangle \tag{1.5}$$

This state is called $A_2$ because of its transformation properties under $C_{3V}$ operations.

The energies of the triplet sublevels are determined by the spin-spin dipole interaction between the two electrons. Here too, we can make a heuristic argument to know the relative energies of the three states. First, note that the N-V axis is the quantization axis of the spins (essentially, $S_z$ of the electrons will be either "up" or "down" along the NV axis) (Fig. 1.3 (a)). Second, the $|e_x\rangle$ and $|e_y\rangle$ orbitals comprise the Carbon dangling bonds, so the electrons will be dispersed along the $XY$ plane of the defect. In this configuration, one can imagine that having the two electron spins align (both pointing "up" or "down" along the NV axis)

will have higher interaction energies than having them anti-aligned. Therefore, the $|m_s = 0\rangle$ state will be lower in energy than the $|m_s = \pm 1\rangle$ states. In practice, we model the $|m_s = \pm 1\rangle$ states as degenerate and separated by the $|m_s = 0\rangle$ state by 2.87 GHz (Fig. 1.3(b)).

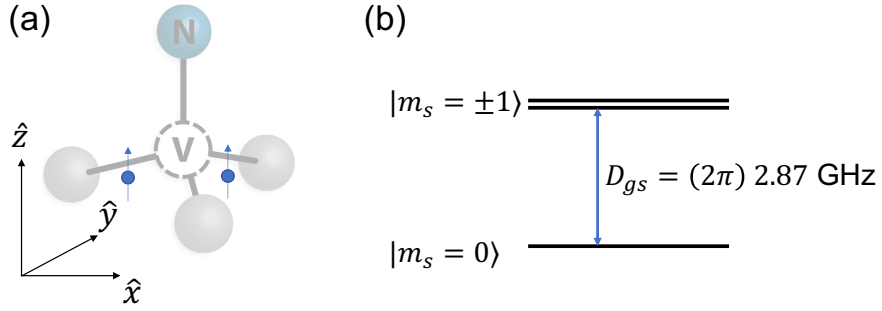


Figure 1.3: **NV ground state spin:** (a) The coordinate system associated with the NV center showing the quantization axis of the electronic spin. The NV center is symmetric with respect to 120° rotations around the $\hat{z}$ axis, and the reflections across planed formed by the Nitrogen-Vacancy-Carbon lattice points. The ground state $|e_x\rangle$ and $|e_y\rangle$ orbitals are linear combinations of the Carbon dangling bonds. Therefore, the ground state electronic configuration is dominantly distributed across the planar region formed by the carbon orbitals with their spin oriented along the $\hat{z}$ axis. As a consequence, when the spins are aligned ($|m_s = \pm 1\rangle$ states), their dipole-dipole interaction energy is higher than when they are anti-aligned. (b) The ground state spin sublevels are split by $D_{gs} \approx (2\pi) \times 2.87\,\text{GHz}$ GHz with the $|m_s = \pm 1\rangle$ states being degenerate to each other. Given that $D_{gs}$ corresponds to a temperature of 140 mK, the ground state spins are fully mixed at room temperature with 1/3 of the population in each spin state. The ground state hamiltonian is $H = D_{gs} S_z^2$ where $D_{gs}$ is called the zero-field splitting.
**Note:** I will use lower case $(\hat{x}, \hat{y}, \hat{z})$ to refer to the reference frame of the NV center and upper case $(\hat{X}, \hat{Y}, \hat{Z})$ to refer to the lab frame. This will be important in the discussion of stress sensing and vector magnetometry. In some cases, the two reference frames are coincident, but this may not be true in general.

### Why the NV$^-$ center?

As mentioned earlier, almost all applications of the NV center involve the negatively charged NV$^-$ center. The superior spin coherence properties of the NV$^-$ center stem from an effective decoupling of the spin and orbital degrees of freedom. Consider spin-orbit couplings of the form $L_\pm S_\mp$ that act on the system. The ground state of the NV$^0$ center is an orbital doublet ($|e_{x,y}\rangle$) with spin 1/2. Since the orbital states are subject to phonon-mediated decoherence [52], any spin-orbit coupling can have parasitic effects on the spin coherence of the system. In contrast, the ground state of the NV$^-$ center, being an orbital singlet, is unaffected by such

spin-orbit coupling terms. This isolates the $NV^-$ spin from phonon-induced decoherence mechanisms. Throughout this thesis, the NV center will exclusively refer to the $NV^-$ center.

### The NV excited state

The electronic excited state of the NV center involves the promotion of an electron from the $|a_1\rangle$ orbital to either the $|e_x\rangle$ or $|e_y\rangle$ orbitals (Fig. 1.2 (c)). Here too, we can use the same procedure to construct the singlet and the triplet excited states. In particular, the triplet excited state manifold ($^3E$) comprises six states which are linear combinations of the following orbital, and spin degrees of freedom [23]:

$$\left\{ \begin{array}{l} (|a_1\, e_x\rangle - |e_x\, a_1\rangle) \\ (|a_1\, e_y\rangle - |e_y\, a_1\rangle) \end{array} \right\} \otimes |S = 1,\, m_s\rangle$$

The relaxation between the $^3E$ manifold and the $^3A_2$ ground state is responsible for the NV center's fluorescence (Fig. 1.4). At room temperature, all the optical lines between the ground state and the excited state are broadened into a single zero phonon line (ZPL) at 637 nm . However, a majority of the photoluminescent emission of the NV center is contained in a broad phonon sideband (PSB) extending up to $\sim 900$ nm. The relaxation from the $^3E$ excited state to the phononic excitations of the $^3A_2$ ground state contributes to this sideband emission [29].

## Dynamics of the NV center

In this section, I will cover the photophysics of NV fluorescence, building on our understanding of the NV level structure (Fig. 1.4). In practice, we 'talk' to the NV center by exciting the optical transition from $^3A_2 \rightarrow {}^3E$ and collecting the fluorescent photons emitted by the NV center as the electron relaxes back to the ground state. Green light at 532 nm is optimal for excitation because it also stabilizes the $NV^-$ charge state over the $NV^0$ charge state. The **fluorescent transition** back to the ground state is **spin conserving**, implying that repeated cycles of excitation and relaxation will not alter the spin state populations of the NV center.

In addition to this fluorescent **(radiative)** relaxation, electrons with $|m_s = \pm 1\rangle$ states of the $^3E$ manifold can transition into $^1A_1$ singlet state. This **non-radiative transition** (which roughly occurs for $\sim$ 30% of the excitation cycles in the $|m_s = \pm 1\rangle$ spin states) is mediated by spin-orbit coupling [45]. Within the singlet manifold, there is an additional fluorescent line at 1024 nm from the $^1A_1 \rightarrow {}^1E$ state, which is filtered out in our experiments. The electrons can transition from the $^1E$ state back into the $^3A_2$ ground state through an additional non-radiative decay channel. The branching ratio for this transition marginally favors the electronic relaxation into the $|m_s = 0\rangle$ spin state in the ground state manifold (as shown by the darker arrow in Fig. 1.4) [29, 45]. This overall relaxation from the $^3E$ state to the $^3A_2$ ground state via the singlet manifold is called the **intersystem crossing** (ISC).

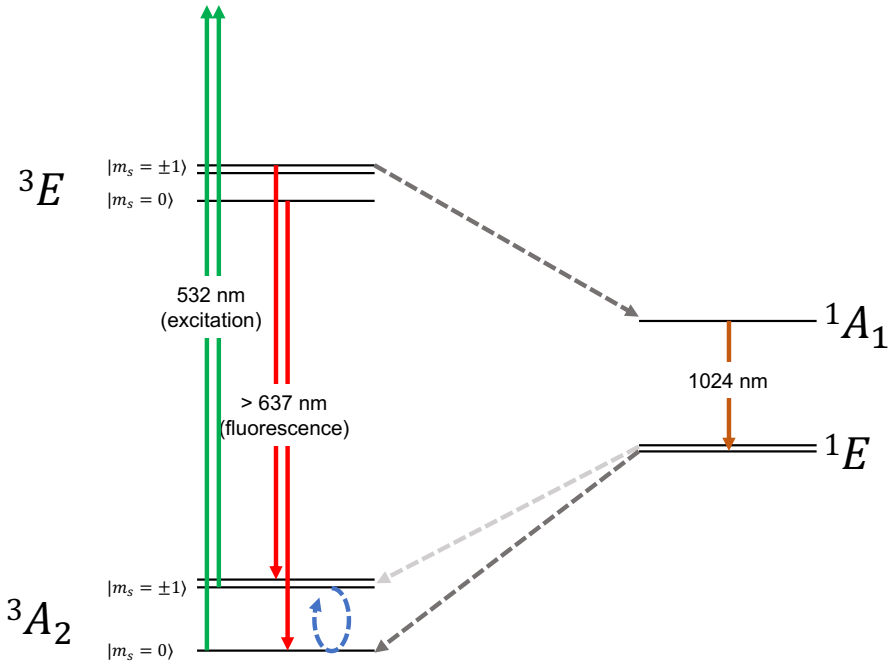


Figure 1.4: **NV ISC mechanism:** Electrons in the ground $^3A_2$ state are off-resonantly excited using a 532 nm beam to the $^3E$ excited state. The excited state has a lifetime of $\sim$ 10 ns at cryogenic temperature, and the electrons can fluoresce back into a ground state, releasing a red photon ($637 - 900$ nm). For the $|^3E, m_s = \pm 1\rangle$ states, complementary to this radiative spin conserving process, the electron can non-radiatively transition into the $^1A_1$ state in the singlet manifold. An additional fluorescence line at 1024 nm in the singlet manifold is filtered out in the experiments. The branching ratio of the second non-radiative relaxation path from the single $^1E$ states back to the ground state marginally favors the electronic population in the $|^3A_2\, m_s = 0\rangle$ state. The microscopic mechanism for this process is believed to be due to a stimulated phonon emission process [100]. This intersystem crossing mechanism, occurring over a timescale of $\sim$ 300 ns, is crucial for optical pumping and spin state readout of the NV center. In addition to optical transitions, the NV center also shows ground-state spin coherence. Using MW radiation, we can induce coherent oscillations among the $|^3A_2, m_s\rangle$ spin states (blue dashed arrow) - a mainstay of the NV center's room temperature quantum applications.

The ISC mechanism plays a central role in the NV center use in quantum technologies due to the following:

- **Optical pumping to** $|m_s = 0\rangle$: The upper branch of the ISC ($^3E \rightarrow^1 A_1$) is spin selective [45]. In comparison, the transition rates from the $^1E$ singlet to the $^3A_2$ spin states are comparable [100]. It is easy to imagine that over multiple cycles of exci-

tation, electrons in the $|^3A_2, m_s = \pm 1\rangle$ states will progressively get pumped into the $|^3A_2, m_s = 0\rangle$ state. Therefore, the ISC mechanism is key to state preparation of the NV center.

- **Spin state readout**: The lifetime of the $^3E$ excited state is $\sim 10\,\text{ns}$ whereas that of the $^1E$ singlet state is $\sim 370$ ns at cryogenic temperatures [100]. Given that relaxation through the ISC path is non-radiative (non-fluorescent), one can infer that the $|^3A_2, m_s = 0\rangle$ will be brighter than the $|^3A_2, m_s = \pm 1\rangle$ states. In experiments, measuring the fluorescence contrast (relative difference in fluorescence) enables us to perform spin state readout of the NV center.

#### Electron spin resonance

**Coherent control of the NV center's ground state spin *at room temperature* is a key advantage in its use in quantum technologies.** The depolarization time ($T_1$) of the NV center is on the order of milliseconds ($\sim 1$ ms) [54], and the decoherence time ($T_2$) can be pushed to $\sim 100\,\mu$s using clever dynamical decoupling techniques [22]. Essentially, this means that within the ground electronic $^3A_2$ state, one can use microwave (MW) radiation to induce transitions between the $|S = 1,\, m_s\rangle$ sublevels unlocking the capability of performing a plethora of NMR-type measurements with the NV's electronic spin.

## How to set up a Confocal NV experiment

Equipped with an understanding of the NV center and its amazing properties, our task then is to build an apparatus that is capable of making measurements. At a minimum, we need to be able to:

- Excite the NV center from the $^3A_2 \rightarrow {}^3E$ state for optical pumping
- Collect and measure the fluorescence from the NV center
- Apply microwaves (MW) at $\sim 3$ GHz for spin state manipulation

In practice, the most common design for an NV experimental setup is a scanning confocal fluorescence microscope integrated with MW control. The optics is reasonably straightforward, and a seasoned experimentalist can easily build an NV experiment in a couple of days (if not a few hours). A schematic for the experiment is shown in Fig. 1.5 with the setup details included in the figure caption.

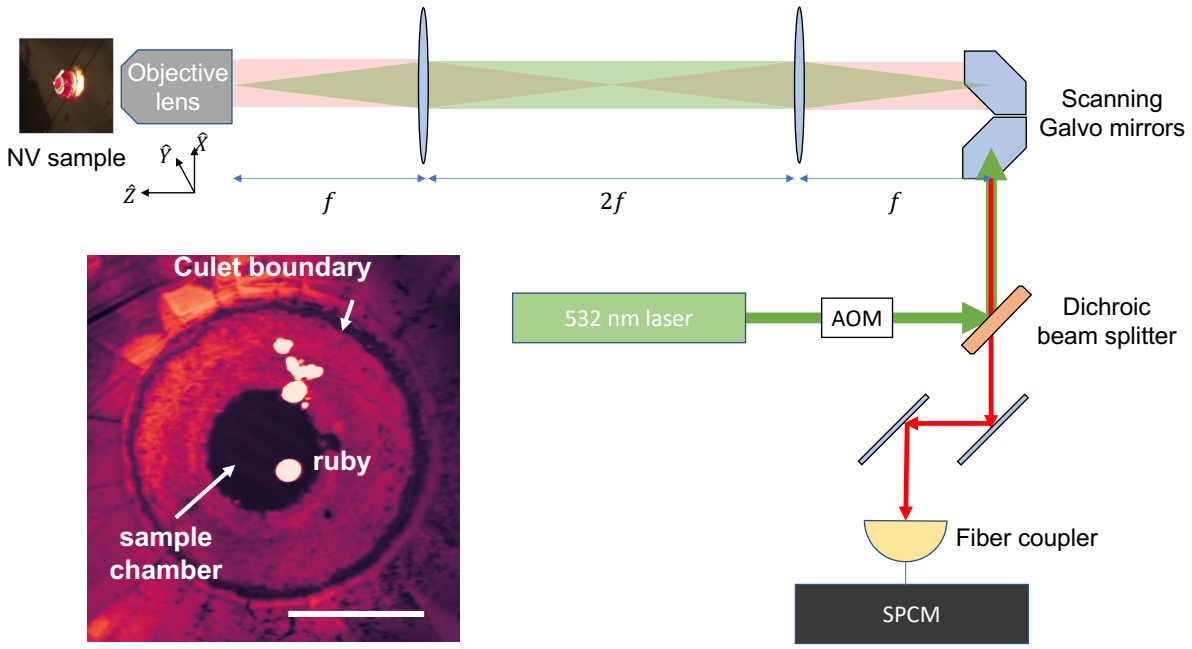


Figure 1.5: **Schematic of a confocal NV fluorescence microscope:** The beam of a 532 nm laser (Coherent Compass 315M or Coherent Verdi V-2), switched by a double pass AOM (Gooch & Housego AOMO 3110-120) setup, is directed towards a pair of scanning galvo mirrors (Thorlabs GVS212) using a dichroic beamsplitter (Semrock FF552-Di02). Following the galvo, a $4f$ telescope comprising two converging lenses is used to focus the excitation beam (green) onto the rear window of a high NA objective lens (typically a Mitutoyo M Plan APO long working distance objective). The voltage-controlled galvo mirrors raster the excitation beam in XY while the $4f$ system fixes the focus of the beam at the objective entrance enabling one to scan the excitation laser over the sample region. Scanning in the Z axis is enabled by a piezo objective mount (Edmond Optics nanopositioning piezo actuator) with 100 $\mu$m range. The NV fluorescence (red beam) at the sample captured over some solid angle by the objective counter propagates along the excitation path. The dichroic beam splitter transmits the fluorescence beam, and additional filters are used to chop out parasitic excitation photons and $NV^0$ fluorescence. The fluorescence beam is then coupled to a fiber (the fiber core acts as the pinhole in our confocal setup). In all experiments, a single photon counter (Excelitas SPCM-AQRH-64-FC) was used to measure the fluorescence signal. (bottom left) A sample NV fluorescence scan of a pressure loading is shown. One can clearly see the culet and facets of the diamond anvil as well as the sample chamber and ruby pressure marker. White scale bar shows 100 µm.

In this thesis, most of the data taking was shared between two confocal setups (the first at room temperature and the second integrated with an Attocube attoDRY 800 cryostat). Additionally, for some experiments, we took data on a room temperature widefield setup.

The details thereof are relegated to a later chapter to be explained in the context of the experiment (Chapter 5).

To integrate MW control into our confocal setup, we used a stripline or wire near the NV sample as a MW antenna. We performed spin state manipulation by channeling high-power microwaves through the antenna. Fig. 1.6 shows a schematic of the MW circuit used in our experiments with the relevant details in the figure caption.

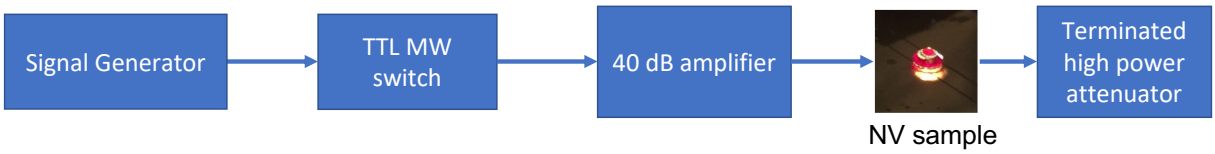


Figure 1.6: **MW setup**: A microwave signal generator (SRS SG386 or SG384) is used for both pulsed and continuous wave experiments. A MW switch (Minicircuits ZASWA-2-50DR) is used to shutter any spurious leakage in the MW channel. A high-power class A amplifier (Minicircuits ZHL-15W-422-S+) is used to amplify the MW prior to channeling the radiation to the NV sample. Downstream from the sample, a 50Ω terminated high power attenuator (Minicircuits BW-N40W50+) is used to absorb the MW signal to prevent any reflection back to the sample.

## 1.3 Measurements using the NV center

In this section, I will detail two main measurement schemes employed in NV (and other NMR-like) systems. Instead of being comprehensive and going into the details of sensitivity and SNR, my motivation will be to give a sense of what the measurement protocol entails and how the measurement signal is obtained. Detailed descriptions of measurement sensitivity can be found in [9].

### Continuous wave experiments

The majority of the experiments in this thesis are continuous wave optically detected magnetic resonance (cwODMR) measurements. ODMR implies that magnetic dipole transitions in the ground state spin manifold are detected optically using a fluorescence contrast measurement. During a cwODMR measurement, the excitation laser is always ON. Under this condition, one can model the optical pumping process as a competition between the fluorescent relaxation and ISC transitions, yielding a steady state population of ground state spins. The majority of the NV spin populations will be in the $|m_s = 0\rangle$ state. We now apply microwaves and tune the MW frequency across the ground state zero-field splitting. On resonance, the MW will induce a transition from $|m_s = 0\rangle \leftrightarrow |m_s = \pm 1\rangle$. This will offset the steady-state populations and reduce the overall fluorescence of the NV center. In

Fig. 1.7 (a), a cwODMR signal at 120 GPa shows two such resonance peaks stemming from transitions from the $|m_S = 0\rangle$ state to eigenstates in the $|m_S = \pm 1\rangle$ manifold under stress. Therefore, by measuring the fluorescence synchronously with a change in the MW frequency, we can optically detect the NV electrons' magnetic resonance signal.

## Pulsed experiments

The cwODMR measurement described above is an incoherent process. In contrast, pulsed measurements leverage the coherence of the spin levels. Instead of trying to explicate the expansive arsenal of pulsed measurements available to us, I will only describe a simple Rabi measurement to provide an idea of how pulsed measurements work in practice. Very broadly, it can be broken down into three steps:

- **State preparation**: This step generally involves $\sim 100\,\mu$s long laser pulse to prepare the NV in the $|m_s = 0\rangle$ state. If required, a calibrated MW pulse can subsequently be used to prepare the system in any of the spin states or a coherent superposition thereof. A wait time is generally included to control for any charge dynamics in the system following the long laser pulse as well as for electrons in the singlet state to relax back into the ground state manifold.

- **MW pulse sequence**: A sequence of choice can be applied to the NV center to direct the time evolution of the spin states, decouple environmental noise, etc. In reality, this sequence can be as simple as a MW pulse with a fixed frequency applied for a varying duration (in the case of the Rabi measurement) or a complicated sequence of pulses for simulation or sensing [9].

- **Readout**: In the final step, we measure the fluorescence of spin state as an indicator of the population in different spin sublevels. A readout pulse is generally calibrated to be about $\sim$1 µs.

- **Readout Reference**: A second reference pulse is taken after the readout pulse to correct for fluctuations in laser power and other experimental factors (such as drift in the optical alignment). The reference pulse provides an estimate of the background fluorescence when the NV spin is in the $|m_s = 0\rangle$ state. The ratio of the raw readout counts and the reference counts yields a better estimate of the final state populations in practice.

In the Rabi experiment, starting in the $|m_s = 0\rangle$ state, a resonant MW pulse can cycle the spin between $|m_s = 0\rangle \leftrightarrow |m_s = \pm 1\rangle$ states. We can directly see this when we plot the normalized readout counts against the length of the MW pulse. The strength of the magnetic dipole coupling of the NV center to the applied MW pulses defines the frequency of this oscillation (called the Rabi frequency). The decaying envelope of the Rabi signal defines the dephasing $T_2^*$ timescale.

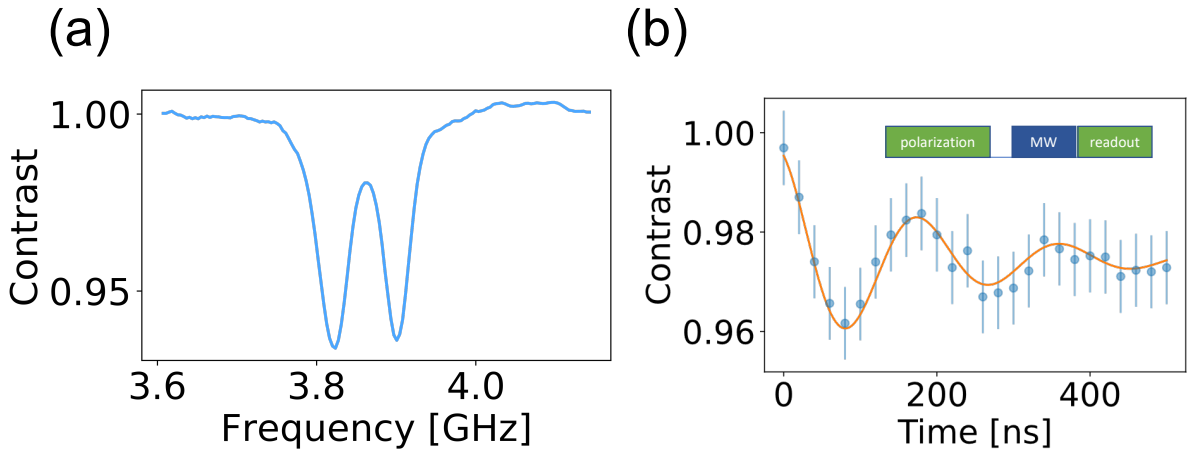


Figure 1.7: **NV measurements at** $\sim$ 120 GPa**:** (a) A room temperature cwODMR spectrum at high pressure showing the resonances between the ground state $|m_s = 0\rangle$ and $|m_s = \pm 1\rangle$ states. The $|m_s = \pm 1\rangle$ states are shifted, split, and mixed due to crystal stress. (b) A low-temperature Rabi measurement at the same pressure: The pulse sequence for a Rabi experiment (inset) starts with a polarization pulse to prepare the NV center in the $|m_s = 0\rangle$ state. Following a short wait time, a MW pulse at the resonance frequency is applied for a variable time. A state readout pulse shows rabi oscillations as a function of the length of the MW pulse. A second reference readout pulse (not shown) can control for drift in NV counts over the course of the data taking.

#### Single NV vs. Ensemble measurements

A second distinction must be made regarding the types of NV measurements. On the one hand, experiments can use a sample rich in NV centers that measure more than $\sim$ 1000 NVs in one diffraction spot [49]. Alternatively, one can use a sparse sample where experiments measure the behavior of individual NV centers. The former is an ensemble measurement, whereas the latter is a single NV measurement. Each type of measurement has its tradeoffs pertaining to SNR, sensitivity, and integration time. The right choice will necessarily depend on the goals of the project. In this thesis, all high-pressure experiments are ensemble experiments.

## 1.4 NV sensing: Vector Magnetometry

In this section, I will show how the tools introduced so far can work in concert to make meaningful measurements. Barry *et al.* [9] give a thorough review of NV sensing protocols from the standpoint of sensitivity improvement. Here, I will only provide a simple illustration

of vector magnetometry to show the concept and usefulness of NV sensing at a high level. In particular, I hope to impress upon the reader that one can leverage ensemble NV sensing to reconstruct vectorial and tensorial information of the parameter of interest. I have often found myself using this technique in the lab, and my hope is to demystify the procedural steps involved.

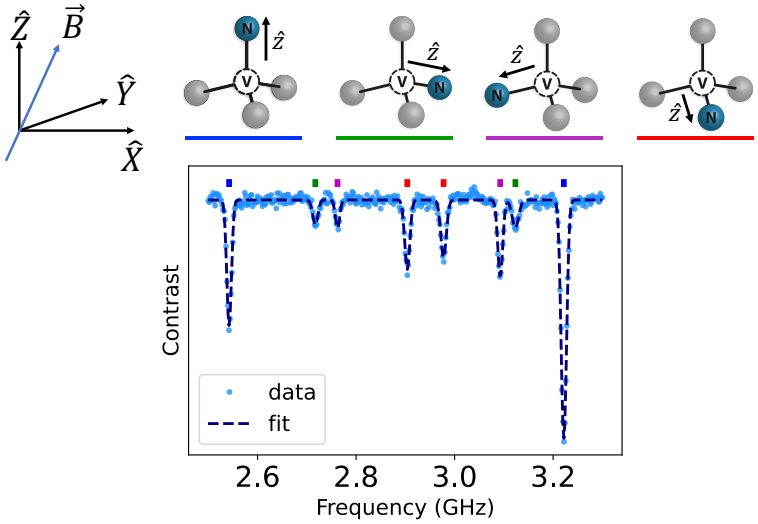


Figure 1.8: **Vector magnetometry:** There are four groups of NV centers in diamond with the N-V axis oriented along each of the four diamond bonds. The ground state spin of each group is quantized along its respective NV axes ($\hat{z}$). In this figure, the four groups are depicted in terms of their crystal orientation (top). The application of a generic $\vec{B}$ field (shown in the crystal frame on the top left) will result in eight resonance lines (two for each NV group) in a cwODMR spectrum. This is because the magnitude of the field projection in the frame of each NV group will determine the shift and splitting of these lines. In the ODMR spectrum, the lines from each group are paired and denoted by the color associated with each group. The four groups are ordered according to the magnitude of the field projection in their respective frames.

In practice, the quantization axis ($\hat{z}$) of an NV center can be oriented along any of the four bonds in the diamond crystal. Pictorially, this translates to the nitrogen-vacancy axis lying along this bond (Fig. 1.8). Therefore, there are four different NV groups in a diamond sample with tetrahedrally oriented quantization axes. In the presence of a generic magnetic field, the NV groups couple to the projection of the $\vec{B}$ field in its reference frame, yielding the following Hamiltonian for the system:

$$H = \sum_{i=1,2,3,4} D_{gs}\, S_{z,i}^2 + \gamma \vec{B}^{(i)} \cdot \vec{S}_i \tag{1.6}$$

where $D_{gs} = (2\pi) \times 2.87\,\text{GHz}$ is the zero field splitting, $\gamma \sim (2\pi) \times 2.8\,\text{MHz/G}$ is the gyromagnetic ratio, and $\{S_{x,i}, S_{y,i}, S_{z,i}\}$ are the spin-1 matrices for the $i$-th NV group. Intuitively, the field projection along $\hat{z}^{(i)}$ couples linearly, causing a Zeeman splitting of $2\gamma B_z^{(i)}$ between the $|m_s = \pm 1\rangle$ spin states. In contrast, the off-axis components $(B_x^{(i)}, B_y^{(i)})$ are suppressed by the zero-field splitting term and perturbatively couple at second order (at low fields). These off-axis fields result in a shift and a splitting of the order $\sim (\gamma\, B_{x,y}^{(i)})^2 / D_{gs}$. Therefore, the application of a non-degenerate $\vec{B}$ field will yield eight resonances in the ODMR spectrum (two from each of the NV groups as in Fig. 1.8). For each group, it is possible to fit $B_z^{(i)}$ and $B_\perp^{(i)} = \sqrt{B_x^{(i)\,2} + B_y^{(i)\,2}}$ from the shift and the splitting values. Reconstructing the three free parameters of $(B_X, B_Y, B_Z)$ in the lab frame from these eight resonances can then be relegated to an optimization routine.

**Note:** As mentioned earlier, I will use upper case $(\hat{X}, \hat{Y}, \hat{Z})$ for the lab reference frame and lower case $(\hat{x}, \hat{y}, \hat{z})$ to denote the reference frame of a single NV group. Except for special cases, the two frames are not coincident.

## 1.5 What is this thesis about?

Abstracting away the experimental details, we can think of the NV center as a spin 1 defect in diamond, with three quantum states that can be reliably **initialized**, **coherently controlled** and **measured**.

On the one hand, this thesis details the work done to extend the validity of this abstraction to pressure scales of $\sim 100$ GPa (1 megabar). Being able to do so is crucial for unlocking the sensing capabilities of the NV center, hitherto demonstrated under ambient conditions, to explore the rich world of high-pressure phenomena.

On the other hand, this thesis also highlights some unique new capabilities that the NV center brings as a high-pressure metrology tool. The ability to make spatially resolved measurements and sense both uniaxial and deviatoric stresses is complementary to more conventional high-pressure probes, thereby augmenting our ability to answer meaningful scientific questions in this realm.

I hope future high-pressure physicists will find something useful here to make measurements for their research work.

# Chapter 2

# The diamond anvil cell

I can neither confirm nor deny whether an anonymous researcher once told me, "I would rather not work than do that!" (referring to loading DACs).

Having covered NV centers in the previous chapter, my intention in this short chapter is to provide a primer on diamond anvil cells (DAC) and high pressure physics. In the same vein, my objective here is to help the beginning student learn the methods of DACs to get their hands dirty and start taking data. Although preparing a pressure loading can be a painstaking and underappreciated process, there is no better mantra than trying things out and failing one's way to success!

## 2.1 A (very) brief history

The storied history of the diamond anvil cell can be a fascinating read [12] when grappling with shattered diamonds. Around 1949, researchers at the University of Chicago started to realize the usefulness of using diamonds in high pressure research. Almost a decade later, in 1958, Charles Weir at the National Bureau of Standards (NBS) made the first diamond anvil cell. Interestingly, researchers at NBS had access to confiscated contraband jewelry diamonds that (coincidentally) were ideal for high pressure work. However, during this period, the idea of leveraging the transparency of diamonds to directly look at the sample eluded researchers. Alvin Van Valkenburg is credited to have serendipitously discovered this fact in 1958, thereby birthing our current idea of a diamond anvil cell. Looking through his diamond anvil loading to check for alignment, Valkenburg directly observed phase separation of his high pressure sample. To study materials under quasi-hydrostatic pressure, Valkenburg is also credited to have pioneered the gasket technique that is now routinely used in practically all high pressure loadings.

In geophysics, where one is interested in phases of matter in planetary interiors, high pressure is often quoted in gigapascals (GPa), with $1\,\mathrm{GPa} = 10.000\,\mathrm{atm}$ and the pressure at the center of the Earth being $\sim 360$ GPa. The earliest explorations in DACs were able to achieve a few GPa of pressure (an enormous feat at the time) [12]. Nevertheless, one of the

clear directions in high pressure research was making this journey to the Earth's center (on the pressure scale). The impressive push to megabar (Mbar) pressures (1 Mbar = 100 GPa), along with conclusive calibration techniques, was developed by Dave Mao and Peter Bell [12, 70]. Even before this, however, many ideas were already put forth to explore the colorful world of high pressure phases. In particular, in 1968, Neil Ashcroft proposed the possibility of high temperature superconductivity in a high pressure metallic phase of Hydrogen [6].

Metallic Hydrogen became a unicorn of sorts, driving researchers to achieve higher and higher pressures on one hand and adding fuel to the search for high temperature superconductors on the other [13]. This decades-long effort was reignited with recent breakthroughs in superhydride materials [32, 33, 95]. The starting point of our project to explore NV sensing under pressure coincided with the discovery of high temperature superconductivity in $H_3S$ above 100 GPa pressures by Mikhail Eremets' team [32]. Our initial motivation to push NV sensing to megabar pressures was fueled by all the interest and activity in high-pressure hydrides with the dream of imaging the Meissner effect in these systems.

In discovering DACs, Valkenburg's key breakthrough was the realization that he could do meaningful science simply by looking through the diamond and mapping the high pressure chamber. In some sense, the NV center empowers us to continue on this path by opening a new window to directly image the magnetic and stress fields in the anvil.

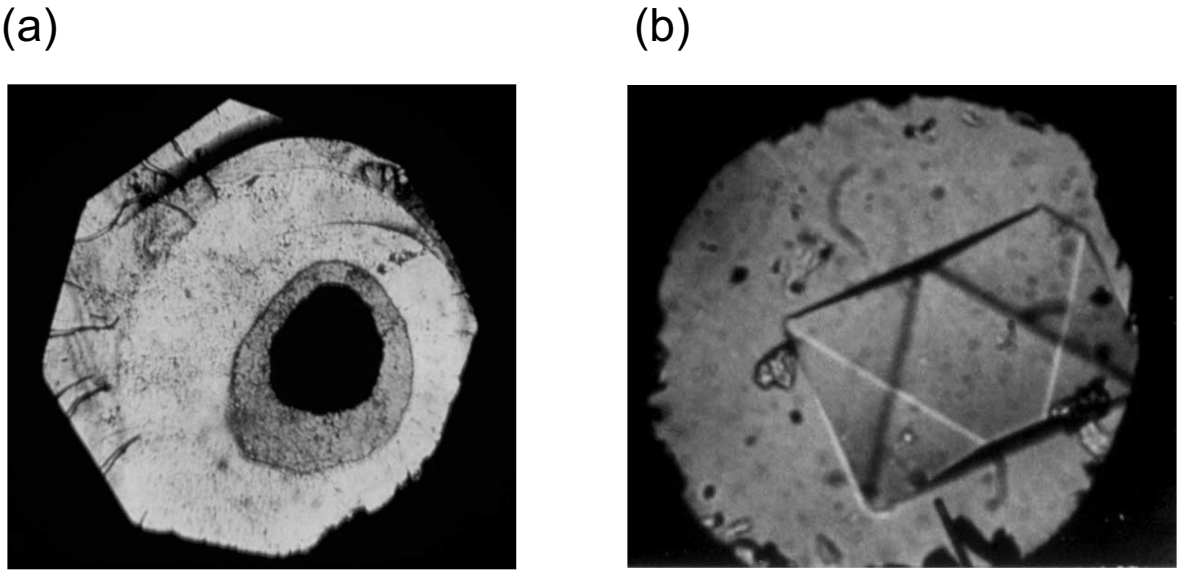


Figure 2.1: **Valkenburg's original pictures of DAC loadings (images adapted from [12])**: (a) A loading of copper bromide nucleation of a high pressure phase (dark). (b) A pressure loading with water at room temperature showing an octahedron phase of ice VI.

## 2.2 The design of a diamond anvil cell

The basic idea of a diamond anvil cell is very intuitive. Two opposing gem-cut diamonds with flat culets are pressed together to create a high pressure region. The sample, enclosed at the center of a metal gasket, is sandwiched between the culet faces of the diamond. In our experiments, the gasket was fashioned out of rhenium foil by pre-indenting up to $25-30$ GPa and subsequently drilling a hole in the center of the indent. Fig. 2.2 (a) and (b) show a standard schematic of a diamond anvil and a DAC setup.

Belying this simplistic notion, DACs come in many shapes and sizes catering to the needs of a particular experiment, varying in both the design of the cell body and the diamond anvil itself. During my graduate study, I had the opportunity to work with three different DACs:

- **Pasternak DAC:** This miniature cryo DAC was designed by Moshe Pasternak and subsequently lent to the group by Prof. Raymond Jeanloz. The Pasternak cell was the workhorse for our initial pressure loadings and early demonstrations of NV sensing under pressure (Chap. 3). The cell body is a variation of the plate DAC design with two plates aligned by metal spokes and pressed against each other by six screws (Fig. 2.2 (c)). This design allows much space for circuits for MW delivery and transport measurements.

- **PPMS DAC:** This family of cells was lent to us by Prof. Viktor Struzhkin early in the group's foray into high pressure. The cell body is a miniaturized design of a panoramic DAC originally fashioned by Prof. Alex Gavriliuk and Prof. Viktor Struzhkin [41]. The three DACs are 10 mm, 17 mm, and 23 mm in diameter with maximum pressures of 10 GPa, 100 GPa, and 200 GPa, respectively. These DACs (my favorites) were instrumental in my efforts to push to megabar pressures.

- **mini BX90**: Our effort to improve microwave delivery in the DAC for pulsed NV measurements under high pressure led us to experiment with a BX90 piston-cylinder DAC design. The starting point was a 1.5 inch mini BX90, made of beryllium copper (BeCu), lent to us by Prof. Leonid Dubrovinsky [56]. The symmetric design of this cell can achieve higher pressures than a Pasternack cell while providing ample working space for incorporating MW circuits.

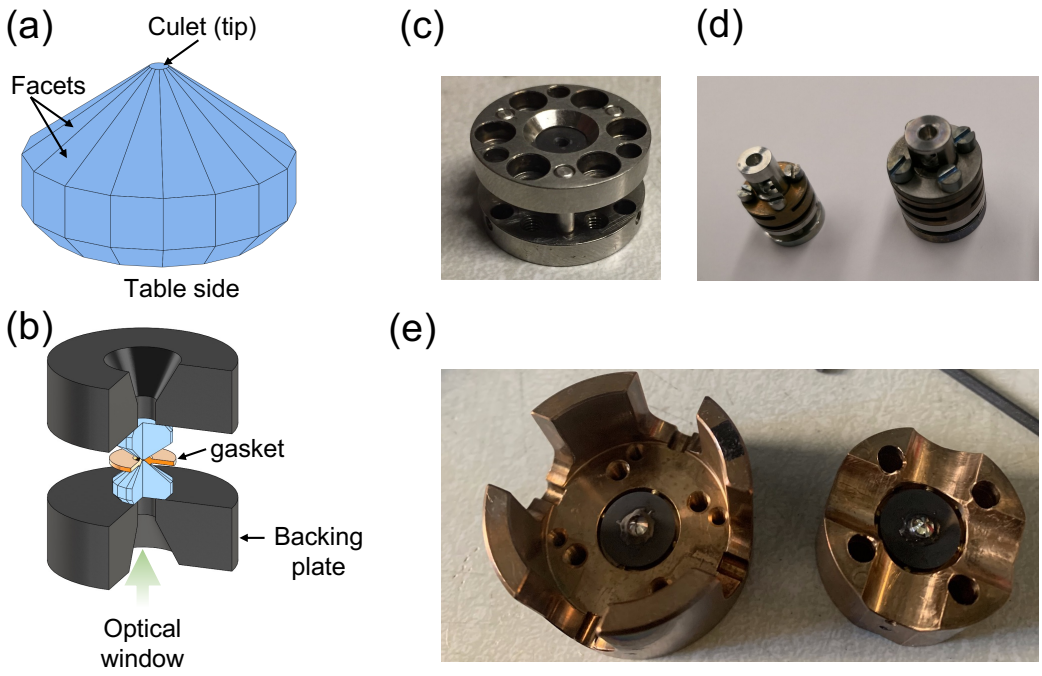


Figure 2.2: **DAC design:** (a) A standard gem cut diamond anvil showing the base (table side) and a flat culet. Most of our experiments used this kind of anvil design with 200 $\mu$m culets with 16 facets. At its widest, the girdle of the diamond anvil can be $\sim$ 3.25 mm. (b) A cartoon of a DAC loading with two opposing anvils and a gasket. The diamonds are glued to backing plates (seats) and subsequently aligned with the cell body of the DAC (not shown). An optical window allows us to perform confocal scanning through the table side of the diamonds. (c) a Pasternak DAC showing two plates with guiding rods and a cubic boron nitride (black) backing plate at the center. (d) 10 mm and 17 mm PPMS DACs designed by Viktor Struzhkin and Alex Gavriliuk [41] (c) a BeCu mini BX90 cell [56] showing the cylinder (left) and piston (right). Diamond anvils are glued to backing plates in both parts .

## 2.3 The apparatus of high pressure NV experiments

I will ink some lessons from Dr. Thomas Smart and Dr. Zachary Geballe, who provided me with invaluable guidance in my early days of working with DACs. I will use the mini BX90 DAC as an example. I will also consider flat culets, which can be safely pushed to $\sim$ 80 GPa pressures for compression and decompression studies. Each DAC has unique quirks and requirements for loading and alignment, and no one will master them without a few painful hours in the lab. Nevertheless, there are some common threads in the loading procedure.

### Gluing diamonds

Diamond anvils are aligned and glued to backing plates using Stycast® 2850FT in a gluing jig (Almax Diacell easyGlue). In all alignment steps, it is necessary to avoid parallax errors associated with the microscope. To this end, it is essential to align only along the vertical axis, while iteratively rotating the system by 90°. Alternatively, it is possible to entirely alleviate parallax errors by using a monocular microscope.

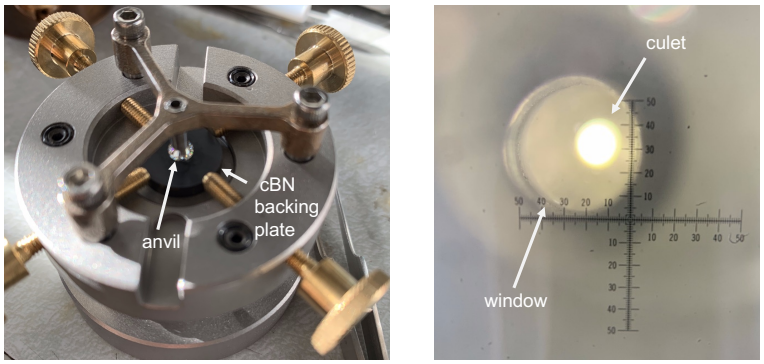


Figure 2.3: **Gluing anvils**: (Left) An Almax Diacell easyGlue jig holding a cubic boron nitride (cBN) backing plate and a diamond anvil. (Right) The optical window of the backing plate is aligned to the diamond culet using the four adjustment screws of the jig. To avoid parallax, we iteratively rotate the jig by 90° and vertically center the culet on the optical window. Even after full alignment, parallax in the microscope does not show the culet and window aligned along the horizontal axis. The diamond is glued to the backing plate by applying Stycast® 2850 FT around the table side of the anvil after alignment.

### Culet alingment

After centering and gluing the diamonds to their respective backing plates, the next step is to center the culets in the DAC. To start, we coarsely center the backing plates on the piston and cylinder of the DAC (Fig. 2.4 (a)). Closing the DAC *very carefully* to bring the culets near each other, we look through the optical window to inspect the alignment of the culet. In this step, the diamonds must not make forceful, direct contact with each other as they may easily crack! Inspecting from the side (Fig. 2.4 (b)) and through the optical window (Fig. 2.4 (c)), we can align the culets to each other. There are three aspects to consider at this step:

- **Positional alignment** is performed by moving the set screws holding the *bottom* backing plate. Again, one must avoid parallax error, using only the vertical axis of the microscope for alignment and rotating the DAC to ensure the culets are fully aligned. Fig. 2.4 (c) shows two misaligned culets, whereas (d) shows two culets that are aligned to each other.

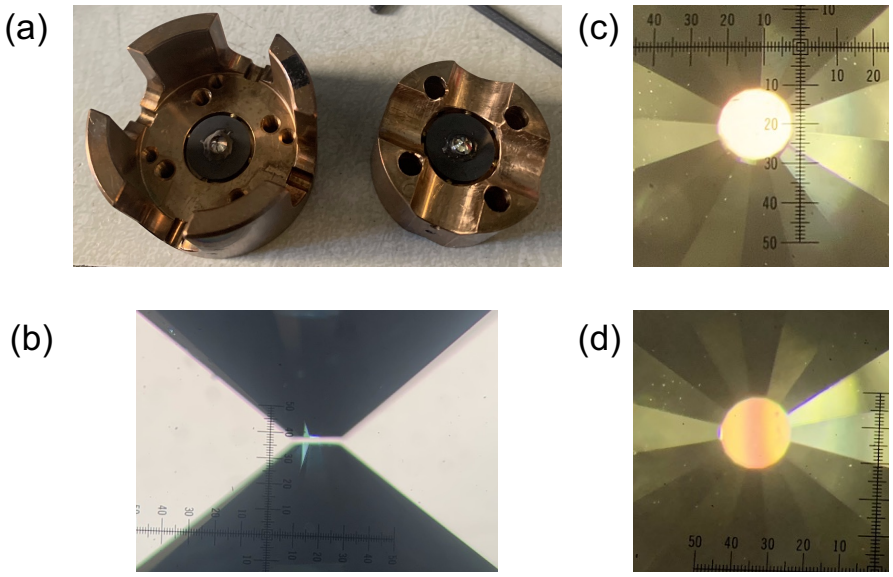


Figure 2.4: **Culet Alignment:** (a) The cylinder (left) and piston (right) of the mini BX90 cell show anvils glued to the cBN backing plates. (b) Closing the cell *very carefully*, we can inspect from the side to check for positional alignment of the culet. Diamond contact at this step can easily cause the culets to crack. (c) Inspecting through the optical window shows two misaligned culets. One can perform positional alignment by moving the *bottom* culet. (d) Two culets aligned in position and parallelism, as evidenced by a single interference fringe spread out over the culet.

- **Parallelism** between the culets is important for the stability of the sample chamber. Bringing the culets close together allows one to observe a repeating VIBGYOR interference pattern in a white light microscope. The worse the parallelism is between the culet faces, the more numerous and dense this pattern will be. Therefore, counting the number of interference fringes and inspecting their density provides a measure of the parallelism between the culet faces. Rotating one of the culet faces relative to the other, one can try to minimize the number of fringes to improve parallelism. Fig. 2.4 (d) shows a single interference fringe spread over the entire culet.

- **Rotational alignment** ensures that the culets are concentric with the cell body. I have not found this to be crucial for pressure loadings in practice. If necessary, this is achieved by iteratively rotating one of the backing plates followed by positional alignment to check for concentricity.

### Gasket

A gasket is used to laterally confine the sample in high pressure loading. The flow of the gasket under pressure creates a biaxial planar stress $\sigma_\perp = (\sigma_{XX}+\sigma_{YY})/2$ in the sample chamber. In conjunction with the uniaxial $\sigma_{ZZ}$ stress due to the anvils and a pressure medium, this creates a quasi-hydrostatic environment in the chamber. In most pressure loadings, a metal gasket is fashioned out of a foil of tungsten carbide (WC), steel, beryllium copper (BeCu), or rhenium (Re). The latter two are non-magnetic and, therefore, appropriate for studying magnetism at high pressure. An insulating gasket yielded the best results for NV experiments (Fig. 2.5).

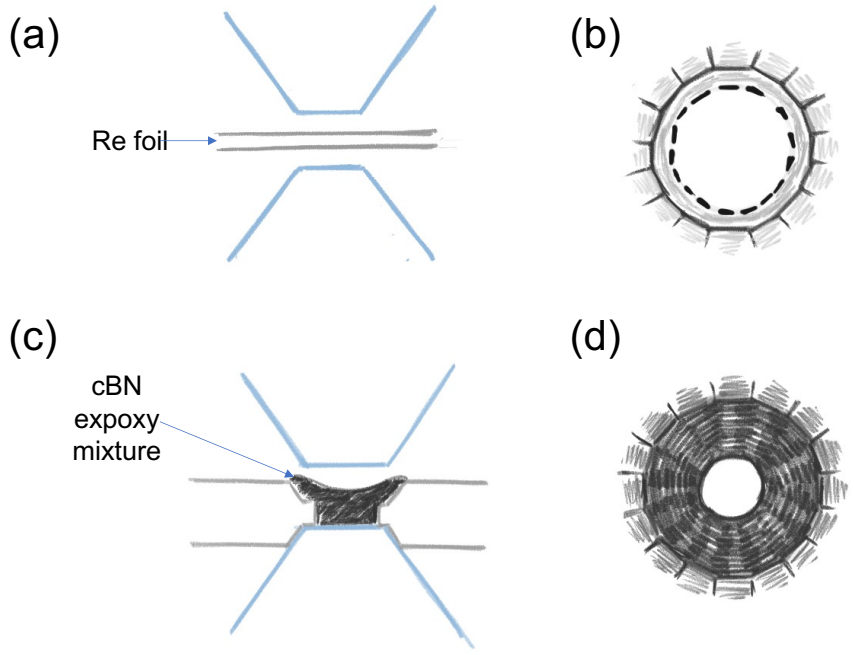


Figure 2.5: **Making insulating gaskets:** (a) A Rh foil is first pre-indented up to $\sim 30$ GPa. (b) The majority ($\sim 90\%$) of the culet area is drilled to avoid shorting under high pressure due to gasket flow. (c) The sample chamber is then packed with a powdered mixture of cBN (LANDS Superabrasives, Co.) and epoxy (EPO-TEK® 353 ND/A). This mixture is prepared by combining $2 \times 10^6$ mesh powdered cBN with epoxy in a $4:1$ ratio by mass. The dried paste is subsequently powdered in a mortar and pestle. (d) The mixture is compressed to $\sim 30$ GPa, and the sample chamber is punched out using a laser drill.

In this work, I used either insulating or rhenium gaskets. One can make an insulating gasket simply by pre-indenting a metal foil (Re) to 30 GPa and drilling out the culet area. Filling the sample area with a $4:1$ insulating mixture of cubic boron nitride (cBN) powder

and epoxy (EPO-TEK® 353 ND/A), a second indentation and drilling step (again to 30 GPa) is necessary to make an insulating gasket.

### MW wire

MW delivery is an *essential* component of an NV-pressure experiment. In practice, the current apparatus for MW delivery can be quite temperamental, and the best solution is yet to be ascertained. It can drastically reduce SNR and directly affect data quality and acquisition times if poorly implemented. In retrospect, I would say that this *the* part of the experiment consumed most of my time in the laboratory. Of course, the absence of eddy currents in insulating gaskets helps improve the MW signal at the culet. However, there is room for improvement in engineering a robust MW delivery system under extreme pressure and foolproof loading. The primary challenge is to overcome the multiple points of impedance mismatch along the circuit that result in the reflection of the microwaves. Fig. 2.6 shows a schematic of the MW loadings used in most experiments in this thesis.

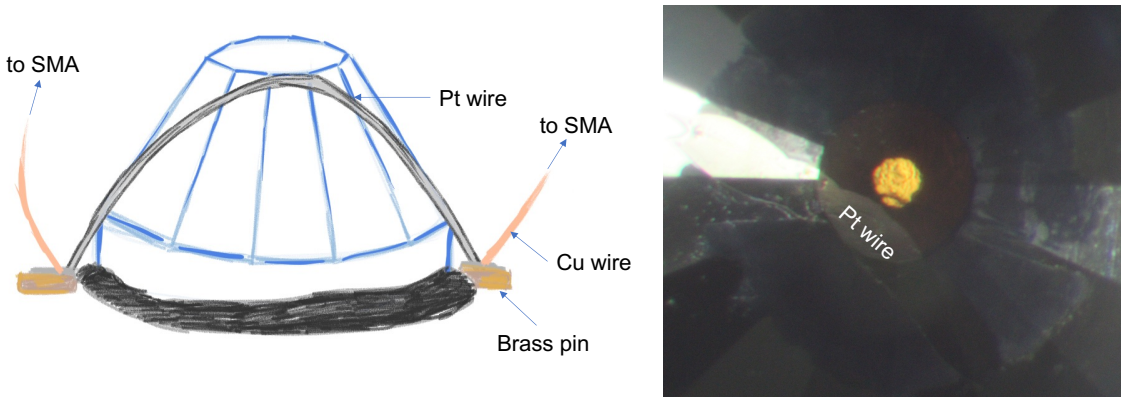


Figure 2.6: **MW delivery:** (Left) In our loadings, we used a wire cut out of 4 µm platinum (Pt) foil. The wire was draped over the anvil facets as close as possible to the sample chamber. The two ends of the wire were soldered to brass pins glued to the backing plate. Insulated copper (Cu) magnet wires were used to connect these pins to coax (SMA) cables for MW delivery to the DAC. (Right) For performing pulsed measurements, it is imperative to have MW wires as close as possible to the target NV centers in the sample chamber.

### Pressure medium

The pressure medium maintains a quasihydrostatic pressure environment in the sample chamber. Gaseous media such as nitrogen ($N_2$), helium (He), or neon (Ne) show low deviatoric stresses up to the highest pressures [70]. However, gas loading is non-trivial and requires specialized equipment. In practically all the experiments in this thesis, I used soft solids (salts such as cesium iodide and potassium chloride) as pressure media. For experiments going up

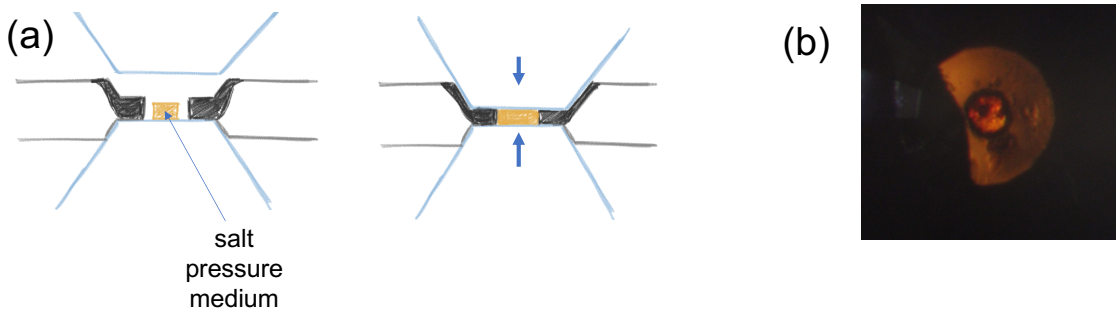


Figure 2.7: **Loading with salt:** Although fairly straightforward, loading with salt proved to be tricky for me in my first few attempts. The trick, as shown by Dr. Zachary Geballe, is outlined above. (a) A piece of salt roughly $\sim 80\%$ of the volume of the sample chamber is used. Filling the chamber with salt can cause the gasket to flow outward under pressure leading to the expansion of the sample chamber and failure of the pressure loading. Instead, this technique ensures the gasket flows inward, maintaining the integrity of the sample chamber. (b) The metalization of cesium iodide (CsI) can lead to absorption of 532 nm excitation light above $\sim 50$ GPa. Under white light illumination, the sample chamber appears red because of the absorption of short wavelengths at the onset of metalization.

to 100 GPa, it is best to use potassium chloride (KCl) because of the metalization of cesium iodide at $\sim 65$ GPa [104]. Fig. 2.7 shows the procedure for loading with salt.

## Pressure calibration

Ruby fluorescence [98] and culet Raman fluorescence are most commonly used for pressure calibration [36]. Interestingly, a confocal apparatus is fully compatible with both techniques requiring only a calibrated spectrometer for pressure calibration. In the case of pressure calibration with ruby fluorescence, the shift of the $R_1$ of ruby microspheres in the sample chamber can be used to track the pressure. At megabar pressures, diminishing brightness of the ruby fluorescence line becomes a challenge, and the Raman shift of diamond at the culet is commonly used for pressure calibration [2].

**Note:** NV centers can also be used as pressure calibrants capable of estimating hydrostatic and deviatoric stresses in the sample chamber. There are some empirical pressure gauges based on NV response for different crystal cuts. Although the empirical calibration of hydrostatic stresses is relatively robust to different samples and pressure media, the work in this thesis shows deviatoric stresses can be different for different media. In future work, there will be a need for careful calibration of both hydrostatic and deviatoric stresses for different pressure media and crystal cuts.

### Crystal cut of diamond anvil

Crystal cut of the diamond plays a crucial role in a high-pressure NV experiment by determining the orientation of the NV groups with respect to the loading axis. Anvils are commonly available in [100], [110] and [111] crystal cuts where $[a\,b\,c]$ represents the surface normal vector of the culet in the reference frame of the diamond crystal. From the standpoint of NV sensing, the right choice for crystal cut will depend on the goal of the experiment. I will circle back to this in section 6.5, providing here only an illustration of the geometry of the loading.

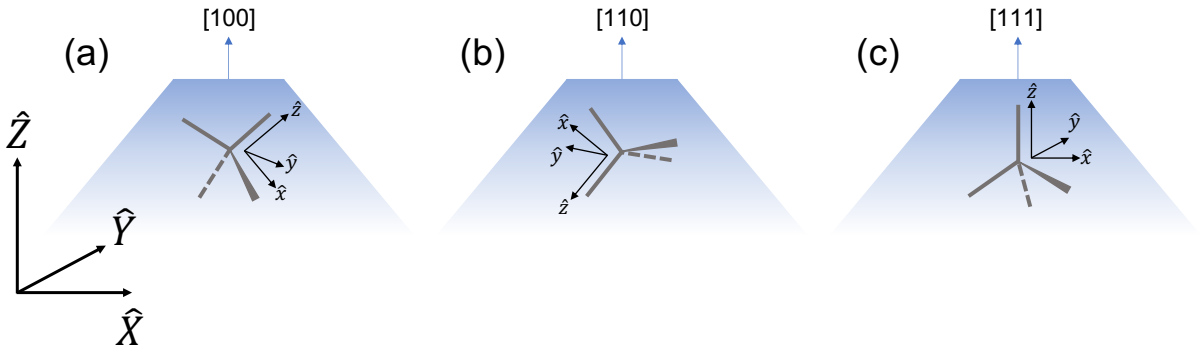


Figure 2.8: **Crystal cut of culet [75]:** The three main crystal cuts for diamond anvils are shown along with the orientation of the four NV groups therein. As a convention in this thesis, $\{\hat{X}, \hat{Y}, \hat{Z}\}$ represents the lab frame, whereas $\{\hat{x}, \hat{y}, \hat{z}\}$ represents the reference frame of a single NV group. The $\hat{Z}$ axis in the lab frame is the loading axis in all cases. In each case, the local frame $\{\hat{x}, \hat{y}, \hat{z}\}$ of one of the NV groups is shown. (a) In a [100] cut anvil, the four NV groups are degenerate with respect to the loading axis. (b) In a [110] cut anvil, two sets of NV groups are each doubly degenerate with respect to the loading axis. One set is oriented in the plane of the culet, whereas another set projects strongly on the loading axis. (c) In a [111] cut culet, one NV group is fully oriented along the loading axis. Note that the local frame of this [**111**] **NV group** is coincident with the lab frame. The other three NV groups are degenerate with respect to the loading axis.
**Note:** The [100], [110] and [111] directions are represented in the crystal frame of diamond which is not shown in this figure.

## 2.4 Using high-pressure tools...

This chapter is a very short primer on high pressure techniques. I recommend Mikhail Eremets' book [36] on *High pressure experimental methods* for more thorough details on each technique. In the following chapters, we will see how we can combine diamond anvil cells and NV sensing to build a platform for high-pressure metrology.

# Chapter 3

# NV sensing at high pressure: proof of principle

The group's foray into high pressure had a meandering start. After a few attempts at studying the NV's response to pressure, we set out to measure the full stress tensor inside the culet. Other adventures were picked up along the way as we learned about efforts by Prof. Jean Francois Roche's group in this sphere. Coordinating with Prof. Roche in France and Prof. Sen Yang's group in Hong Kong, we decided to publish our first proof of concept study on NV sensing under pressure [49, 61, 107]. This chapter details that work.

Instead of reproducing our publication [49] in this thesis, I provide a high-level overview of the study. In particular, I highlight the key strengths of the NV center in high pressure metrology and how it can complement other conventional high pressure probes. My primary objective is to give a sense of this scientific tool's wide range of possibilities as a potential technology.

## 3.1 Stress Response of the NV center

Crystal stress (equivalently, strain) affects both the optical and spin properties of the NV center. Davies and Hammer [26] were the first to investigate the former in the late 1970s. They provided a thorough and careful calibration of the NV optical response to crystal stress up to $\sim 2\,\mathrm{GPa}$ even before the NV center was identified. The spin stress coupling parameters were first measured by Barson *et al.* [10], whose study provided a launchpad for our work.

This section summarizes the stress Hamiltonian in the NV reference frame. Just as in the case of magnetic fields, a generic crystal stress $\overset{\leftrightarrow}{\sigma}$ will project differently in the reference frame of the four NV groups. The full stress Hamiltonian is written as follows:

$$H_S = \sum_{i\in\{1,2,3,4\}} D\big(\overset{\leftrightarrow}{\sigma}^{(i)}\big)S_{z,i}^2 + E_x\big(\overset{\leftrightarrow}{\sigma}^{(i)}\big)(S_{x,i}^2 - S_{y,i}^2) + E_y\big(\overset{\leftrightarrow}{\sigma}^{(i)}\big)(S_{x,i}S_{y,i} + S_{x,i}S_{y,i}) \quad (3.1)$$

where $\overleftrightarrow{\sigma}^{(i)}$ is the local stress tensor, and $\{S_{x,i}, S_{y,i}, S_{z,i}\}$ are the spin-1 matrices for the $i$-th NV group. The stress parameters $D, E_x,$ and $E_y$ are as follows:

$$D = \alpha_1\big(\sigma_{xx}^{(i)} + \sigma_{yy}^{(i)}\big) + \beta_1\sigma_{zz}^{(i)} \tag{3.2}$$

$$E_x = \alpha_2\big(\sigma_{xx}^{(i)} - \sigma_{yy}^{(i)}\big) + \beta_2\big(2\sigma_{xz}^{(i)}\big) \tag{3.3}$$

$$E_y = \alpha_2\big(2\sigma_{xy}^{(i)}\big) + \beta_2\big(2\sigma_{yz}^{(i)}\big) \tag{3.4}$$

Here $\{\alpha_1, \beta_1, \alpha_2, \beta_2\} = (2\pi) \times \{8.6(2), -2.5(4), -1.95(9), -4.50(8)\}$ MHz/GPa are the stress susceptibilities. A full derivation of the this Hamiltonian based on Barson *et al.* is given in section 4.3.3 of the supplementary information of [49].

**Note:** Based on the above Hamiltonian crystal stress will induce a shift of $D$ and a splitting of $2E = 2\sqrt{E_x^2 + E_y^2}$ (Fig. 3.1).

## Stress and Symmetry

The connection between the stress and the $C_{3V}$ symmetry of the NV center can help build intuition about the stress Hamiltonian 3.1. For a single NV group, I rewrite the full Hamiltonian as follows:

$$H = \big(D_{gs} + D\big)S_z^2 + E_x(S_x^2 - S_y^2) + E_y(S_xS_y + S_yS_x) \tag{3.5}$$

where $D_{gs} = (2\pi) \times 2.87\,\text{GHz}$ is the zero-field splitting. In the frame of the NV group, the stress can either preserve the symmetry of the NV center (e.g., a combination of $\sigma_{zz}$ or $\sigma_\perp = (\sigma_{xx} + \sigma_{yy})/2$) or break the symmetry. In the former case, the stress should preserve the degeneracy of the $|S = 1, m_S = \pm 1\rangle$ spin states and cause the cwODMR resonance to shift. In the latter case, the stress should lift the degeneracy of the $|S = 1, m_S = \pm 1\rangle$ states causing the cwODMR resonance to split.

Under a symmetry breaking stress, the 'good' eigenstates should be an admixture of $|m_S = \pm 1\rangle$ states. Within the $|m_S = \pm 1\rangle$ manifold, the reduced Hamiltonian can be written as

$$H = (D_{gs} + D)\mathbb{I} + E_x\,\boldsymbol{\sigma_x} + E_y\,\boldsymbol{\sigma_y} \tag{3.6}$$

where $\mathbb{I}$ is the identity and $\boldsymbol{\sigma_x}, \boldsymbol{\sigma_y}$ are the Pauli matrices. $E_x$ and $E_y$ are given by equations 3.3 and 3.4.

It follows that symmetry breaking stress $E_x$ (and $E_y$) mixes the $|m_S = \pm 1\rangle$ states into symmetric and anti-symmetric combinations $|\pm x\rangle = (|+1\rangle \pm -1)/\sqrt{2}$ (and similarly $|\pm y\rangle$). To distinguish between $E_x$ and $E_y$ stress parameters, one must study the relative contrast of the resonance peaks as a function of the direction of a linearly polarized MW drive. An application of this technique in the context of electric field sensing [75] is discussed in chapter 4. Fig. 3.1 describes the effect of stress on the spectrum at an intuitive level.

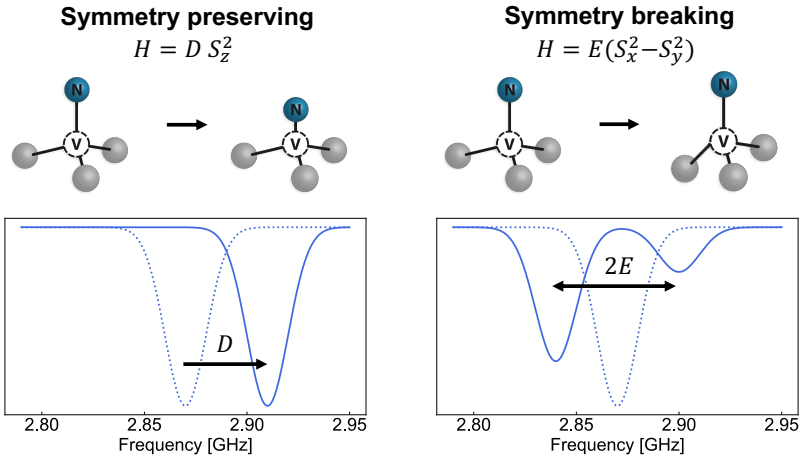


Figure 3.1: **Stress coupling of the NV center:** A symmetry preserving stress (left) shown as a compression along the N-V axis shifts the NV resonance line. In contrast, a symmetry breaking stress (right) shown as a bending of a carbon dangling bond lifts the degeneracy of the $|m_S = \pm 1\rangle$ states and splits the NV resonance line. In addition, the admixture of the $|m_S = \pm 1\rangle$ states under a symmetry breaking stress can have different transition matrix elements with the $|m_S = 0\rangle$ state under linearly polarized microwave radiation.

## 3.2 Early promise

Having covered various aspects of NV centers and diamond anvil cells, we are finally ready to embark on our first study of NV sensing under pressure. In this section, I will first show how NV imaging can be used to study a structural phase transition in Iron (Fe) by measuring the associated change in magnetism. Next, by tuning temperature, we will explore the pressure-temperature phase diagram of Gadolinium (Gd). Finally, I will detail our measurements of the full stress tensor as a probe of the glass transition and departure from quasi-hydrostaticity in a pressure medium.

In all studies, we used 200 µm flat culets and a Pasternak DAC. Type Ib diamond anvils of different crystal cuts were incorporated with a layer of NV ensembles up to 50 nm below the surface. In studying magnetism in Iron and measurements of the full stress tensor, we used Rhenium (Rh) gaskets and a 16 : 3 : 1 by volume mixture of methanol, ethanol, and water as a pressure medium. For the Gd study, we used Beryllium-Copper (BeCu) gaskets and Caesium Iodide (CsI) as a pressure medium. Microwave radiation was applied using Pt wire placed close to the culet surface. In all experiments, we used confocal microscopy with sub-micron spatial resolution. We mapped out the magnetic and stress fields by rastering the excitation beam over the culet surface. All measurements under pressure were continuous wave ODMR.

**Note:** Figures in the following sections appear in our publication [49]. However, I have

attempted to rephrase the text and figure captions to provide a more concise description of the work. In case of any inconsistencies or inadequacies in my description, I defer to the published work.
**Note:** While the data collection on $\alpha \leftrightarrow \epsilon$ transition in Iron and stress sensing was largely spearheaded by Satcher Hsieh, I was most actively involved with the work on Gadolinium.

## Sensing $\alpha \leftrightarrow \epsilon$ transition in Iron

Under ambient conditions elemental Iron (Fe) exists in the body-centered cubic (bcc) crystal structure. This form, commonly referred to as $\alpha$-Iron, is a soft ferromagnet [27]. Under pressure, it is well established that Iron undergoes a structural phase transition into a hexagonal close-packed (hcp) crystal structure [5]. Concomitant with this transition into so-called $\epsilon$-Iron, there is a drastic reduction in the magnetic moment.

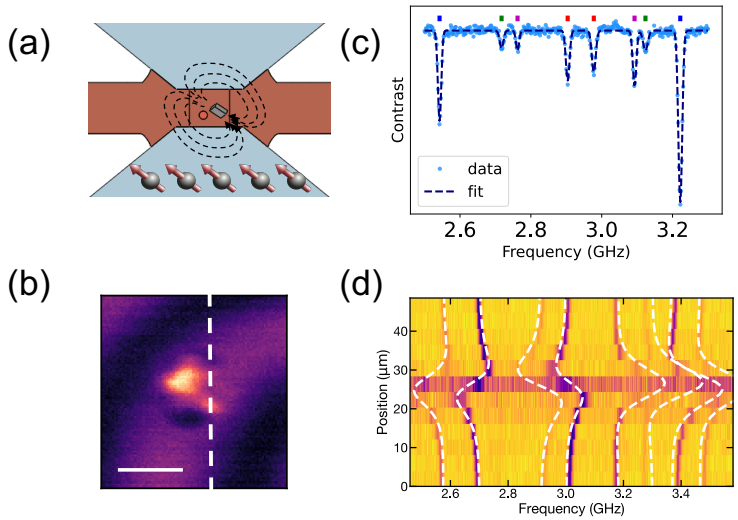


Figure 3.2: **Imaging local magnetic fields under high pressure [49]:** (a) A schematic of the loading showing a ruby pressure marker, the iron pellet, and a layer of NV centers 50 nm below the culet surface. In the presence of an applied external field $H_{ext} \sim 180$ G, the magnetic domains of $\alpha$-Iron roughly align to the field to yield a dipole field pattern (shown in broken black arrows). (b) A white light microscope image of the Iron pellet (scale bar on the bottom left shows 10 μm). (c) At each point of this image, we can take a cwODMR spectrum to determine the local magnetic field. The projection of the local field in the frame of the four NV groups determines the magnitude of the splitting and shifting of their resonances. **Note:** The spectrum shown is a sample cwODMR resonance and is not belong to this data set. (d) By taking a line cut along the vertical (white broken line in (b)) we can follow the change in the NV resonances with position to make a map of the local field.

In this experiment, we employed NV magnetometry to image the local magnetic field of a $\sim 10\,\mu m$ iron pellet (sourced commercially from Alfa Aesar) on both compression and decompression up to $\sim 20\,GPa$ (Fig. 3.2). We used confocal microscopy to make a two-dimensional map of the dipole field from the iron sample (Fig. 3.3).

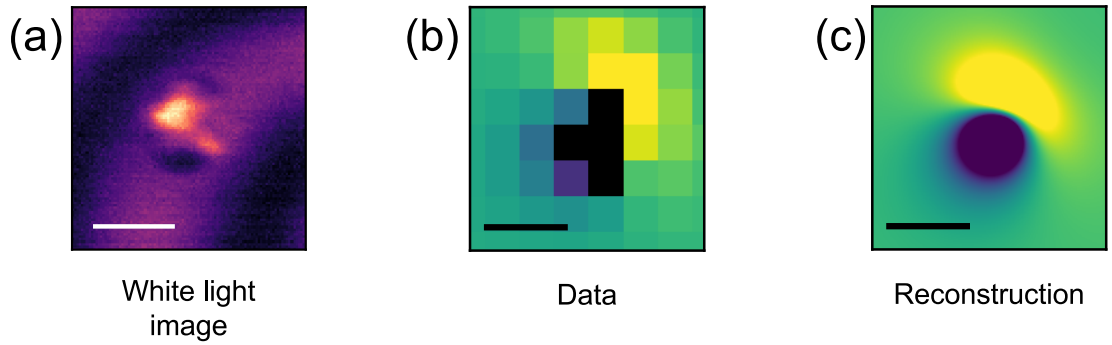


Figure 3.3: **Reconstructing the dipole field of Iron [49]:** Following the procedure in Fig. 3.2 (d), we can map out the NV resonances over the sample region (a). (b) Fitting to the local magnetic field, we directly see a dipole field pattern around the location of the pellet. Directly on top of the Iron pellet (black pixels), cwODMR resonances are obscured due to large field gradients. (c) Nevertheless, the obtained field pattern can be fit to a point dipole model to fully reconstruct the field over the sample region (see section 5.2 of supplementary information in [49] for full details).

Monitoring the changes in the dipole strength of the sample, we directly observe a first-order structural phase transition between $\alpha \leftrightarrow \epsilon$ Iron on both compression and decompression (Fig. 3.4). The transition occurs at $P = 16.7 \pm 0.7\,GPa$ on compression and at $P = 10.5 \pm 0.7\,GPa$ on decompression (Fig. 3.4 (c)). The observed hysteresis in the transition profile is a combination of the intrinsic hysteresis associated with the first-order structural phase transition and the broadening of onset and completion due to stress gradients in the pressure medium. We determine a critical pressure $P_C = 13.6 \pm 3.6\,GPa$ which is in good agreement with previous work measuring $P_C \approx 12\,GPa$ using Mossbauer spectroscopy [99].

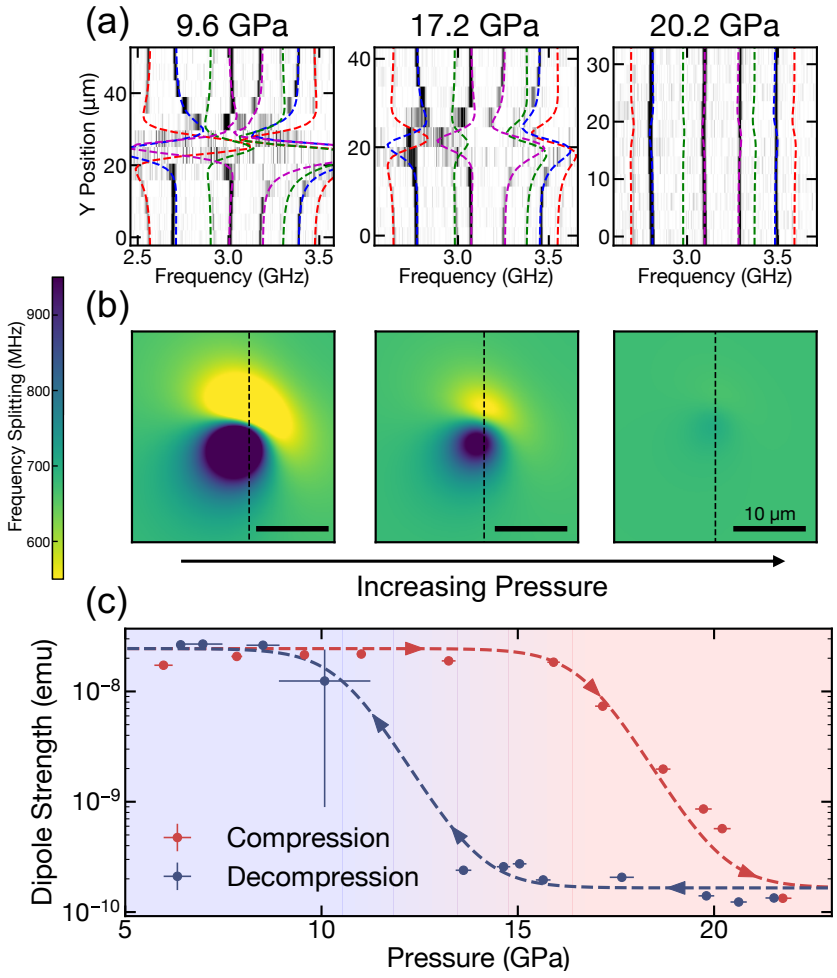


Figure 3.4: **Structural transition between $\alpha \leftrightarrow \epsilon$ Iron [49]:** Mapping out the dipole pattern at each pressure point on both compression and decompression we can quantitatively ascertain the dipole strength of the Iron sample under pressure. (a) cwODMR data taken along a line cut in the sample area (black broken line in (b)) at three demonstrative pressure points on compression. The spatial variation of the local magnetic field diminishes on compression from 9.6 GPa to 17.2 GPa and effectively disappears at 20.2 GPa. (b) Extracted dipole maps show a marked reduction in dipole field strength with increasing pressure. (c) A plot of the dipole strength against applied pressure (measured using ruby fluorescence) shows a clear transition from $\alpha \rightarrow \epsilon$ with the onset at $\sim 15$ GPa and completion at $\sim 22$ GPa. On decompression, the transition from $\epsilon \rightarrow \alpha$ iron shows and onset at $\sim 15$ GPa and completion at $\sim 9$ GPa. The pressure gradients in the sample chamber exacerbate the intrinsic hysteresis associated with this first-order structural transition. **Note:** The large error bar associated with the decompression pressure point at 11 GPa is due to relaxation in the sample chamber during data acquisition. A drift pressure in the chamber resulted in a significant change in the sample dipole moment.

## $PT$ Phase diagram of Gadolinium

Tuning a combination of pressure and temperature as thermodynamic parameters can give rise to a diverse system of phases. Our goal here was to demonstrate the robustness of the NV center as a high pressure sensor operating between room temperature ($\approx 300\,\mathrm{K}$) and cryogenic temperatures ($\approx 25\,\mathrm{K}$). Specifically, in addition to pressure-driven structural transitions, we can use NV sensing to study temperature-driven transitions in magnetic ordering. Gadolinium (Gd) was a clear choice due to its Curie transition near room temperature [84]. Unwittingly, however, we chose a material with a rich $PT$ phase diagram bejeweled with structural and magnetic phases [87]. Under ambient pressures, Gd exists in a hexagonal close-packed (hcp) crystal structure. hcp-Gd shows a Curie transition from paramagnetic (PM) to ferromagnetic (FM) state on cooling below $\sim 294\,\mathrm{K}$ [66]. Itinerant electrons mediate an RKKY-type interaction between the localized $4f$ electrons in Gd. The ordering of these $4f$ electrons in turn induces ordering in the itinerant electrons [80] making it an interesting material for studies of magnetism. Magnetic properties of Gd and other rare earth elements in their many structural phases continue to be of research interest today [87, 55, 80].

In this study, we loaded a $\sim 30\,\mu\mathrm{m}$ piece of Gd cut out from commercially bought Gd foil (Alfa Aesar). Using an Attocube attoDry800 cryostat for temperature control we cooled the sample in the presence of a background magnetic field of $\approx 100\,\mathrm{G}$. To measure the sample's local magnetic field, we probed the NV cwODMR spectrum at a spatial point close to it. A separate spatial point more than $50\,\mu\mathrm{m}$ away from the sample was used as a control to monitor for changes in the background field.

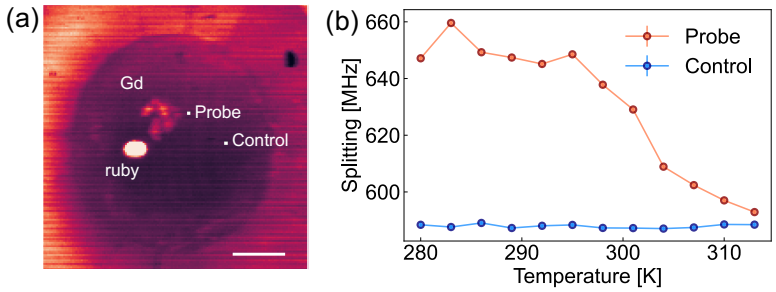


Figure 3.5: **Gadolinium (Gd) loading [49]:** (a) Fluorescence scan showing a Gd sample and ruby pressure marker. cwODMR from culet NVs were taken at a 'probe' point close to the Gd sample. A 'control' point further away from the sample was used to monitor changes in the applied background magnetic field. White scale bar shows $50\,\mu\mathrm{m}$. (b) On cooling below the Curie temperature with an applied background field, we notice a dramatic increase in the splitting at the probe point suggesting a contribution to the local magnetic field from the ferromagnetic ordering in hcp-Gd. In contrast, we observe no change at the control point.

On cooling the sample, we observe a dramatic increase in the NV splitting at the probe point relative to the control point (Fig. 3.5 (a)) suggesting a local change in the magnetic field due to ferromagnetic ordering in hcp-Gd. The observed Curie transition temperature $Tc = 292.2 \pm 0.1\,\mathrm{K}$ decreases at the rate $dT_c/dP = -18.7 \pm 0.2\,\mathrm{K/GPa}$ consistent with previous studies [55]. Furthermore, there is no hysteresis in the transition profile, per the nature of this second order transition. Surprisingly we observe PM $\leftrightarrow$ FM transition in hcp-Gd up to a pressure of $\sim 6\,\mathrm{GPa}$, well beyond the phase boundary (at 2 GPa) between hcp and Samarium type (Sm-type) crystal structure. This observation suggests that the dynamics of the hcp $\rightarrow$ Sm-type transformation is slow to equilibrate during data acquisition.

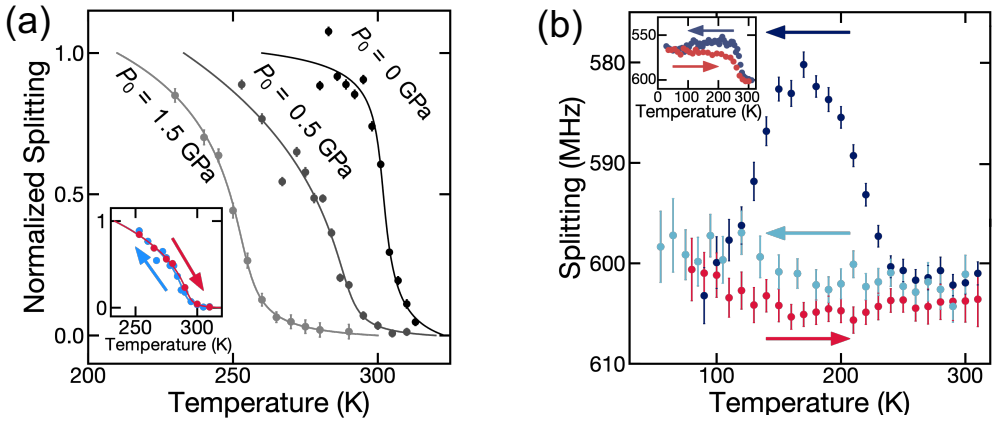


Figure 3.6: **Probing structural and magnetic transitions in Gd [49]:** (a) Profile of the Curie transition in hcp-Gd shows a decreasing transition temperature with an increase in pressure. Inset shows no perceptible hysteresis associated with this transition at 0.5 GPa consistent with its second order nature. (b) A path in the $PT$ phase diagram (dark blue) starting in the hcp structural phase at near $\sim 2\,\mathrm{GPa}$ shows a clear increase in splitting at the Curie transition point. However, increasing pressure on further cooling results in an abrupt loss of ferromagnetic signal at $\gtrsim 6\,\mathrm{GPa}$ suggesting a structural transition into the dhcp phase. Retracing the $PT$ path after this change in crystal structure into the dhcp phase (red and light blue) shows no recovery of the ferromagnetic signal underpinning the metastability of the dhcp phase on quenching pressure. However, the signal associated with magnetic ordering in the hcp phase is recovered if the dhcp phase boundary at $\sim 6\,\mathrm{GPa}$ is not crossed (inset).

Due to the contraction of the cell body on cooling, each cooldown for this study traces a non-isobaric path in $P - T$ space cutting across a mix of magnetic and structural phase boundaries. Compared to the relatively simple characterization of the Curie transition in hcp-Gd, exploring the full phase map of Gd is a far more involved task. For one specific cooldown, we observed the characteristic magnetic ordering of hcp-Gd. Further cooling re-

sulted in pressure increasing above $\sim 6$ GPa, the phase boundary between Sm-type structure and double hexagonal close-packed (dhcp) crystal structure in Gd. Concurrent with this increase in pressure at 130 K we observed a sharp decrease in ferromagnetic signal suggesting a crossover into the paramagnetic phase of dhcp-Gd. Quenching the pressure did not result in recovery of the ferromagnetic signal even on several rounds of temperature cycling suggesting that the dhcp phase is metastable at lower pressures.

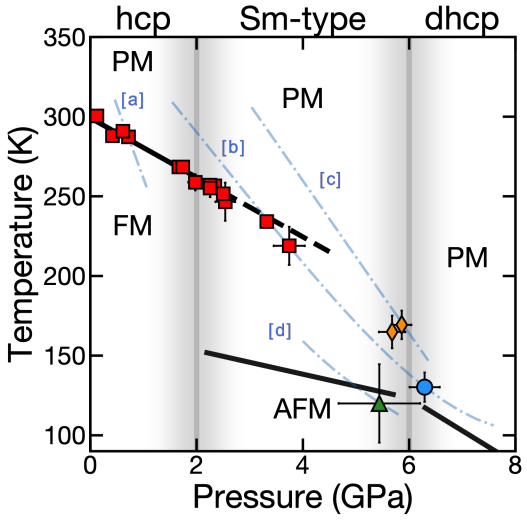


Figure 3.7: *PT* **phase diagram of Gadolinium [49]:** Each cooldown takes a diagonal path through the *PT* phase space. [a] The curie transition in hcp-Gd (red squares) is observed well beyond the boundary of the hcp and Sm-type structural phases suggesting sluggish transition dynamics between these two crystal structures. [b] Starting in the paramagnetic hcp phase, we observe a Curie transition followed by a complete loss of magnetic signal at the boundary of the dhcp crystal phase (detailed in Fig. 3.6 (b)). Significantly weaker signals are obtained in the transition from the paramagnetic Sm-type to paramagnetic dhcp-Gd (orange diamonds in [c]) and the Neel transition within the Sm-type phase (green triangle in [d]). The magnetic phase boundaries within the Sm-type and dhcp structural phases are taken from [87].

Additional transitions from PM (Sm-type) $\leftrightarrow$ PM (dhcp) phases and PM $\leftrightarrow$ AFM (antiferromagnetic) ordering within Sm-type phase show markedly weaker signals (See section 6 of supplementary information of [49]) because of the small change in the sample's magnetic susceptibility across these transitions. Nevertheless, future work using AC magnetometry under pressure remains a viable means of diagnosing such transitions with high sensitivity and spatial resolution [18].

## Stress sensing

In the final study, we demonstrate the versatility of NV sensing. Departing from DC magnetometry, we used cwODMR measurements to extract the full stress tensor at the culet of the diamond anvil up to pressures of $\sim 13$ GPa. Pressure calibration is a central problem in high pressure physics. Furthermore, measuring stress tensor is crucial for decoupling the effects of hydrostatic and deviatoric stresses in high pressure systems [11]. To this end, the ability to image the full stress tensor in tabletop experiments with sub-micron spatial resolution is a promising application of NV sensing in many high pressure studies.

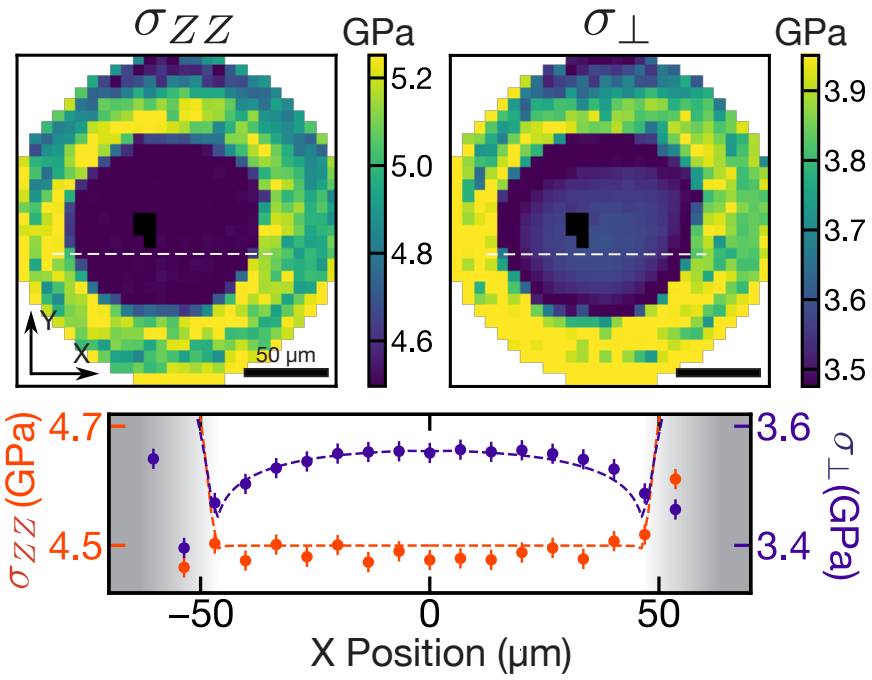


Figure 3.8: **Imaging Culet stress [49]:** Maps of the uniaxial $\sigma_{ZZ}$ stress (left) and the biaxial $\sigma_\perp = (\sigma_{XX} + \sigma_{YY})/2$ (right) in a [111] cut culet. The outer region shows stress at the gasket and the inner region shows stress within the sample chamber when using 16:3:1 methanol/ethanol/water pressure medium. The ruby pressure of 4.9 GPa agrees closely with the $\sigma_{ZZ}$ stress value in the sample chamber. A linecut of the stress (along the white broken line in the culet) is shown at the bottom. The $\sigma_{ZZ}$ and $\sigma_\perp$ stress profiles are qualitatively different. We observed a uniform stress profile in the former case due to a quasihydrostatic pressure medium. In the latter case, we observe a convex spatial profile due to the 'cupping' of the diamond culet. In both cases, finite element simulations (broken lines) fit the measured stress.

Crystal stress ($\overleftrightarrow{\sigma}$), being a symmetric tensor, has six free parameters. As outlined earlier

in Eq. 3.1, a generic crystal stress projects differently in the frame of each NV group giving eight measurements (shift and splitting for four groups). Like vector magnetometry, solving for the stress tensor is an over-constrained problem. In this experiment, we applied a carefully controlled magnetic field transverse to the NV axis of a particular NV group. For the other three NV groups, the field projection along their respective NV axes induces a large Zeeman splitting, spectroscopically isolating the target group. For this target NV group, the field couples in second order, allowing us to directly measure the shift and splitting due to stress. Repeating this procedure for all NV groups gives us the required shifts and splittings due to stress.

To demonstrate the potential scope of stress imaging, we used this technique to qualitatively probe the glass transition in our pressure medium: a mixture of methanol, ethanol, and water in the ratio of 16:3:1 by volume. This medium is quasi-hydrostatic only up to $\sim$ 10 GPa pressures. Imaging at $\approx$ 4.9 GPa, we measure a unifrom $\sigma_{ZZ}$ stress across the sample chamber region. However, at $\approx$ 13.6 GPa pressure, there is a distinct spatial gradient in the $\sigma_{ZZ}$ stress suggesting that the sample can support deviatoric stresses in the 'glassy' phase [42].

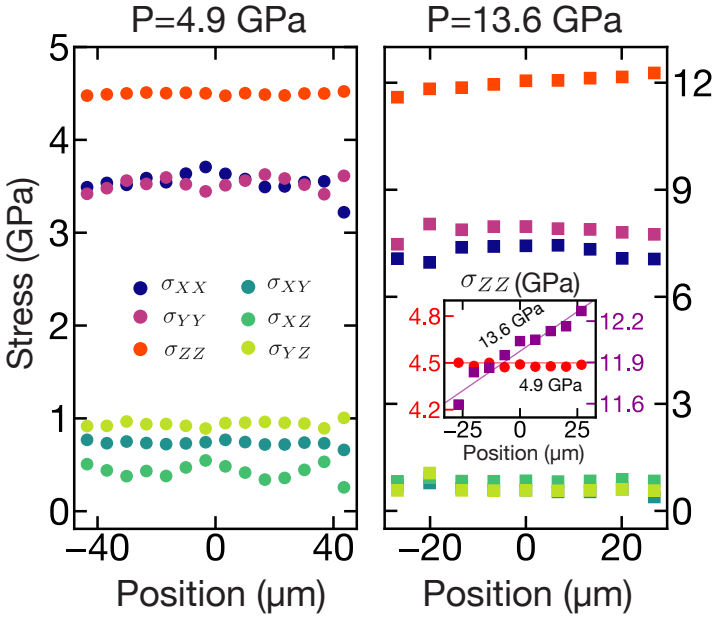


Figure 3.9: **Glass transition in Methanol/Ethanol/Water [49]:** A comparison of all six stress components is plotted along a linecut in the sample chamber region for two pressure points (denoted by the ruby pressures of 4.9 GPa and 13.6 GPa). The right inset shows a comparison of the $\sigma_{ZZ}$ stress below and above the glass transition of the pressure medium. We see a clear development of a spatial pressure gradient at 13.6 GPa.

## 3.3 Other Techniques

I want to briefly highlight a complementary approach concurrently undertaken by Yip *et al.* [107] in their high pressure sensing project. Specifically, instead of implanting NV centers in the diamond anvil, Prof. Sen Yang's group used Moissanite anvils to apply pressure. Their work demonstrates the compatibility of NV sensing with a wide range of high pressure tools. By incorporating micron size diamond particles directly in the sample chamber, the group was able to demonstrate magnetic sensing of the superconducting transition in $BaFe_2(As_{0.59}P_{0.41})_2$ (Fig. 3.10). Similar to the studies highlighted in this chapter, this technique allows one to perform *in situ* calibration of hydrostatic pressure as well as spatially resolved magnetometry. As we will discuss, the loss of contrast under hydrostatic pressures limits the viable application of this method for sensing at megabar pressures [28]. Nevertheless, when used in conjunction with Moissanite anvils at low pressures, the use of readily available NV microdiamonds (through Adamas Nanotechnologies) can be a cost-effective solution. I encourage interested readers to peruse their beautiful work!

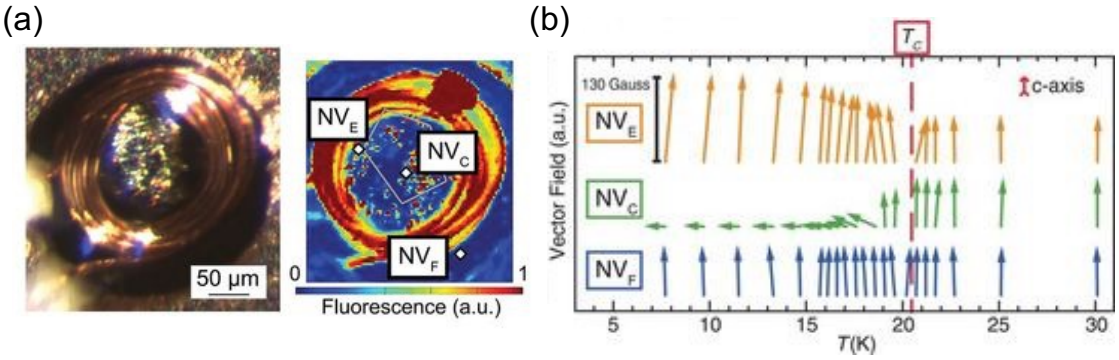


Figure 3.10: **Sensing superconductivity using diamonds particles in high pressure chamber (figure reproduced from Yip *et al.* [107]):** (a) A comparison of white light (left) and fluorescence (right) images showing MW driving coil and diamond particles in the sample chamber of the pressure loading. Scattered diamond particles can serve both pressure calibration and spatially resolved magnetic sensing. (b) Warming up across a superconducting transition with an applied magnetic field, the authors perform vector magnetometry at three points to show local changes due to Meissner expulsion of the applied field from the interior of the superconducting sample. Above the superconducting transition ($T_C$), all three locations measure the same applied field.

## 3.4 Looking forward

The work described in this chapter was the first step in taking the project of NV sensing under pressure from ideation to actuality. In the first two studies of magnetism in Iron and Gadolinium, we probed magnetic and structural transitions. The crucial ability to perform spatially resolved measurements allowed us to monitor local changes in the magnetic field induced by the sample while controlling for global parameters such as the applied background field. In this context, the ability to perform local measurements *insitu* with diffraction-limited sub-micron spatial resolution is a crucial advantage of NV sensing. In the final study, we demonstrate the versatility of NV sensing by directly measuring the stress at the diamond culet. Here, measuring the full stress tensor (in particular the shear stress) can enable us to ask a wealth of questions on several fronts. First, by spatially mapping the changes in stress for different anvil geometries, we can optimize anvil design to the requirements of the experiment. Second, we can better understand deviations from hydrostaticity in different pressure media. Third, by independently measuring the stress components, we can better parse apart the effects of specific stress parameters on sample behavior.

As a thermodynamic parameter, pressure (hydrostatic stress) provides a powerful tool for mining out novel phases. NV sensing affords one a suite of capabilities including spatially resolved AC and DC magnetometry and electrometry, in addition to stress mapping and calibration. While it is great to see the usefulness of NV sensing realized in this context, it is even more exciting to think about how it can work synergistically with other high pressure probes (such as transport and X-ray diffraction) to empower us to ask an array of new scientific questions. The following chapters describe our initial efforts on this front.

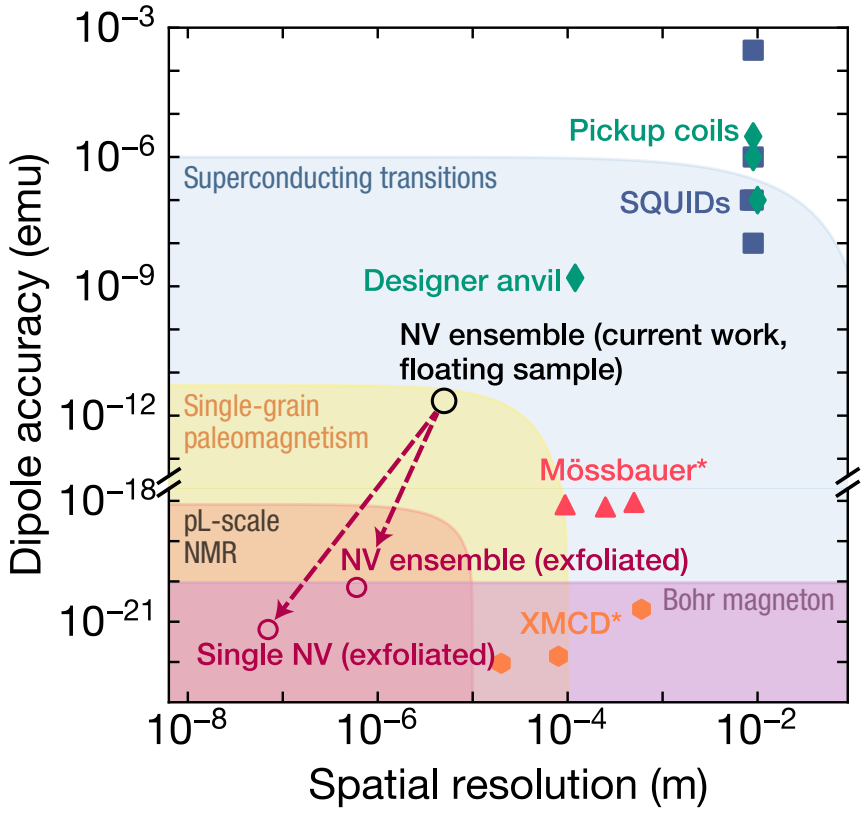


Figure 3.11: **A survey of magnetic sensing at high pressure [49]:** spatial resolution is defined as the length scale over which the sensor can probe variations in magnetism. For the case of the superconducting quantum interference device (SQUID) and pick-up coils, the spatial resolution is the size of the coil over which the entire signal is integrated. The performance of this work and projected sensitivity for future work shows the ability of NV centers to outperform several conventional high pressure probes of magnetism.

# Chapter 4

# The NV center at ambient conditions: strain and electric fields

In this chapter, I will break from the larger theme of the thesis to briefly touch upon an important *non-example* of strain (equivalently, stress) in NV centers. Although I will closely follow our published work [75], I do not intend to reproduce the paper. Instead, I want to highlight some aspects of the work and touch on topics pertinent to the context of NV sensing under pressure.

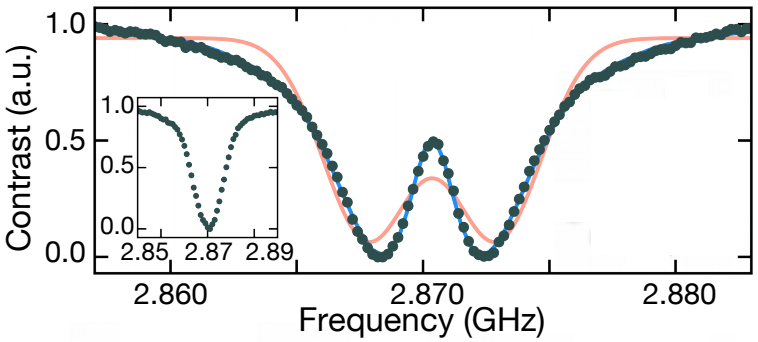


Figure 4.1: **Zero field cwODMR spectra in type Ib diamond [75]:** cwODMR spectra of NV centers in type Ib diamond show a clear splitting with features that do not fit to Gaussian or Lorentzian lineshapes. In particular, the inner slope at the splitting is sharper than expected based on inhomogeneous broadening. In addition, we observe consistent heavy tails away from the center. The inset shows a naive expectation based on zero field splitting term ($H_0 = D_{gs}S_z^2$, where $D_{gs} = (2\pi) \times 2.87\,\text{GHz}$) and inhomogeneous broadening coming from magnetic noise.

In the lab's early days, as we were testing the waters, the group set out to study several

different kinds of diamond samples with NV centers. Linewidth and contrast properties of bulk diamonds, nanodiamonds, and microdiamonds of all shapes and sizes were painstakingly characterized. We were all operating under the idealized picture that under ambient conditions, the NV Hamiltonian is $H = D_{gs}S_z^2$ with $D_{gs} = (2\pi) \times 2.87\,\text{GHz}$. However, our data showed something completely different. Rather than a single resonance, the spectrum showed an apparent splitting of $\sim 10\,\text{MHz}$ in high-density samples with lineshapes that were not characteristically Gaussian or Lorentzian (Fig. 4.1). In the case of nanodiamonds and microdiamonds, it was understandable that surface effects (likely strain) may lead to such features. However, what could be the source of strain in bulk crystals? Furthermore, these cwODMR features were qualitatively different in bulk Type Ib and Type IIa diamond samples. Knowing that the density of defects (substitutional nitrogen centers) is the primary difference between the two diamond materials, it felt uneasy to think that strain could cause such a difference. On a seemingly unrelated note, we knew that we are always working with the negatively charged $NV^-$ center. Where did the additional electron come from?

Our effort to make sense of these questions is the subject of this chapter. For complete details on this work (done jointly with several other group members), I encourage the reader to look at the paper [75] and the supplementary information.

**Note:** In the larger context of the thesis, it is helpful to think of high pressure experiments as exerting global stress on diamond samples. However, in the case of this work, we consider local (intrinsic) strain in NV ensembles. While stress and strain may be equivalent, I will consider the latter in this chapter.

## 4.1 NV spectra at $B = 0$

In the absence of environmental parameters such as strain, electric, and magnetic fields, the spin 1 ground state of the NV center is modeled to have a zero field splitting ($D_{gs} \sim (2\pi) \times 2.87\,\text{GHz}$) due to dipole-dipole interaction between the valence electrons [29]. In addition, a hyperfine interaction stems from the spin 1 $^{14}$N nucleus of the NV defect. This interaction term given by $H_{hyp} = A_{zz}S_zI_z$ where $A_{zz} = (2\pi) \times 2.16\,\text{MHz}$ and $I = 1$ [94]. In the absence of any near shell $^{13}$C nuclei (with a natural abundance of $\sim 1.1\%$), we, therefore, expect three resonance lines spaced apart by the interaction strength $A_{zz}$ with the center line at $\nu \sim (2\pi) \times 2.87\,\text{GHz}$.

We observe several qualitatively different features by studying samples with defect concentrations spanning more than two orders of magnitude (type Ib diamond with $\sim$ ppm level concentrations and type IIa samples with $\sim$ ppb level concentrations) in the cwODMR spectrum. For high density type Ib samples, we observe three crucial features in the spectrum (Fig. 4.1):

- resonance lines with an asymmetric lineshape that is neither Gaussian nor Lorentzian
- the central feature of the resonance is sharper than the inhomogeneous linewidth (stemming from magnetic noise of electron spins associated with defects such as substitu-

tional nitrogen centers)

- the presence of two resonances with a strong splitting $\sim 5 - 10\,\mathrm{MHz}$ without any significant shift

Interestingly, in the case of type IIa diamonds with far lower defect concentrations, cwODMR spectra at zero fields is closer to the expectations resembling the three lines resulting from hyperfine interaction with $^{14}N$ (Fig. 4.3 (c)). However, the central resonance consistently shows an apparent splitting ($< 1\,\mathrm{MHz}$) without any marked shift. The qualitative features in the spectra of high density samples (listed above) persist for this central resonance in these spectra.

Such spectra are typically attributed to local strain (equivalently, stress) in diamond samples [30, 51, 10, 37, 111, 91, 1, 59, 60, 17, 86, 53, 72, 20, 62, 96]. However, at a high level, it is not clear if there is a strong connection between defect concentration and local stress so as to yield qualitatively different spectra in the two cases described above. More importantly, in the case of ensemble spectra (as above), an averaging of the local strain should result in shifting and splitting in comparable magnitude owing to the values of the strain susceptibility parameters [10]. Consequently, one should observe an overall broadening of ensemble cwODMR spectra instead of a splitting (Fig. 4.2).

## 4.2 Intrinsic electric fields in bulk diamonds

Strain and electric field couple in similar ways to the ground state spin of the NV center. In particular, the full Hamiltonian of the NV center in the presence of electric fields (projected in the NV frame) is given by:

$$H = \underbrace{D_{gs}\, S_z^2}_{H_0} + \underbrace{A_{zz}\, S_z\, I_z}_{H_{hyp}} + \underbrace{\Pi_z\, S_z^2 + \Pi_x(S_x^2 - S_y^2) + \Pi_y(S_x S_y + S_y S_x)}_{H_E} \tag{4.1}$$

Here, $D_g s = (2\pi)\times 2.87\,\mathrm{GHz}$ is the zero field splitting, $A_{zz} = (2\pi)\times 2.16\,\mathrm{MHz}$ is the hyperfine coupling to the $^{14}$N nucleus and $\Pi_z = d_\parallel E_z$ and $\Pi_{\{x,y\}} = d_\perp E_{\{x,y\}}$ defines the coupling of the NV center to electric fields. $S$ ($I$) are spin 1 operators of the NV center ($^{14}$N nucleus). The electric field susceptibilities are given by $\{d_\parallel, d_\perp\} = \{0.35, 17\}$Hzcm/V [79].

In the electric field Hamiltonian ($H_E$) given above, $\Pi_z$ represents the symmetry preserving electric field term (coupling to $E_z$), which yields a shift in the NV spectrum. In contrast, $\Pi_{\{x,y\}}$ (coupling to transverse fields $E_{\{x,y\}}$) break the $C_{3V}$ symmetry of the defect and lead to a splitting. The stress Hamiltonian of the NV center (Eq. 3.1) has the same operators as $H_E$. However, while the stress susceptibility for the symmetry preserving and symmetry breaking terms of the NV center are of the same order ($\sim 10\,\mathrm{MHz/GPa}$), the susceptibility to transverse electric fields ($d_\perp$) is fifty times larger than susceptibility to symmetry preserving axial fields. In effect, ensemble spectra averaging over either electric or strain fields are more likely to yield a splitting without any significant shifting in the former case. In the latter

case, due to the absence of global stress in bulk diamonds, averaging over random intrinsic strain is more likely to result in an overall broadening in cwODMR spectra.

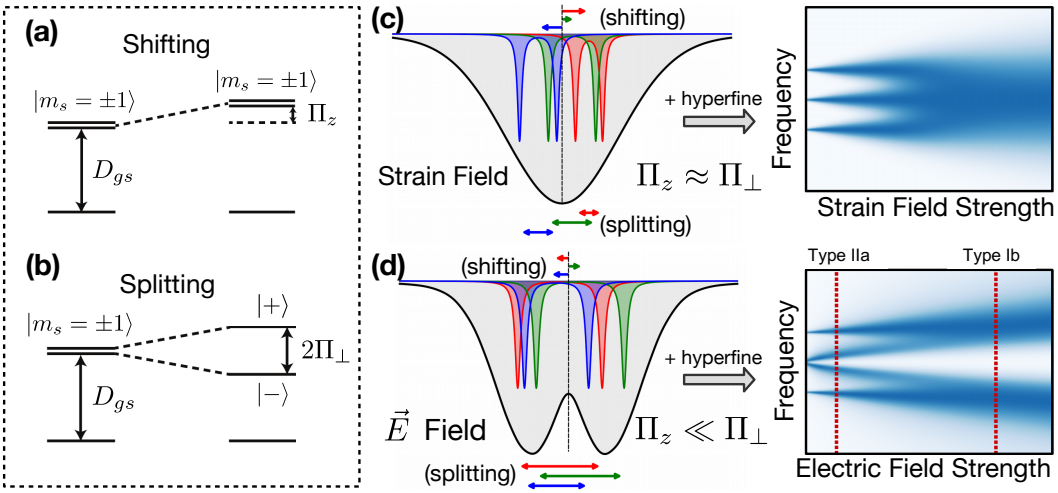


Figure 4.2: **A comparison of random electric fields and strain in ensemble NV spectra [75]:** Strain and electric field couple in similar fashion to the ground state spin of the NV center. (a) A symmetry conserving term $\Pi_z$ causes the $|m_S = \pm 1\rangle$ manifold to shift. (b) In contrast, a symmetry breaking term $\Pi_\perp$ leads to a splitting and mixing of the $|m_S = \pm 1\rangle$ states. (c) Due to comparable susceptibility parameters, a random strain is likely to both shift and split the NV spectra by the same order. In the presence of random local strain, the spectra of NV ensembles should consequently show an overall broadening (at large strain values). (d) In contrast, the splitting due to a transverse field is about fifty times larger than that due to an axial field of the same strength. Consequently, at large field strengths, ensemble averaging of random electric fields is more likely to yield a splitting in cwODMR spectra. A simulation on the right shows the evolution of the NV cwODMR spectrum with the strength of a random local vector electric field. Based on this evolution, one can earmark typical field strengths for Type Ib and Type IIa samples. A microscopic charge model based on this qualitative picture can allow us to extract the density of charged defects in different samples (see [75] for full details).
**Note:** This figure (taken from [75]) has been doctored for illustrative purposes only.

Furthermore, from the standpoint of electric fields, it is conceivable that defect concentrations affect cwODMR spectra. In particular, in high density samples (type Ib), the presence of a large number of charge defects (particularly under laser excitation in the case of cwODMR) suggests that larger electric fields can dominate the hyperfine coupling term. In contrast, for low density samples (type IIa), the hyperfine term in the Hamiltonian dictates the NV eigenstates. In the case of extremal hyperfine resonances corresponding to $|m_I = \pm 1\rangle$, this coupling manifests as a magnetic field $\pm A_{zz}/\gamma$ at the NV spin making. The

splitting of the NV spin due to this effective magnetic field adds in quadrature with the electric field splitting $\sim \sqrt{(A_{zz})^2 + (2\Pi_\perp)^2}$ (where $\Pi_\perp = \sqrt{\Pi_x^2 + \Pi_y^2}$). However, in the case of $|m_I = 0\rangle$, there is no such effect magnetic field projected onto the NV spin. Therefore, the center resonance splits linearly with the transverse electric field yielding the characteristic Type IIa spectra. A microscopic charge model using this qualitative picture to extract quantitative estimates for charge density is discussed in detail in [75].

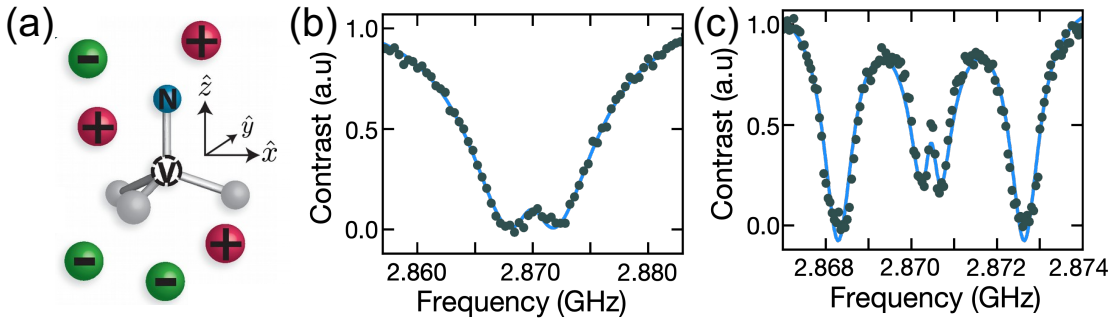


Figure 4.3: **Typical spectra of ensemble NV centers due to local electric fields [75]:** (a) An illustration of the microscopic charge model wherein NV centers are surrounded by charge defects yielding an effective electric field. The ensemble averaging of random fields (due to different local charge environments of each NV center) results in the spectra in (b-c). (b) In a high density (type Ib) sample, a higher concentration of charge defects causes the $H_E$ term in the NV Hamiltonian to dominate the hyperfine coupling with the $^{14}$N spin. (c) In a low density (type IIa) sample, a lower concentration of charge defects results in qualitatively different spectra resembling the expectations from the hyperfine coupling with the $^{14}$N nucleus. The extremal resonances for $|m_I = \pm 1\rangle$ (where I represent the nuclear spin) split quadratically with the strength of the electric field. However, for $|m_I = 0\rangle$, the NV spin evolves linearly with the electric field strength showing a clear splitting.

## 4.3 Vector imaging electric fields in single NV centers

Based on the above picture, it should be possible to identify the local charge environment of single NV centers. For single NV centers with stronger local electric fields, the cwODMR spectrum may show two resonances. In contrast, for NV centers with a markedly weaker local electric field, the spectrum is similar to that of type IIa ensembles. Crucially, however, in this case, we expect the electric field to have a definite direction and magnitude, allowing for full vector electrometry. In particular, the eigenstate of the NV spin in the presence of

an electric field (assuming $|m_I = 0\rangle$) is given by:

$$|\pm\rangle = \frac{1}{\sqrt{2}}(|m_S = +1\rangle \pm e^{i\phi_E} |m_S = -1\rangle) \tag{4.2}$$

where, $\phi_E = \arctan(\Pi_y/\Pi_x)$.

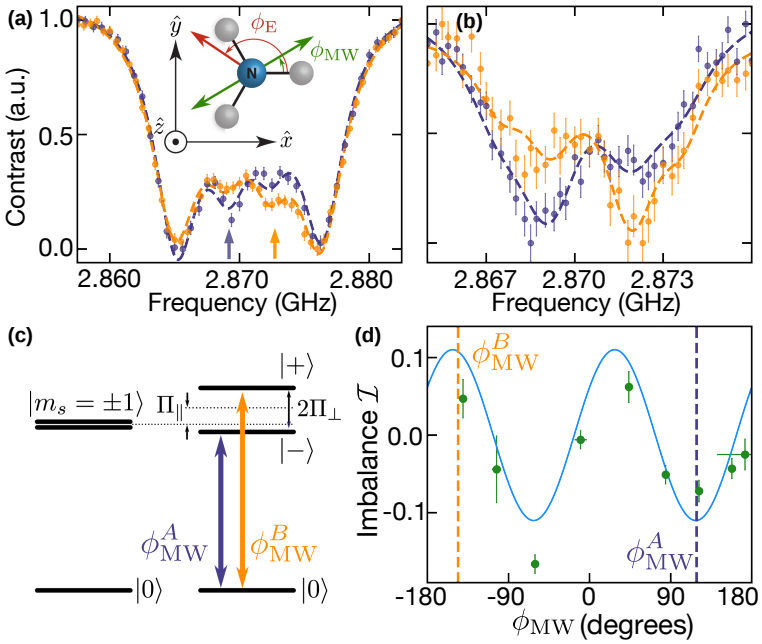


Figure 4.4: **Vector imaging of local electric fields by modulating MW polarization [75]:** (a-b) The application of linearly polarized microwaves allows us to modulate the transition amplitudes between $|m_S = 0\rangle \leftrightarrow |\pm\rangle$ (eigenstates under electric field) for single NV centers. In the case of low electric field strength (a), we look at the modulation of the inner two peaks ($|m_I = 0\rangle$). In the case of higher electric field strength (b), we look at the modulation of the two resonances. The inset in (a) is an illustration showing the orientation of the microwave polarization ($\phi_{MW}$) relative to the transverse electric field ($\phi_E$) in the frame of the NV center. The rotation of the MW polarization results in modulation of the resonance amplitudes allowing us to measure $\phi_E$. (c) A illustration showing the eigenstates in the presence of an electric field yielding a shift ($\Pi_z$) and splitting ($2\Pi_\perp$). MW polarization along $\phi^A_{MW}$ ($\phi^B_{MW}$) yield maximal resonance amplitude for $|-\rangle$ ($|+\rangle$). (d) Measuring the change in imbalance ($\mathcal{I}$) of resonance amplitudes on rotating the MW polarization allows us to extract $\phi_E$. Data is shown for a single NV center in (a). Dashed lines indicate the $\phi_{MW}$ values for spectra plotted in (a).

The transition matrix elements between the $|m_S = 0\rangle$ state the above eigenstates can be modulated by linear polarized microwaves. Specifically, by applying MW polarized along

$\phi_{MW}$ ($\vec{B} \sim (\cos(\phi_{MW})B_x\vec{e_x} + \sin(\phi_{MW})B_y\vec{e_y})e^{i\nu t}$) in the transverse ($xy$) plane in the frame of the NV center, it is possible to observe an imbalance in the cwODMR contrast of the two resonances. Defining, the imbalance $\mathcal{I} = (A_+ - A-)/(A_+ + A_-)$ where $A_\pm$ is the amplitude of $|m_S = 0\rangle \leftrightarrow |\pm 1\rangle$ transition we find [75]

$$\mathcal{I} \sim -\cos(2\phi_{MW} + \phi_E)$$

Modulating $\phi_{MW}$, we can measure $\phi_E$ (thereby $\Pi_y/\Pi_x$). Furthermore, we can measure the full electric field by extracting $\Pi_z$ and $\Pi_\perp = \sqrt{\Pi_x^2 + \Pi_y^2}$ vector in the frame of the NV center.

## 4.4 Conclusion

In this chapter, I have departed from the larger narrative of the thesis to discuss a study wherein the NV spectrum is not dictated by stress. Instead, at ambient conditions, the effect of electric fields emanating from charged defects in the local environment of the NV centers dictates the spin eigenstates. There is an important connection between stress and electric fields. Namely, the similarity of their Hamiltonians allows the technique of vector electrometry to carry over to cases where the NV spectrum is influenced by crystal stress. In the case of electric fields, due to averaging of random *local* electric field in high density samples, the technique of rotating MW polarizations to extract $\phi_E$ may not extend to ensemble measurements. Therefore, this technique remains restricted to single NV centers, as discussed in this chapter. However, in the case of a *global* stress field (as is realized by high pressure measurements), the possibility of rotating the MW polarization remains a viable method to obtain additional information on the stress in the sample. The challenge here is to rotate the microwave polarization in the high pressure environment. A simple extension of techniques already demonstrated under ambient conditions [4] may be a reasonable starting point!

# Chapter 5

# Imaging stress across nanoseismic faulting events in chrysotile Serpentine

Following our initial proof of concept demonstrations, it was clear that the NV center offered two key advantages as a probe for crystal stress:

- The ability to image stress with diffraction-limited spatial resolution
- The power to independently measure hydrostatic and deviatoric stress components

With a product in hand, the group went hunting in the seemingly unfathomable market of scientific questions to look for a meaningful use case. Quite amazingly, we did not have to look too far!

This project started as a collaboration with Dr. Thomas Smart and Prof. Raymond Jeanloz in the Earth and Planetary Sciences Dept. at Berkeley. Tom and Raymond were instrumental collaborators in taking our high pressure project off the ground. Tom was already studying acoustic emissions associated with amorphization in chrysotile Serpentine. The project played to the strengths of the NV center as a high pressure probe capable of imaging shear stress *in situ*. Joining forces on this effort was as fascinating as it was fun! A good portion of the work was done by Tom and collaborators (Sections 5.2 and 5.3). Here, I describe the full study to build the context of our scientific goals. However, details of displacement sensor calibration are omitted and I defer to Tom's thesis [93] and our paper (in preparation) as more authoritative sources on this part of the work.

## 5.1 Deep Earthquakes

Shallow earthquakes occur in the Earth's crust, and upper mantle due to **brittle fracturing** or **stable sliding** [38]. In the first case, an accumulation of stress causes rocks to fracture

without showing any plastic deformation. In the second case, seismic activity occurs due to the relative movement of rocks along fault lines. These failure mechanisms are not possible beyond depths of $\sim 60$ km due to the prevailing temperature and pressure conditions deeper in the Earth's mantle [38]. High temperatures induce the onset of ductile deformation of rocks as opposed to brittle fracturing. High pressures (normal stresses) increase friction along fault planes to combat sliding. Nevertheless, nearly a third of all earthquakes have foci located at depths from 60 km down to 700 km [39]. The first convincing case for such deep earthquakes was made as early as 1928 [39]. Despite decades of effort, microscopic mechanisms for deep earthquakes remain poorly understood.

Phase transformational faulting, whereby pressure and temperature-driven structural transformations in key mantle minerals underpin focal mechanisms [38], is an intriguing hypothesis for the origin of deep earthquakes. In the simplest case, the nucleation of a high density phase leading to volume collapse and runaway structural instabilities would result in **isotropic sources**. However, a key signature of deep seismicity (and earthquakes in general) is the observation of **double couple sources** with acoustic waves showing simultaneous tension and compression along mutually perpendicular axes (Fig. 5.1). This observation, though seemingly at odds with phase transformational faulting, not only rules out the simple volumetric collapse model but also hints at the role of deviatoric stress in driving faulting mechanisms. In this project, we study the amorphization of chrysotile Serpentine ($Mg_3(Si_2O_5)(OH)_4$), a structural phase transformation that is accompanied by the emission of acoustic waves, to explore the connection between nanoseismicity, failure mechanisms, and applied stress. Serpentine, California's state rock, is abundant in **subduction zones** where one tectonic plate slides under another [74]. Interestingly, deep earthquakes often occur in such regions where the accumulation of stress and temperature gradients can induce brittle-like failure [15].

Here, we use a three-pronged approach to highlight an instance of phase transformational faulting driven by deviatoric stress as one possible mechanism for deep earthquakes. First, using piezoelectric displacement sensors, we perform direct acoustic sensing on both compression and decompression up to 26 GPa (corresponding to lower mantle pressures). Our measurements elucidate the nature of the focal mechanism driving acoustic emissions. Second, we use X-ray diffraction (XRD) in conjunction with acoustic sensing to show that nanoseismic events coincide with structural amorphization. Finally, using NV centers to perform *in situ* stress imaging, we show the accumulation and relaxation of shear stresses on both compression and decompression. Interestingly, we find that sudden relaxations in shear stress are always accompanied by acoustic emissions.

## 5.2 Displacement sensing of nanoseismic events

In the first study, we use displacement sensing to characterize acoustic emission from Serpentine on compression and decompression up to 26 GPa (lower mantle pressures). Natural Serpentine (a mixture of Clino- and Ortho-chrysotile) was powdered with a mortar and

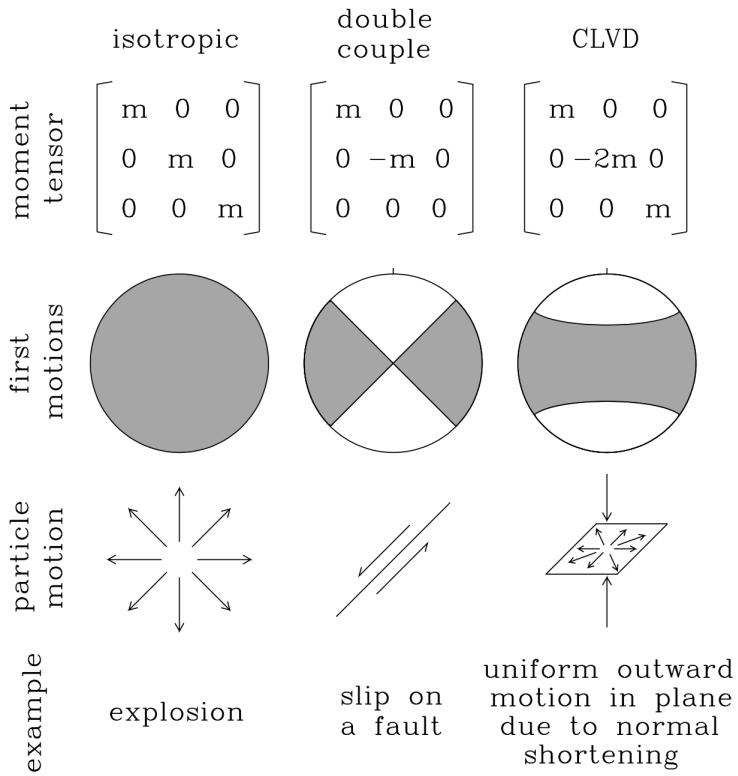


Figure 5.1: **Source mechanism of an earthquake (reproduced from [39]):** The moment tensor of an earthquake is a signature of its focal mechanism. This schematic in Frohlich's book [39] shows the three possible source mechanisms. An **isotropic source** shows uniform tension (or compression) as one would expect in a structural phase transition resulting in volume collapse. In contrast, a **double couple source** shows simultaneous tension and compression along mutually perpendicular directions. Finally, a **CLVD source** mimics the bursting of a water balloon, wherein tension along a plane is accompanied by compression (at twice the rate) along the normal direction. Seismic data from deep earthquakes point towards double couple sources, which rule out focal mechanisms driven by simple volume collapse.

pestle to prepare the sample. We compressed this powdered sample without pressure media to maximize the development of shear stresses. Using a Merril-Basset diamond cell (a triangular plate DAC) instrumented with four piezoelectric displacement sensors, we can characterize the source mechanism of nanoseismic faulting in our sample. We placed three sensors in the plane of the sample (perpendicular to the loading axis) and the fourth sensor parallel but off-center of the loading axis. The complicated loading geometry can lead to non-trivial acoustic transients in our sample. In particular, reflections of acoustic waves due to impedance mismatch at multiple interfaces between the sample and the displacement

sensor can befog a full characterization of the acoustic time series. To obviate these issues, we performed **first motion analysis** wherein only the initial trace of the acoustic signal was considered for source characterization. The viability of first motion analysis was verified by calibrating with known acoustic sources [93].

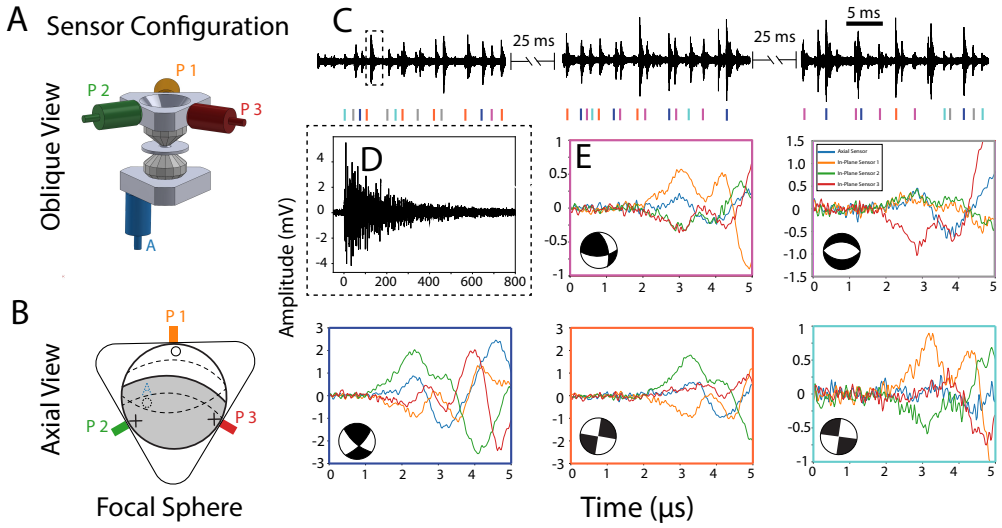


Figure 5.2: **Displacement sensing of acoustic emissions:** (a) A illustration of the DAC loading showing in-plane displacement sensors P1, P2, and P3 (orange, green, and red) and axial sensor A (blue). The sensors shown are color-coded with their respective signal traces. All sensors are coupled orthogonally to the DAC. (b) Top-down view of the DAC illustrating the determination of source mechanism. Simultaneous detection of compression (+ sign) on the P2 and P3 and tension (o sign) on P1 and A allow us to constrain the orientation of the double couple source. The most likely boundary between compressional and tensional regions of the source is shown by the convex solid black line in the center with possible angular error (broken black line). A concave broken line shows an alternative (but unlikely) source mechanism. (c) Time series data of displacement signals show clusters of acoustic emissions. (d) Full waveform of a typical acoustic emission. First, motion analysis can identify five categories of source mechanisms for this data set. Each acoustic emission in (c) is thereby ascribed to its particular first motion group (colored bars) (e) Example traces from each first motion type are color-coordinated to the colored bars under the emission cluster (c). Focal mechanisms (insets) show relative motions as viewed orthogonal to the compression axis, viewed along sensor 1. Data was collected and analyzed by Thomas Smart and Jes Parker.

We collected over 450 acoustic emissions at room temperature on compression between 6 GPa and 26 GPa and decompression down to 5 GPa. Intriguingly, even samples with a history of pressure cycling yielded further acoustic signals on re-compression. This observation

suggests that high pressure amorphization may be reversible on decompression. Crucially, first motion acoustic traces show a distribution of compression and tensional signals across the four displacement sensors (Fig. 5.2), establishing the presence of double couple sources (ruling out a pure isotropic source mechanism).

Sampling between 0.1-40 MHz first motion amplitudes vary between 0.3-3 mV depending on the strength of the acoustic signal and the coupling between the source and the sensor. Duration of first motions range from 1.2 µs to 1.7 µs for sample diameters of 90 µm and 170 µm, respectively. This indicates that fracture propagation speeds are a fraction ($\sim$ 4%) of the shear wave velocity in Serpentine ($v_S \approx 2.3\,\mu m\,ns^{-1}$ at ambient pressures) [83]. Furthermore, acoustic emission traces can be classified into distinct groups based on first motion characteristics. Cross-correlations between signals in the same first motion group show high correlation coefficients ($> 95\%$). Similar analysis on signals belonging to different first motion groups or signals from different sample loadings yields significantly smaller correlation coefficients of $40 - 80\%$. This observation suggests that signals from a first motion group stem from a single source [76]. Localized nucleations of high pressure phases leading to faulting are common in other systems (such as Ice I, $Mg_2GeO_4$) up to $\sim 5$ GPa [92, 43, 88]. However, this work demonstrates that such mechanisms remain viable in chrysotile Serpentine up to lower mantle pressures.

## 5.3 XRD characterization of failure mechanims

Having characterized acoustic signals, we performed X-ray diffraction (XRD) concurrently with displacement sensing to demonstrate the connection between amorphization and nanoseismicity in our sample. The crystal structure of Serpentine comprises magnesium-silicate layers stacked via hydrogen bonding [8]. We studied the sample at 300 K on compression from 8 GPa to 24 GPa, and on decompression down to 10 GPa. Indexing the diffraction peaks by the $hkl$ miller indices, the $[hk0]$ peaks correspond to the $a$ and $b$ axes defining the magnesium-silicate sheets [106]. The $c$ axis defining the stacking direction is represented by the $[00l]$ peaks.

On compression, all diffraction peaks broaden. Although we observe weak signals from some $[hk0]$ peaks, all $[00l]$ peaks are imperceptible at the highest pressures. On decompression, we observe the sharpening of some $[hk0]$ peaks ([020], [130], [060]). However, none of the erstwhile $[00l]$ peaks are recovered. Our observations paint the following microscopic picture of the amorphization process. The disappearance of the $[00l]$ peaks on compression suggests the breaking of weak hydrogen bonds between the stacked magnesium-silicate sheets. The intra-layer integrity, though disordered, is not completely destroyed at the highest pressures, as evidenced by the persistence of the $[hk0]$ peaks. On decompression, these individual magnesium-silicate layers partially recrystallize. Nevertheless, the long-range inter-layer stacking order is irreversibly lost after the initial compression cycle. As noted earlier, acoustic emissions are also observed on re-compression of samples with a history of pressure cycling. This suggests that the failure mechanisms responsible for acoustic emissions in Serpentine on

compression are not solely due to the disintegration of inter-layer hydrogen bonds. Rather, such emissions also emanate from disordering of individual magnesium sillicate layers.

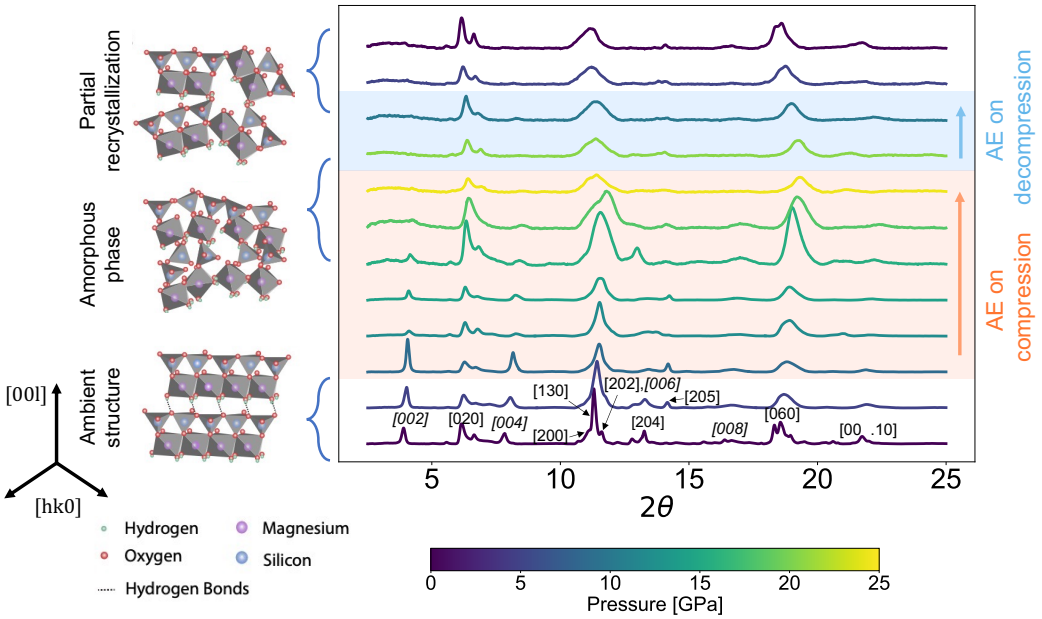


Figure 5.3: **X-ray diffraction:** (Right) XRD intensity versus $2\theta$ (diffraction angle) for a mixture of clino- and ortho-Chrysotile Serpentine on compression and decompression between $0 - 25\,\text{GPa}$. An orange (blue) background indicates that acoustic emissions (AE) were observed on compression (decompression). The color bar shows the ruby pressure for each XRD measurement. Miller indices for the relevant peaks are indicated on the ambient pressure diffraction pattern. Indices for $[00l]$ peaks are italicized. (Left) Illustrations show structural changes based on the interpretation of XRD data. Under ambient conditions, the stacked magnesium-silicate sheets in Serpentine are aligned in the $[hk0]$ plane and are held together with weak hydrogen bonding in the $[00l]$ direction. In the amorphous phase, there is disordering within each layer and a loss of inter-layer hydrogen bonding. On quenching the pressure, there is partial recrystallization of the magnesium silicate sheets, evidenced by the recovery of $[hk0]$ peaks. Preserved peaks ($[020], [130], [205], [060]$) are associated with the magnesium-silicate sheets. Peaks associated with the inter-layer stacking $[00l]$ are not recovered, suggesting the irreversible loss of inter-layer hydrogen bonding. The apparent doubling of the [020], [204], and [060] peaks is caused by the mixture of orthorhombic and monoclinic chrysotile in the sample. Data collected and analyzed by Thomas Smart and Jes Parker.

On decompression, further acoustic activity stems from the partial re-crystallization of these sheets. Furthermore, the strengthening of the $[hk0]$ peaks due to reordering precludes thermal disordering (such as frictional melting), which would induce long-range displace-

ment of the atoms from their equilibrium lattice positions [58]. Instead, our observations conclusively show that the sample remains solid.

**Note:** It is interesting to think about the thermodynamics of this phase transformation. It was non-intuitive to me that the sample should lose energy by emitting acoustic waves on both compression and decompression. At a qualitative level, the reversibility of this transition necessitates that the high pressure amorphous phase has a smaller volume than the low pressure crystalline phase. The act of compression, therefore, increases the free energy of the sample in this high pressure phase. On quenching the pressure, the partial relaxation of the sample to the crystalline phase with lower free energy is accompanied by the emission of acoustic waves.

## 5.4 The role of stress in sample failure and nanoseismicity

The overarching goal of our project was to learn the nature of acoustic emissions in chrysotile Serpentine, understand the failure mechanisms that gave rise to acoustic behavior, and explore the connection between sample stress and failure. Piezoelectric displacement sensors provided a diagnostic for detecting and characterizing the source mechanisms. X-ray diffraction provided a window into the microscopic origin of sample failure linking solid-state amorphization to nanoseismic faulting. Shear stress is often invoked as a driving mechanism for solid-state amorphization. However, experimental probes were hitherto unable to measure sample shear directly [43, 64, 57]. In this final study, we used NV centers to image the culet stress *in situ* to uncover this link between sample stress and acoustic activity.

### Widefield Imaging using NV center

We loaded the sample in a Pasternak DAC (Fig. 2.2 (c)) equipped with a single displacement center to monitor for acoustic emission events. We used a [111] cut Type Ib diamond with $\lesssim 1$ ppm concentration of NV centers incorporated up to 50 nm from the surface [49]. For this project, we relied solely on widefield imaging to generate stress maps. By operating in widefield modality, one can drastically reduce measurement time by performing spatially resolved cwODMR simultaneously over the entire culet. Fig. 5.4 (a) shows a schematic of a widefield apparatus with details in the caption.

We obtain a widefield cwODMR spectrum by taking fluorescence images of the sample on an EMCCD camera (Fig. 5.4 (b)) while synchronously tuning applied MW tones. The widefield dataset is, therefore, a three-dimensional matrix, where the first two indices fix the pixel row and column, and the third dimension maps to the applied MW frequency. At each pixel, we can plot the normalized fluorescence against the applied MW frequency to get a cwODMR spectrum.

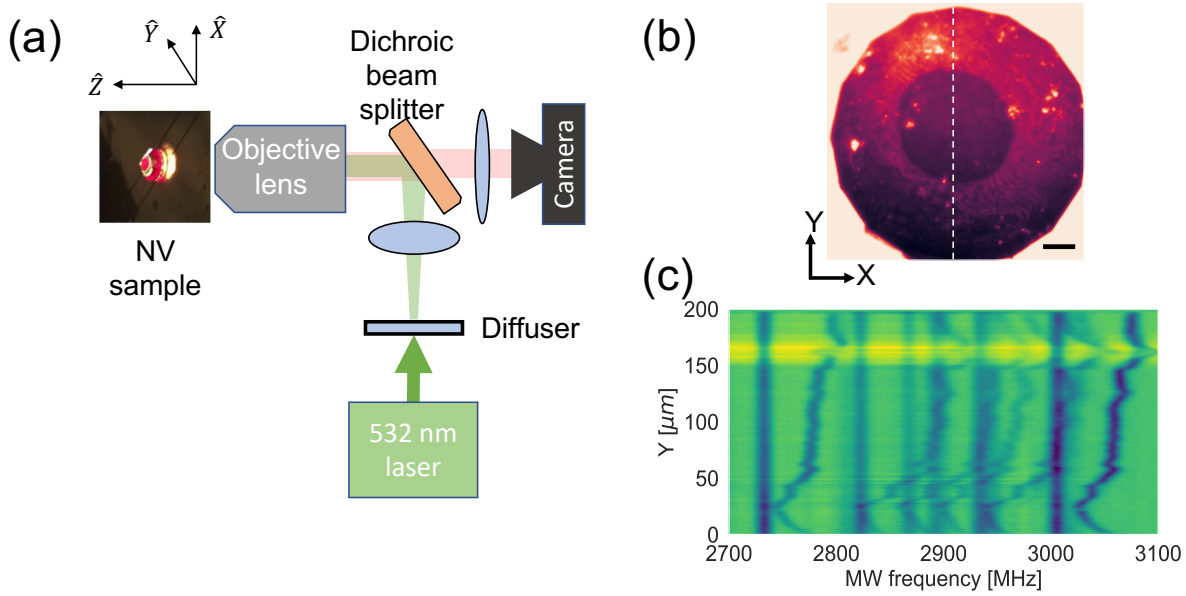


Figure 5.4: **Widefield Setup and Data:** (a) The 2 W 532 nm excitation laser from a Coherent Verdi V-2 is passed through an optical diffuser (Optotune LSR-3005-6D-VIS) and directed towards the sample. The diffuser reduces the spatial coherence of the laser and improves image quality. An aspheric lens curbs the beam's divergence after the diffuser. The sample's fluorescence is separated from the excitation path by a dichroic beam splitter (AVR Optics FF556-SDi01-25x36) and focused on an EMCCD camera (Princeton Instruments ProEM-HS: 512BX3). A condenser lens before the camera helps increase the field of view (FOV) of the setup to 200 µm × 200 µm and capture the full culet surface. The MW setup for the widefield apparatus is identical to Fig. 1.6. A $\vec{B}$ field was applied using three electromagnets oriented along the $\hat{X}, \hat{Y}$, and $\hat{Z}$ axes in the lab frame (b) A sample widefield fluorescence image of a 200 µm diamond culet (black scale bar shows 25 µm). One can make out the high pressure sample chamber and bright ruby pressure markers distributed across the culet. A widefield data set comprises a cwODMR spectrum at each pixel on this image. Taking a vertical linecut at the center of this image (broken white line), we can look at a so-called 'waterfall plot' (c), showing the spatial variation of the ODMR resonances along the column. In the waterfall plot, we observe two types of resonances. 'Background resonance lines' coming from NV centers in the facets show no spatial dependence. In contrast, resonances from NV centers at the culet show clear spatial dependence.

Looking at different slices of the widefield dataset as a **waterfall plot** can be a powerful way to understand the spatial structure of the NV resonances. Fig. 5.4 (c) shows a generic waterfall plot obtained by fixing the X location and looking at NV resonance lines against the position in Y. For vector magnetometry and tensor stress sensing experiments, such plots

can aid in attributing resonances to the four NV groups. To shorten acquisition times, a mean filter of a widefield dataset can also average down pixel noise (at the cost of spatial resolution).

In Fig. 5.4 (c), we can identify two types of resonances in the waterfall plot. The **background resonance lines** appear as uniform resonances with no apparent spatial dependence. These resonances are likely picked up from NV centers implanted on the facets of the diamond anvil. In contrast, resonances from NV centers in the culet show marked spatial dependence. The presence of background resonances can complicate the analysis of widefield maps. Nevertheless, far from the high pressure chamber, the facet NV centers experience negligible stress and primarily couple to the applied external field. Therefore, these background resonances can be used as an *in situ* $\vec{B}$ field calibrant allowing us to decouple the effects of the applied field and local changes in stress and magnetism on NV centers in the culet.

## Fitting Widefield Maps

A widefield cwODMR captures up to $512 \times 512$ sq. pixels of data within the same time as a single confocal measurement. Although this can be a massive win from a sensing standpoint, processing the data to extract useful information can be complicated. The challenges stem not only from the presence of additional background lines but also from possible complications in the NV resonances' spatial patterns. For example, one can imagine that a generic stress profile can cause resonances from different NV groups to overlap or 'cross' each other in sections of the data set. A naive Gaussian fitting procedure can fail or misattribute NV resonances to different groups. In practice, it is intractable to parse through the dataset and control for such cases. In this section, I will describe our approach to overcoming these challenges.

To simplify our approach, we used a [111] cut culet, where the lab frame and the NV frame for the [111] group are conincident. Applying a $\vec{B}$ field to separate the NV resonance lines, we identified the extremal culet resonances as those belonging to the [111] NV group (blue arrows in Fig. 5.5 (a)). The main challenge then was to fit these resonances for extracting the culet stress and, separately, the background resonances for extracting the magnetic fields.

Working with the approximation that the relative contrast of background lines is fixed throughout the dataset, we first identified pixels where the background and culet resonances are not overlapped. We then iteratively fit the background lines in these pixels, respecting the contrast ratios. Fig. 5.5 (b) shows an example of the resulting background resonance profile. When subsequently fitting to the resonances of [111] group of NV centers in the culet, we used an overall scaling of the background profile as a fitting parameter (Fig. 5.5 (c)). The center frequencies for a typical fit are shown in Fig. 5.5 (d) and (e). We can see an imprint of the sample-gasket boundary for both the left and right [111] peaks.

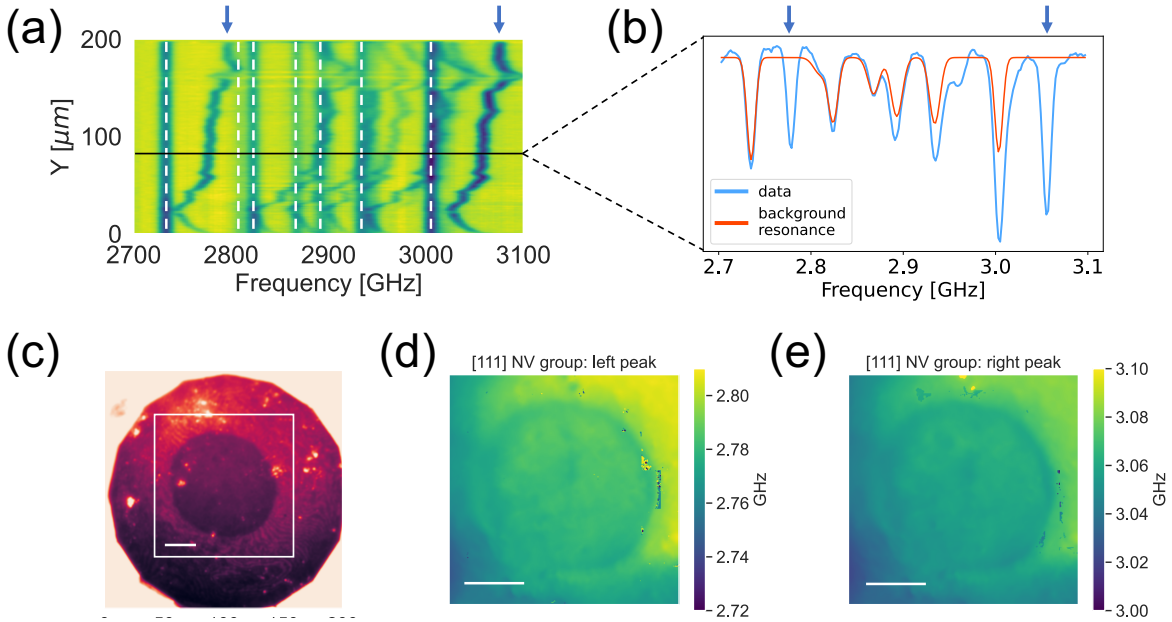


Figure 5.5: **Fitting Background Resonances (compression pressure point $\sim$ 6.75 GPa):** (a) We can identify the seven background resonances (white dashed lines) and resonances of the [111] NV group in the culet (blue arrows) in the waterfall plot. Identifying pixels showing the low overlap between the background and culet resonances, we can generate the background resonance profile. The center frequency of the background resonances is used to determine the applied magnetic field. (b) The resulting profile of background lines (with fixed relative contrast) can be scaled when fitting to resonances of the [111] NV group in the culet (blue arrow) to extract the stress parameters. (Note how much easier it is to identify and follow resonances in the waterfall plot (a) compared to the cwODMR signal for a single pixel (b)) (c) Restricting ourselves to the sample chamber region (white box), we fitting the resonances of the [111] NV group in the culet. (d) and (e) Fits of the center frequency for the left and right [111] peaks in (a,b) clearly show the sample-gasket boundary. White scale bars on (c-e) denote 25 µm

## Modelling the stress environment

Considering the [111] NV group at the diamond culet, we can write down the Hamiltonian of the systems as follows:

$$H = \underbrace{D_{gs}\, S_z^2}_{H_0} + \underbrace{\gamma \vec{B} \cdot \vec{S}}_{H_B} + \underbrace{D(\overleftrightarrow{\sigma})\, S_z^2 + E(\overleftrightarrow{\sigma})(S_x^2 - S_y^2)}_{H_S} \tag{5.1}$$

where $H_0$ represents the zero-field splitting term ($D_{gs} = (2\pi) \times 2.87\,\text{GHz}$), $H_B$ is the coupling of the NV spin to the applied $\vec{B}$ field ($\gamma \sim (2\pi) \times 2.8\,\text{MHz/G}$), and $H_S$ is the coupling of the NV center to the crystal stress $\overleftrightarrow{\sigma}$ [49]. As mentioned earlier (Section 3.1), the symmetry preserving stress manifests as a shift in the NV resonance frequency of magnitude $D$, and the symmetry breaking stress causes the $|m_s = \pm 1\rangle$ states to mix and split by $2E$ (in the absence of a $\vec{B}$ field). The $(D, E)$ stress parameters are functions of the crystal stress, as given below:

$$D = \alpha_1(\sigma_{xx} + \sigma_{yy}) + \beta_1\sigma_{zz} \tag{5.2}$$

$$E = \sqrt{E_x^2 + E_y^2} \tag{5.3}$$

$$E_x = \alpha_2(\sigma_{xx} - \sigma_{yy}) + \beta_2(2\sigma_{xz}) \tag{5.4}$$

$$E_y = \alpha_2(2\sigma_{xy}) + \beta_2(2\sigma_{yz}) \tag{5.5}$$

where $\{\alpha_1, \beta_1, \alpha_2, \beta_2\} = (2\pi) \times \{8.6(2), -2.5(4), -1.95(9), -4.50(8)\}$ MHz/GPa [49]. We neglect the $E_{x,y}$ terms in Eq. 5.1 because we are only interested in the energies (shift and splitting) of the NV spin. If we were interested in the eigenstate structure of the NV spin under stress, it would be important to consider the full stress Hamiltonian:

$$H_S = D(\overleftrightarrow{\sigma})S_z^2 + E_x(\overleftrightarrow{\sigma})(S_x^2 - S_y^2) + E_y(\overleftrightarrow{\sigma})(S_xS_y + S_yS_x)$$

Our model has five free parameters: $\vec{B} = (B_x, B_y, B_z)$ and $(D, E)$. The task at hand is to extract these numbers from the data. As alluded to already, we will use the background resonances to extract the applied $\vec{B}$ field and subsequently use this estimate to extract the stress parameters.

## Extracting applied magnetic field

Knowing that the applied $\vec{B}$ field is largely oriented along the [111] direction ($\hat{Z}$ in Fig. 5.6 (a)), we can identify the outermost peaks in the background resonances as belonging to the [111] NV group. We want to solve for the $\vec{B}$ field vector in the frame of this group which is equivalent to the lab frame (shown Fig. 5.4 (a)). We start with the model:

$$H = \sum_{i \in \{1,2,3,4\}} D_{gs}S_{z,i}^2 + \gamma\,\vec{B}^{(i)} \cdot \vec{S}_i \tag{5.6}$$

where $i$ enumerates the four NV groups. Seeding an estimate of the $\vec{B}$ field in the frame of the [111] NV group, magnetic field $\vec{B}^{(i)}$ in the frame of the other three NV groups is obtained by using the appropriate rotation matrices. A simple least square routine [103] to fit the resonance frequencies of the background lines provides an estimation of the applied magnetic field.

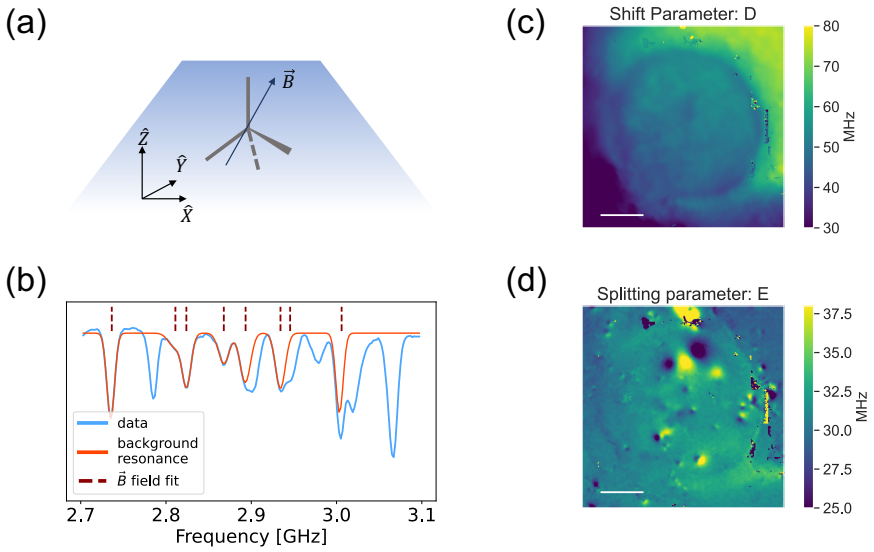


Figure 5.6: **Extracting stress parameters:** (a) For this study, we used a [111] cut diamond anvil. The orientation of the four NV groups with respect to the lab frame is shown. Note that the [111] group is oriented along $\hat{Z}$, and the applied B field is largely pointed along this direction. This allows us to ascribe the outermost background resonances to the [111] NV group. (b) We fit for the applied $\vec{B}$ field in the [111] NV frame (coincident with the lab frame). The solution is over-constrained because we have three free parameters $(B_x, B_y, B_z)$ and seven center frequencies from the background resonances (for this particular data point, an eighth resonance is neglected due to low contrast). Fitting to the $\vec{B}$ field, we plot the predicted eight resonances (dashed red lines). (c) and (d) It is straightforward to extract the stress parameters $(D, E)$ given a known background field. The $D$ and $E$ maps show qualitatively different features, but the sample-gasket boundary can be distinguished in both cases. White scale bars on (c) and (d) denote 25 µm.

**Note:** We can neglect the effect of pressure on the background resonance. This may not be valid for culet pressures nearing $\sim 50 - 100$ GPa, where shift term may need to be included. However, for lower pressures (up to $\sim 10$ GPa), our approximation is robust.

## Extracting $(D, E)$ stress parameters

Knowing the value of the background field, we can simply solve Eq. 5.1 to map out the stress parameters $(D, E)$ as shown in Fig. 5.6 (c) and (d). The shift parameter $D$ measures the symmetry-preserving stress, whereas the splitting parameter $E$ measures the symmetry breaking stress.

It is important to note that our model assumed that the magnetic field is uniform across the culet. While this is true for the $\vec{B}$ field applied using the electromagnet coils in the setup,

it was subsequently discovered that there were parasitic local fields in the high pressure chamber stemming from magnetite impurities in our sample. These fields lead to qualitatively different features in the maps of $D$ and $E$, as seen in Fig. 5.6. The $D$ stress parameter is robust to magnetic fields ($S_z^2$ commutes with $B_z S_z$ terms, and $B_{x,y}$ fields are suppressed to second order). For the $E$ parameter, the contribution to the NV splitting is already second order in the presence of this background field. Any parasitic $B_z$ field adds linearly with the applied background field to further suppress the symmetry breaking stress term in the NV splitting.

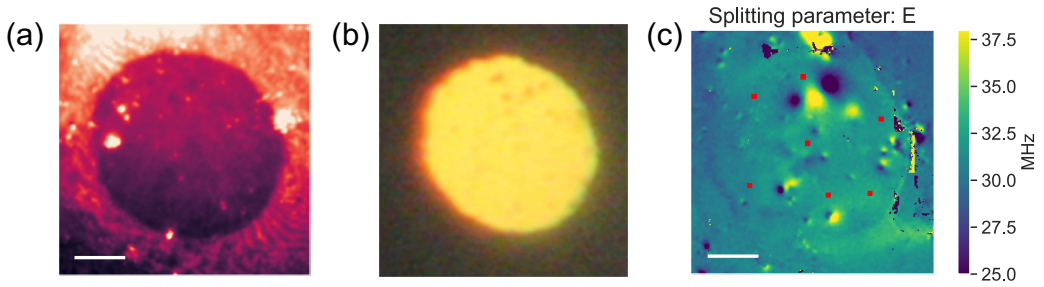


Figure 5.7: **Magnetite impurities in the sample:** (a) Fluorescence widefield image of the high pressure chamber shows ruby particles (bright spots) scattered throughout the culet surface. (b) A white light image shows grains in the sample chamber at points that do not show marked ruby fluorescence but instead show dipole patterns in the map of the $E$ parameter in (c). This suggests that these grains are magnetite impurities creating a parasitic local field. Since it is invalid to attribute the splitting entirely to culet stress near these particles, we sample the stress parameters at select points (red squares) around the high-pressure chamber to get an estimate of the true values of $D$ and $E$.

In Fig. 5.7 (b), it is evident that the map of the splitting parameter contains numerous dipole patterns that are characteristic of magnetic impurities. In particular, some of these dipole patterns are located near granular impurities observed in a white light microscope image (a). While our model for extracting the stress parameters is not valid near these grains, we sample spatial points in the chamber further away from these dipole patterns to estimate the $D$ and $E$ stress parameters for our study.

**Note :** The fact that these spatial patterns are manifest only in the splitting and not the shift suggests that they stem from local magnetism and not contact stress from non-magnetic particles in our sample (such as ruby).

## Connection between stress and sample failure

Although it is not straightforward to reconstruct the stress in the high pressure sample from our measurements at the sample-diamond interface, the $\sigma_{zz}, \sigma_{xz}$, and $\sigma_{yz}$ stress components

are continuous across the boundary. Furthermore, we posit that by sampling away from the magnetite impurities, we can approximate $E \sim 2\beta_2\sqrt{\sigma_{xz}^2 + \sigma_{yz}^2}$. Noting that we have an approximately centrosymmetric system, we neglect $\sigma_{xx} - \sigma_{yy}$ terms. Furthermore, observing that the gasket flow is primarily in the radial direction, we can approximate $\sigma_{xy} \approx 0$ and $\sigma_{\theta z} \approx 0$. The remaining symmetry breaking stress $\sigma_{rz}$ comprises $\sigma_{xz}$ and $\sigma_{yz}$ terms.

Therefore, the value of the shift parameter $D$ (due to $\sigma_{zz}$ and $\sigma_{\perp}$) is representative of the sample pressure, whereas the value of the splitting parameter $E$ is indicative of the deviatoric (primarily shear) stress in the sample. In the former case, we used an empirical calibration of the $D$ stress parameter ($dD/dP \sim 8\,\mathrm{MHz/GPa}$)[49] to convert the measured shift to pressure in the sample chamber. In the latter case, assuming that $\sigma_{xz}$ and $\sigma_{yz}$ dominate the splitting, we can convert the measured splitting into effective shear stress ($dE/d\sigma_{rz} \sim 2\beta_2 \sim 9\,\mathrm{MHz/GPa}$).

Monitoring the $(D, E)$ stress parameters on both compression and decompression, we observe markedly different qualitative behavior in the hydrostatic and shear stresses (Fig. 5.8). The $D$ parameter correlates linearly with hydrostatic pressure (measured using a ruby pressure marker) without any perceptible connections to acoustic emission events. In contrast, the $E$ parameter accumulates on compression, followed by characteristic dissipation concurrent with acoustic emission events. This illustrates that hydrostatic stress plays a relatively minor role in driving amorphization, whereas a build-up of shear stress beyond the shear strength of the sample induces failure. This failure and the accompanied relaxation of shear stress is consistent with volume collapse associated with the disordering of the magnesium-silicate sheets as observed in XRD. On decompression, we observe a pronounced increase in $E$ coincident with acoustic emission, suggesting the reversible nature of the transition. We interpret this increase as an indication of sample recrystallization causing volume expansion within the confining anvils.

We note that peak shear values are a factor of two higher for samples that have undergone a cycle of amorphization and recrystallization (Fig. 5.8 (c)) than samples that have not (Fig. 5.8(b)). There are two plausible contributions to this increase in the material's shear strength. First, the initial cycle of amorphization and recrystallization irreversibly destroys hydrogen bonds in chrysotile Serpentine. The resulting compactification allows the sample to support higher loads before failure. Second, this initial compression and decompression cycle also causes plastic deformation in the metallic gasket. This thinning of the gasket reduces its confining force on the sample on successive compression. This allows the sample to spread out on compression, causing an increase in shear stress at the sample-diamond interface.

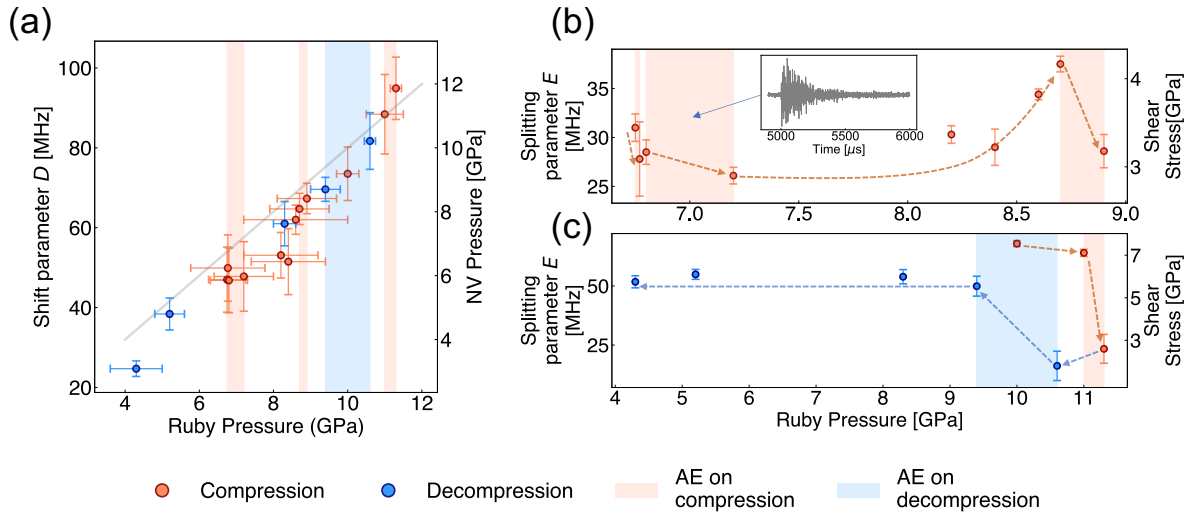


Figure 5.8: **Studying changes in $(D, E)$ across acoustic emission events:** (a) The $D$ (shift) parameter shows a linear increase with applied pressure (measured using ruby fluorescence). An empirical conversion of $dD/dP \approx 8\,\text{MHz/GPa}$ gives a precise correspondence between the ruby and NV pressure gauges (the grey line shows $x = y$ between the two pressure axes). Crucially, we see no clear change in the shift parameter across acoustic emission (AE) events on both compression (orange) and decompression (blue). **Note:** In the case of [111] cut culet, it is not possible to decouple the $\sigma_{zz}$ and $\sigma_{\perp}$ terms based on the shift alone. We use an empirical conversion to simplify the challenge of pressure calibration using the NV center. Nevertheless, the exact value of $dD/dP$ may depend on the material (or pressure medium) in the sample chamber. (b) Tracking the $E$ (splitting) parameter, sampled across the high pressure chamber, we see a qualitatively different behavior compared to the shift. On compression, there is a consistent accumulation of symmetry breaking stress up to AE events (the inset shows an AE trace). Concurrent with AE, we see a clear drop in the $E$ parameter suggesting a relaxation of this stress. (c) The behavior of the $E$ parameter is the same for samples that have already undergone a cycle of compression and decompression. In this plot, we track the $E$ parameter on such a sample, seeing jumps in the splitting parameter on further compression and decompression.
**Note:** Modelling $E = 2\beta_2\sqrt{\sigma_{xz}^2 + \sigma_{yz}^2}$, we can extract the shear stress (shown in (b) and (c)) from the splitting parameter. Error bars show a range in the $D$ and $E$ parameters instead of standard deviation.

### Spatial variation in stress

To take a closer look at the spatial pattern of the shift and splitting parameters, we performed image registration [105] of widefield data sets at two pressure points (ruby pressures of

8.7 GPa and 8.9 GPa on compression in Fig. 5.2 (b)).

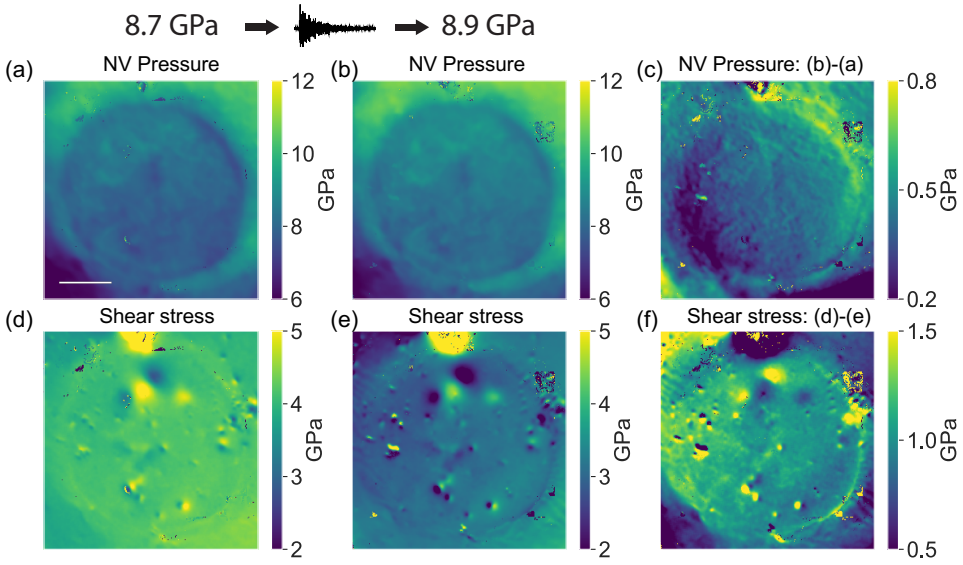


Figure 5.9: **Spatial analysis of pressure and shear stress:** Maps of pressure (top row) and shear stress (bottom row) extracted from the $(D, E)$ stress parameters. Image correlated maps of the NV pressure across the sample chamber for pressure points (a) 8.7 GPa and (b) 8.9 GPa on compression. We see clear acoustic emissions between the pressure points (shown on the top left). (c) Difference map of NV pressure: (b)-(a) We do not see telling micron scale features in the stress maps, perhaps because of the equilibration of local stress perturbations during data acquisition. Shear stress maps for the same pressure points are shown in (d) and (e). (f) Difference in shear stress: (d) - (e) (the order is changed because the pressure point at 8.7 GPa shows higher shear stress before AE). We see a clear build-up of shear at the sample gasket boundary (lower right). The simple difference does not remove features stemming from parasitic magnetic fields because splittings due to stress and magnetism add in quadrature.

The two pressure points lie immediately before and after an acoustic emission (AE) event (Fig. 5.9). Using the shift and splitting parameters to denote the pressure and shear stress, we plot the difference maps for these quantities across the AE event. We do not observe significant micron-scale variations in the difference maps, perhaps due to the equilibration of the sample during data acquisition ($\sim$ 1 day for each pressure point). We observe a concentration of shear stress in the sample-gasket boundary suggesting the presence of heterogeneities or interfaces can serve as regions for the nucleation of large shear values.

## 5.5 Conclusion

This chapter details an application of NV sensing in geophysics. Specifically, the ability to make spatially resolved maps of tensorial stress can find broad usage in many such investigations. Unfortunately, the competition between parasitic magnetic fields and interfacial stress can complicate the extraction of material parameters - something that must be considered in future investigations. Furthermore, the appropriate choice of crystal cut can make extracting the parameter of choice easier. In our case, the symmetry preserving and symmetry breaking stress components for the [111] NV group directly map to elements of the stress tensor in the lab frame. However, separating $\sigma_{zz}$ and $\sigma_{\perp}$ stress can allow for better pressure calibration in the sample chamber. Full stress tensor reconstruction using all eight NV resonances is only possible if appropriate data fitting routines can be developed to deal with widefield datasets. To this end, finding robust protocols to identify different NV groups, tackle degeneracies in the NV spectrum, and separate culet and background resonances is crucial. In the last case, one can eliminate background resonances by only generating NVs in the culet region. Nevertheless, background resonances are advantageous for sensing studies as an independent calibrant for the applied vector magnetic field.

In the context of geophysical explorations, where the ability to tune pressure and temperature is crucial, NV sensing can be performed under heating up to $\sim 600\,\mathrm{K}$ [67] and potentially extended to temperatures of $\sim 1000\,\mathrm{K}$ [68]. Our platform is fully compatible with resistive heating techniques in DACs [35]. Moving beyond the development of the NV sensor as a tensorial stress gauge, it will be interesting to see the geophysical applications of this tool in conjunction with other probes!

# Chapter 6

# The road to megabar pressures

More than half of my time in graduate school was spent trying to develop NV sensing capabilities at $\sim 100\,\mathrm{GPa}$ pressures. At the outset, it was not clear (to any of us) if this was even possible!

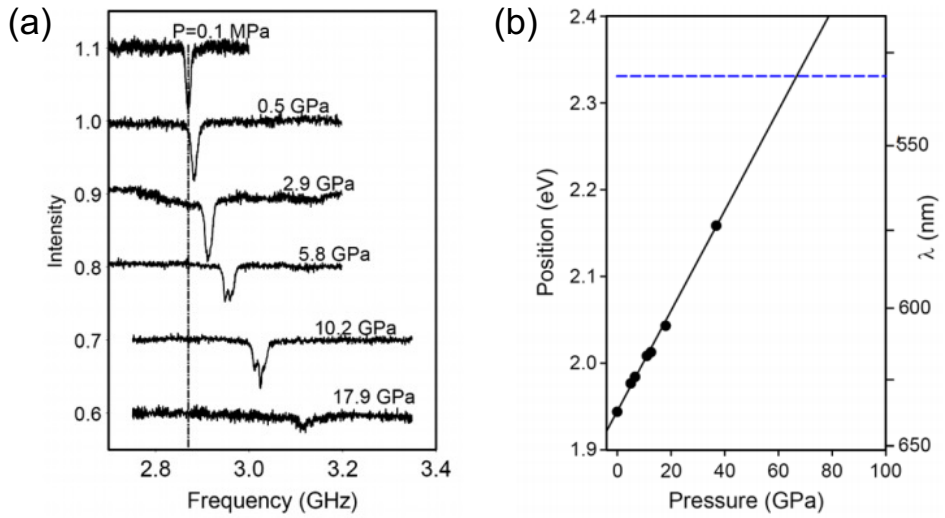


Figure 6.1: **Preliminary studies of NV centers under pressure (figures reproduced from [28]):** Doherty *et al.* [28] conducted an early study of the dependence of the electronic and spin properties of the NV center under hydrostatic pressure. (a) In their experiments, the cwODMR line showed a drastic reduction in contrast with the increase in pressure. (b) Based on data acquired in [28], the shift in the optical zero phonon line (ZPL) was projected to cross 532 nm (green line) at $\sim 66\,\mathrm{GPa}$ potentially precluding standard excitation schemes for NV experiments.

Previous work had hedged the odds against us (Fig. 6.1). In 2014, Doherty *et al.* [28]

had shown that the zero phonon line of the NV center moves towards higher frequencies under hydrostatic pressure. At $\sim$ 66 GPa the optical transition was projected to cross 532 nm, potentially nullifying the standard technique of working with the NV center. In addition, their measurements up to $\sim$ 60 GPa showed a drastic decrease in cwODMR contrast with pressure. Under the weight of our misguided pessimism, we were convinced that high stress gradients developed in the anvil at megabar pressures would pose an insurmountable challenge to NV sensing. After our synergistic endeavor to show the NV's usefulness as a high pressure sensor up to $\sim$ 30 GPa, we argued about our misgivings to Prof. Jean Francois Roche. He mentioned that he was exploring the idea of using shorter wavelengths for electronic excitation at hydrostatic pressures $>$ 70 GPa. Barring potential changes to the NV charge state population, Prof. Roche's optimism gave us a starting point. This chapter begins by chronicling some of my early 'failures' in pushing NV sensing to megabar pressures. Our meandering approach was filled with pitfalls and dead ends. However, the surprising finding of positive contrast ultimately directed us toward our end goal.

**Note:** Our first task was to verify if a simple linear extrapolation of the data measured by Doherty *et al.* [28] was valid up to megabar pressures. Rather, Density Functional Theory (DFT) estimates performed by He Ma in Prof. Giulia Galli's group predicted a more gradual blue shifting of the ZPL, suggesting 532 nm excitation remains viable up to $\sim$ 100 GPa. Ma's estimates have since been experimentally verified by Lyapin *et al.* [69]. Nevertheless, this initial study gave us some impetus to push ahead to higher pressures.

## 6.1 Microdiamonds in hydrostatic pressure

My first loadings were dedicated to studying NV properties under hydrostatic pressure using the 17 mm DAC provided by Prof. Struzhkin. Following the experiments conducted by Doherty *et al.* [28], we loaded microdiamonds (sourced from Adamas Nanotechnologies) in the sample chamber using salt (cesium iodide or potassium chloride) as a pressure medium and ruby as a pressure marker.

Under the mandate of compressing till the diamonds failed, I studied the photoluminescence and cwODMR response of the NV center to both 532 nm and 405 nm excitation up to pressures of 100 GPa. Although there was much to be desired regarding data quality, the first successful loading provided some exciting results (Fig. 6.2). No cwODMR resonance was observed at low pressures with 405 nm excitation. However, near $\sim$ 100 GPa, we observed a gradual appearance of a resonance line that corresponded clearly to the observed cwODMR resonance for 532 nm excitation. Accordingly, PL spectra at low pressures showed a marked difference between $NV^0$ and $NV^-$ fluorescence for the two excitation wavelengths. Specifically, 405 nm excitation showed a higher proportion of fluorescence coming from the $NV^0$ charge state consistent with the fact that the neutral charge state population dominates on excitation at these wavelengths [7]. However, there is a closer correspondence between PL spectra near megabar pressures suggesting comparable charge state populations for 532 nm and 405 nm excitation (Fig. 6.2 (e)).

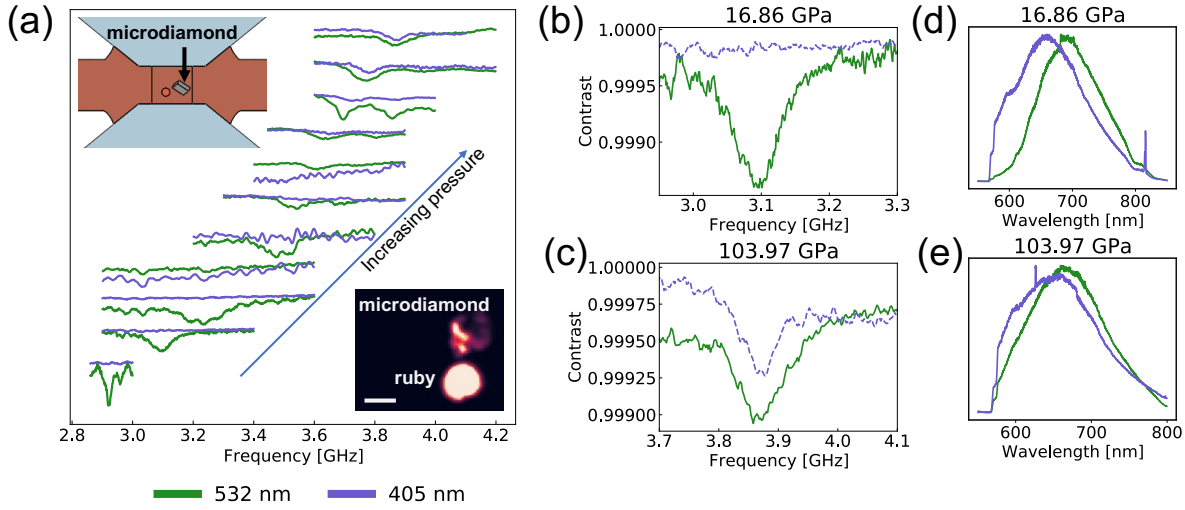


Figure 6.2: **NV response to hydrostatic pressure:** (a) (Top left inset) A loading of microdiamond using salt (CsI) as a pressure medium was used to study the NV response to hydrostatic pressure. cwODMR data obtained for excitation wavelengths 532 nm (green) and 405 nm (violet) are shown at all pressure points. The data clearly shows an appearance of a cwODMR resonance under 405 nm excitation at higher pressures. (Bottom right inset) A fluorescence scan shows the ruby pressure marker and a microdiamond. White scale bar denotes $\sim$ 10 µm. (b) cwODMR spectra at $\sim$ 17 GPa shows a clear resonance for 532 nm excitation and no clear resonance for 405 nm excitation. In contrast, (c) shows a clear resonance for both excitation wavelengths at $\sim$ 100 GPa. (d) Photoluminescence (PL) spectra at $\sim$ 17 GPa show strong $NV^-$ emission $>$ 637 nm and low $NV^0$ emission for 532 nm excitation. At these lower pressures, 405 nm emission shows a stronger $NV^0$ contribution to the PL spectrum. (e) At $\sim$ 100 GPa, PL spectra for both excitation wavelengths show better correspondence with a clear $NV^-$ contribution.

Despite some lukewarm success, the cwODMR spectra were remarkably unsatisfactory due to abysmal SNR. At some pressure points, there were no clear resonances for either excitation wavelength. In addition, there was disagreement between the ruby pressure and the expected NV resonance line [28] suggesting large pressure gradients in the medium. Crucially, acquisition times were painfully long, sometimes requiring a day or two for the shot noise to average down. In other words, even if it were possible to get 'some' signal from NV centers at 1 megabar, it was not obvious whether it would translate into a meaningful sensing platform. It was around this point that we learned about the use of insulating gaskets to perform pulsed measurements with NV centers up to $\sim$ 30 GPa [90]. The circuitous journey to develop pulsed measurements, tangential to the current scope, is omitted. In summary, a series of serendipitous meetings with Dr. Zachary Geballe helped me get started on the next steps toward improving SNR and pushing ahead.

**Note:** Since this study, Dai *et al.* [25] have compressed microdiamonds in the sample chamber to 140 GPa pressures suggesting this technique remains viable up to megabar pressures. Contrary to previous expectations, they could use 532 nm excitations up to the highest pressures. This is consistent with a non-linear shift in the NV ZPL under pressure as observed by Lyapin *et al.* [69].

## 6.2 Sensing with a [100] cut culet

Anecdotally, NV centers in bulk diamonds often show better contrast properties (likely due to surface charge and strain effects in the latter). With this in mind, I next explored the stress response of NV centers in the anvil with the goal of better signal integrity. Testing an anvil with a [100] crystal cut was the logical next step. With the four NV groups degenerate with respect to the loading axis, it would be simpler to interpret the cwODMR spectra.

In this experiment, 200 µm flat culets were glued to the 17 mm miniature PPMS DAC [41]. A [100] cut type Ib diamond with a layer of NV ensembles incorporated $\sim 50$ nm from the surface was aligned on the piston side. An untreated type Ia diamond was glued to the cylinder side of the DAC. Because of the absorption of excitation light at wavelengths $< 500$ nm by type Ib diamond, the only way to test NV response to different wavelengths was to image through the Type Ia diamond on the cylinder side. Consequently, we could only observe the response of NV centers in the sample chamber region.

### cwODMR with multiple excitation wavelengths

Compressing up to $\sim 70$ GPa, we performed confocal measurements with 532 nm and 450 nm excitation and widefield measurements with 532 nm excitation. The signal-to-noise ratio (SNR) was computed as SNR $\sim \sqrt{\text{counts}} * \text{contrast}$. In this case, we observed no significant change in the SNR at high pressures ($\gtrsim 50$ GPa) with either excitation wavelength. Fig. 6.3 shows a comparison of cwODMR contrast at these pressures and a rough comparison of SNR at different pressures for similar laser and microwave powers. Moving forward, there is room for further exploration on this front. In particular, a careful study of SNR using more wavelengths for different stress profiles may be interesting to pursue.

### Measuring Crystal stress

For a [100] cut anvil, dominant culet stresses in the crystal frame ($\sigma_{ZZ}$ and $\sigma_{\perp} = (\sigma_{XX} + \sigma_{YY})/2$) have both symmetry preserving and symmetry breaking components that project degenerately on the four NV groups. Therefore, we anticipate shifting and splitting in the NV resonance line based on Eq. 3.1. The shift parameter $D$ and the splitting parameter $E$

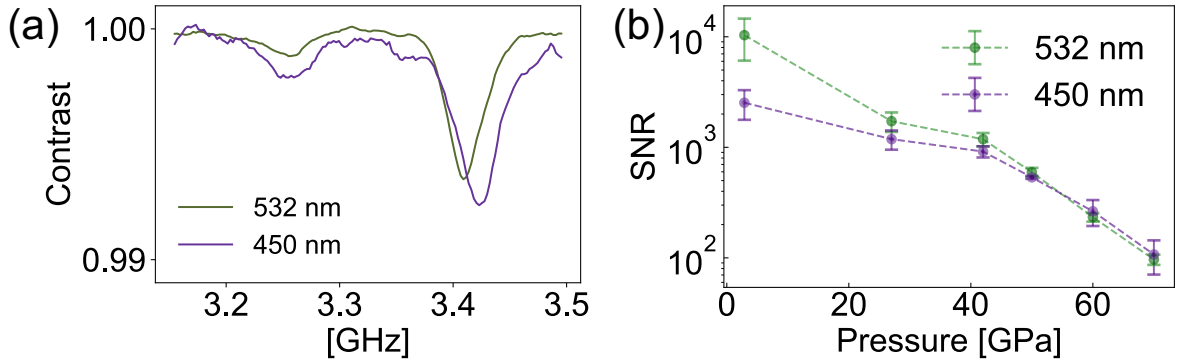


Figure 6.3: **Comparison of cwODMR signal with multiple excitation wavelengths:** (a) A comparison of cwODMR spectra with different excitation wavelengths for a [100] cut culet at $\sim 50\,\text{GPa}$. (b) A comparison SNR $\sim$ contrast $* \sqrt{\text{counts}}$ in cwODMR for 532 nm and 450 nm excitation wavelengths shows no distinct advantage of working with higher energy excitation at high pressures for [100] cut culets.

depend on culet stress (in the lab frame) in the following manner:

$$\begin{aligned}\begin{pmatrix} D \\ E \end{pmatrix} &= \begin{pmatrix} \frac{4}{3}\alpha_1 + \frac{2}{3}\beta_1 & \frac{2}{3}\alpha_1 + \frac{1}{3}\beta_1 \\ -\frac{2}{3}\alpha_2 + \frac{2\sqrt{2}}{3}\beta_2 & \frac{2}{3}\alpha_2 - \frac{2\sqrt{2}}{3}\beta_2 \end{pmatrix} \begin{pmatrix} \sigma_\perp \\ \sigma_{ZZ} \end{pmatrix} \\ &\approx \begin{pmatrix} 9.72 & 4.86 \\ -2.94 & 2.94 \end{pmatrix} \begin{pmatrix} \sigma_\perp \\ \sigma_{ZZ} \end{pmatrix}\end{aligned} \tag{6.1}$$

Here, $\{\alpha_1, \beta_1, \alpha_2, \beta_2\} = (2\pi) \times \{8.6(2), -2.5(4), -1.95(9), -4.50(8)\}$ MHz/GPa are the stress susceptibility parameters. By convention, $\{\hat{X}, \hat{Y}, \hat{Z}\}$ refers to the lab (crystal) frame, and $\{\hat{x}, \hat{y}, \hat{z}\}$ refers to the NV frame. We used ruby and culet Raman spectra to calibrate the pressure in the sample chamber. In addition, we extracted $\sigma_{ZZ}$ and $\sigma_\perp$ stress terms from cwODMR measurements at the culet center. Comparing the two pressure gauges (Fig. 6.4), we observe a clear correspondence between the pressure in the sample chamber (read out using either ruby or culet Raman measurements) and the $\sigma_{ZZ}$ stress in the diamond (measured using the NV center). This is consistent with the continuity of the $\sigma_{ZZ}$ stress across the culet-sample boundary. Furthermore, a marked increase in the $\sigma_\perp$ stress at higher pressures suggest a 'cupping' of the diamond culet on compression [65]. These measurements demonstrate the viability of stress calibration using NV centers.

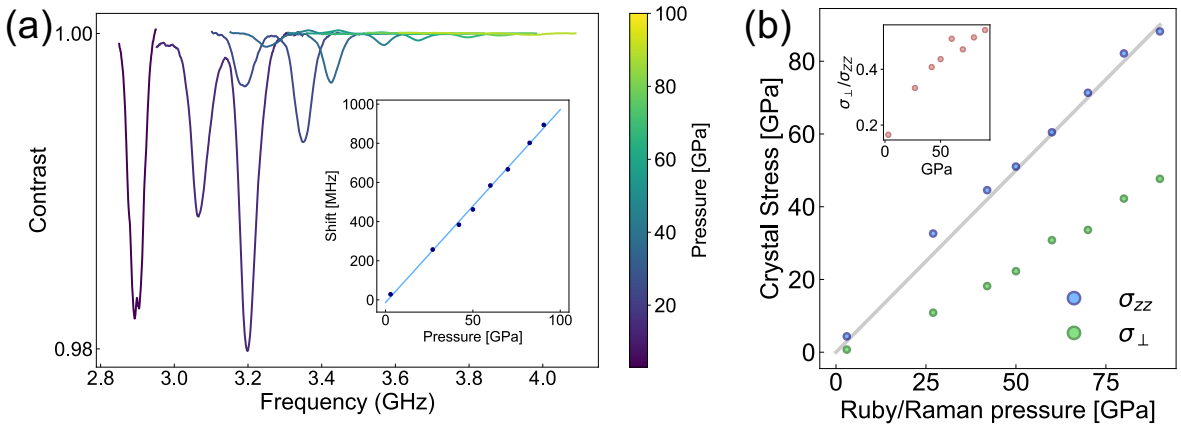


Figure 6.4: **Stress calibration using NV centers in a [100] cut culet:** (a) cwODMR measurements at the culet center show a pressure-induced shift ($D$) and splitting ($2E$) in the NV resonance due to symmetry preserving and symmetry breaking components in the stress. Note that there is a marked reduction in contrast with increasing pressure. (Inset) The measured shift in the resonance frequency is 9.8 MHz/GPa. (b) Using the shift and splitting measured at the center of the culet, the extracted crystal stress $\sigma_{ZZ}$ and $\sigma_\perp$ is plotted against the ruby/Raman pressure marker. There is a clear correspondence between the $\sigma_{ZZ}$ stress and the sample pressure (consistent with the continuity of this stress component across the diamond-sample interface). The grey line simply plotting $x = y$ (without any fitting to the data) demonstrates the viability of the NV center as a pressure calibrant. (Inset) The measured ratio of $\sigma_\perp$ to $\sigma_{ZZ}$ at each pressure step. There is a clear increase in the relative magnitude of $\sigma_\perp$ with pressure suggesting a cupping of the diamond culet with an increase in pressure [65].

## Spatial variation in the stress

Working in the widefield modality, we can image the uniaxial $\sigma_{ZZ}$ stress and biaxial $\sigma_\perp$ stress across the sample chamber. Mapping the stress can be a powerful way to observe pressure gradients in experiments directly. A detailed description of widefield cwODMR techniques and fitting protocols are already included in Section 5.4. I show a sampling of our data at two pressure steps. At high pressures ($\sim 40$ GPa), we observe a distinctive increase in the $\sigma_\perp$ stress component at the center of the sample chamber compared to the edge (Fig. 6.5 (e)). This is consistent with the cupping of the diamond culet under pressure [65].

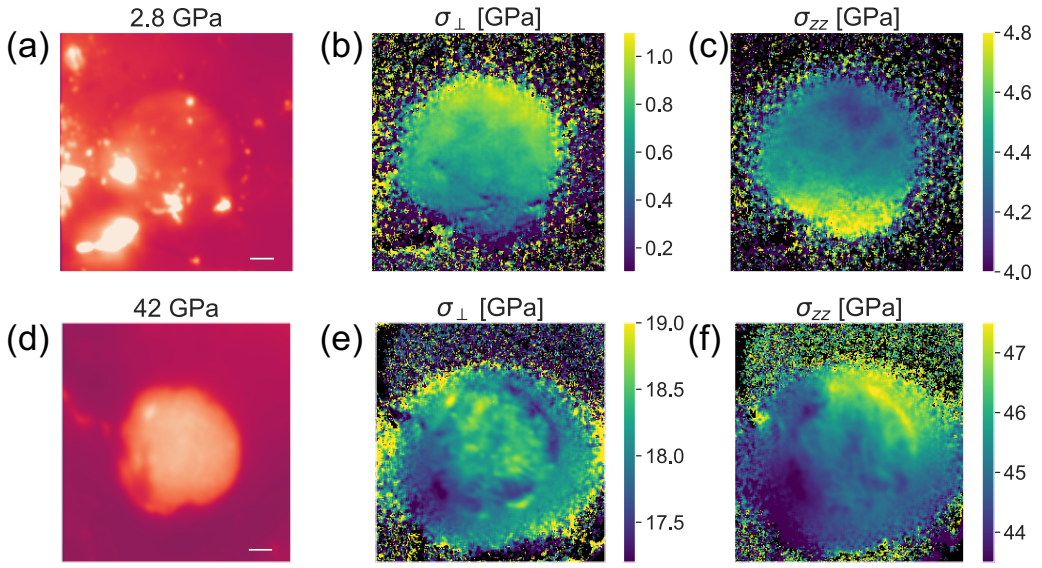


Figure 6.5: **Imaging stress in a [100] cut culet:** (a) and (d) show widefield fluorescence images of the sample chamber at 2.8 GPa and 42 GPa respectively (white scale bars show 10 µm). At low pressures, ruby microspheres scattered throughout the culet are markedly brighter than NV centers. Furthermore, due to the geometry of the loading, only NV centers in the sample chamber of the culet were optically accessible, restricting our study to this region. The ruby fluorescence is markedly diminished at high pressures relative to the NV centers. (b) and (e) are maps of the $\sigma_\perp$ stress in the sample chamber at the two pressure points. At low pressure, the stress distribution is comparatively uniform across the chamber. At high pressure, the $\sigma_\perp$ stress is concentrated at the center of the culet. (c) and (f) are maps of the $\sigma_{ZZ}$ stress in the sample chamber.
**Note:** The extracted stress maps neglect the presence of $\sigma_{RZ}$ stress terms. While this is a reasonable assumption at the center of the culet for centrosymmetric systems (yielding the measurements in Fig. 6.4), it may not be accurate for the entire culet (and certainly not in the gasket region). Although a pressure medium may alleviate significant shear stresses in the sample chamber region, the extracted $\sigma_\perp$ and $\sigma_{ZZ}$ values likely represent an upper bound in the absence of any shear stress.

Despite the success of this loading, our story was remarkably overshadowed by one detail I have so far brushed under the rug.

## 6.3 Positive Contrast

In general, cwODMR contrast is 'negative', meaning that the $|S = 1, m_S = \pm 1\rangle$ states are dimmer than the background fluorescence under laser excitation. As mentioned earlier, a

symmetry breaking stress term dresses the $|S = 1, m_S = \pm 1\rangle$ states into symmetric and antisymmetric combinations. These dressed states can have different matrix elements with the $|S = 1, m_S = 0\rangle$ state for a linearly polarized microwave field (commonly realized in experiments). Therefore, in the case of the [100] cut culet, the differential contrast of resonance peaks (Fig. 6.4 (a)) is not immediately surprising. Above 60 GPa pressures, however, we observed a complete inversion of the resonance peak (Fig. 6.6). This unexpected finding of 'positive contrast' underscores how stress can dramatically tune the properties of NV centers (and color centers in general)!

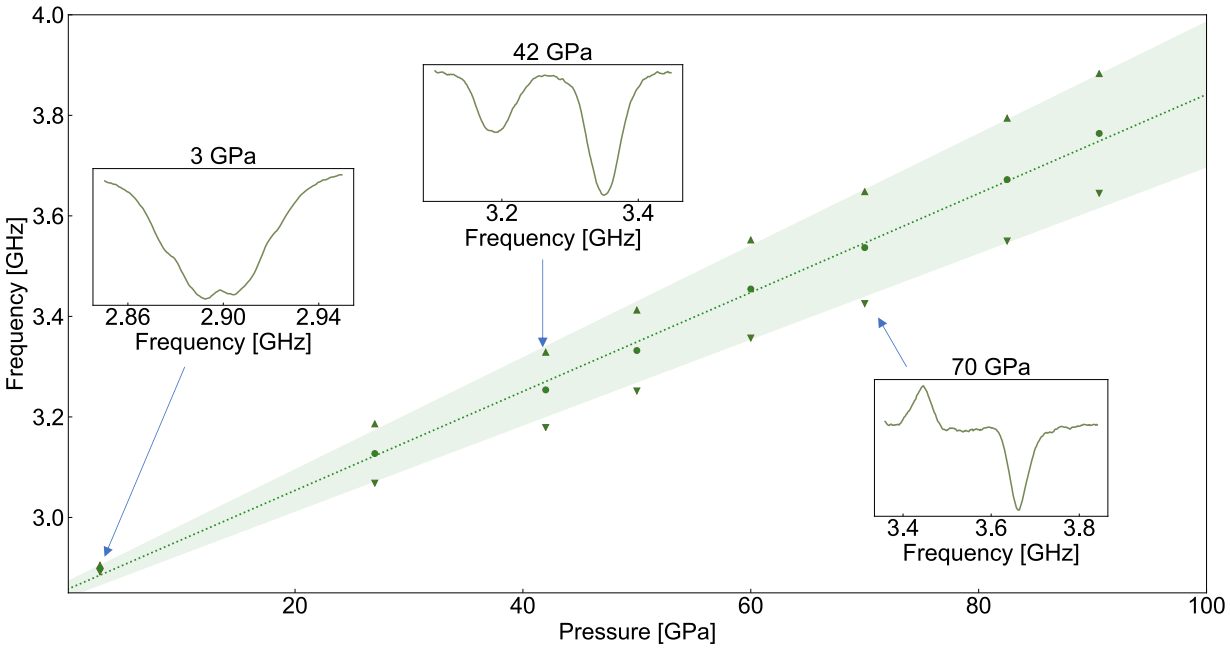


Figure 6.6: **Contrast inversion under pressure:** The shift of the cwODMR resonance (circle) and the center frequency of the two peaks (triangles) is plotted against the ruby/Raman pressure. (Insets) We see a clear shift and splitting of the resonance lines (3 GPa and 42 GPa data points). The differential contrast at 42 GPa is due to the mixing of the $|S = 1, m_S = \pm 1\rangle$ states under a symmetry breaking stress. All points above $\sim 60$ GPa show inverted (positive) for the left resonance (70 GPa data point shown in inset). Despite contrast inversion, the linear trend in the center frequency of both the right and left resonance peaks is maintained up to the highest pressures. Measurements of the stress components $\sigma_{ZZ}$ and $\sigma_{\perp}$ detailed in Fig. 6.4 are based on this data.

The story of positive contrast is a difficult one to ink, primarily because it is unfinished. An undertaking to better understand this phenomenon was deemed orthogonal to our project goals. Although temporarily shelved in my case, someone may take on the mantle of deci-

phering this puzzle in the future. With this in mind, I summarize the data and my thoughts on this topic, hoping to provide some starting ground for the future researcher.

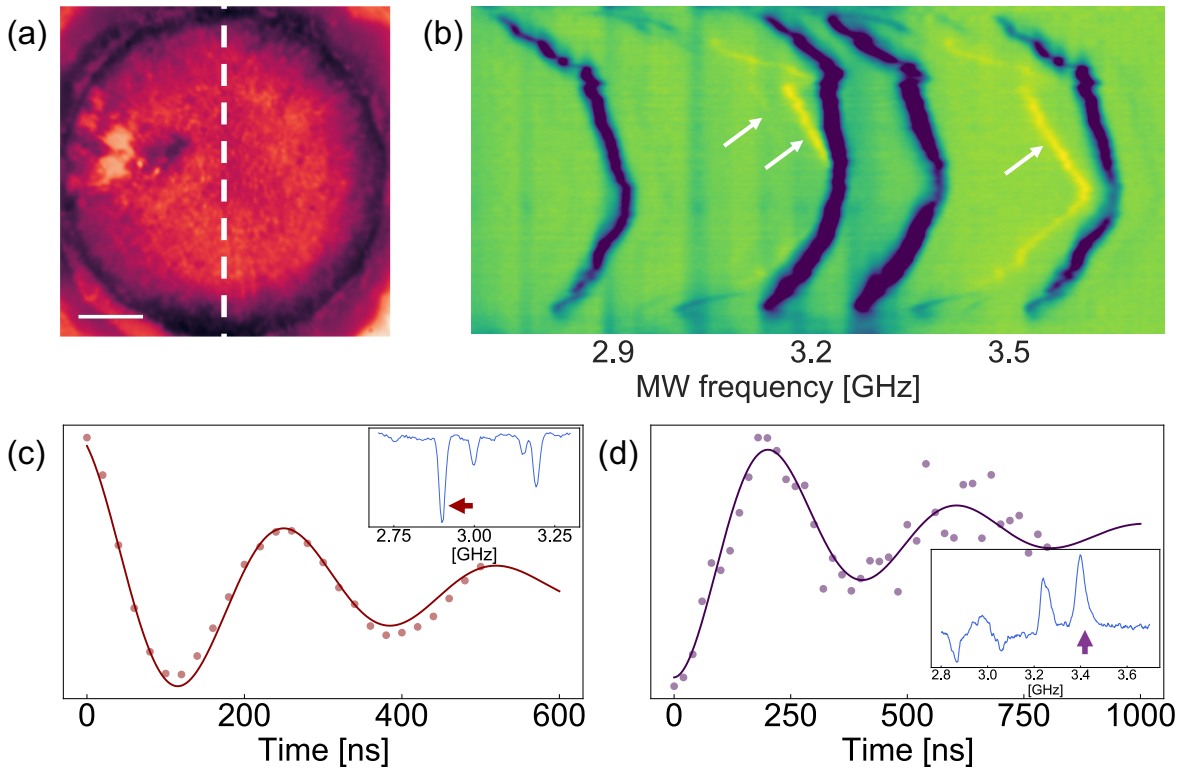


Figure 6.7: **Contrast inversion in [110] cut culets:** (a) . Fluorescence widefield image of a [110] cut culet at ≈ 30 GPa with white scale bar showing 50 µm. The profile of NV resonance for a vertical line cut (broken white line in image) is shown in (b). A cwODMR resonance line (blue) generally has lower fluorescence than the background (green). However, we see three resonance lines with higher fluorescence (yellow) than the background. White arrows point to these positive contrast lines. Rabi measurements on a positive contrast peak (d) show a phase difference of $\pi$ compared to that on a negative contrast peak (c). Insets show cwODMR resonances on which the rabi measurements were performed.
**Note:** Pulsed measurements (c,d) were performed on a separate loading of a [110] cut culet at ≈ 40 GPa. Data in (a,b) taken by Satcher Hsieh.

Contrast inversion was pervasive, being observed in different culet cuts ([100] and [110]) and sample geometries. Pulsed measurements, performed to verify the signal's integrity, showed that the optically pumped state yielded lower fluorescence counts in these regimes (Fig. 6.7). As a rule of thumb, contrast inversion was more pronounced in the gasket region (outside the high pressure sample chamber). Interestingly, even for a [111] cut culet, the

[111] NV group (oriented along the loading axis) showed marked positive contrast in the gasket region. Furthermore, magnetic fields qualitatively changed resonance profiles yielding scenarios where one or both peaks of particular NV groups showed clear positive contrast. Despite these complexities, it is likely that modifications to the intersystem crossing (ISC) mechanism induced by symmetry breaking stress (Fig. 1.4) are responsible for contrast inversion.

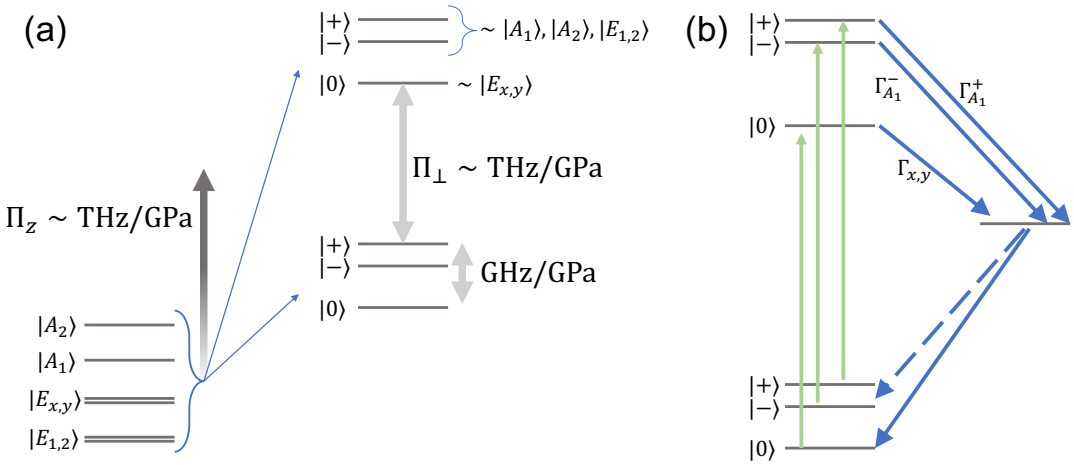


Figure 6.8: **Possible mechanism for positive contrast:** (a) Under stress, the excited state orbitals shifting ($\Pi_z$) and splitting ($\Pi_\perp$) is on the scale of $\sim$ THz/GPa [26]. The stress term dominates the orbital fine structure leading to two orbital branches with spin-1 manifolds in each branch. The spin sub-levels within each branch may be further split (and mixed) by spin-spin and spin-stress coupling terms of the order $\sim$ GHz/GPa (the latter being largely unknown). The interplay of orbital and spin degrees of freedom under stress likely mixes the symmetry-dictated spin states ($|A_1\rangle$, $|A_2\rangle$, $|E_{x,y}\rangle$, $|E_{1,2}\rangle$) that exist under ambient conditions [45]. Consequently, $|\pm\rangle$ spin states in each orbital branch has $|A_1\rangle$, $|A_2\rangle$, and $|E_{1,2}\rangle$ character whereas the $|0\rangle$ spin state has $|E_{x,y}\rangle$ character. (b) Under ambient conditions, spin-orbit coupling mediates the intersystem crossing pathway from the excited $|^3E\rangle$ state to the singlet manifold [45]. The transition is strongest (first order) for the $|A_1\rangle$ state. However, under the influence of stress, modifications to the spin-orbit coupling term may facilitate further transitions terms $\Gamma^+_{A_1}, \Gamma^-_{A_1}$ and $\Gamma_{x,y}$. Speculating that spin-stress coupling terms in the $^3A_2$ and $^3E$ states yield similar spin eigenstates under stress, it is conceivable that electronic excitation will spin conserving. In the regime $\Gamma^-_{A_1} < \Gamma_{x,y} < \Gamma^+_{A_2}$, we are going to get a combination of positive and negative contrast peaks (necessarily assuming that $|^1A_1\rangle \rightarrow |^3A_2\rangle$ transition rates are unaltered under stress). Future experiments may probe aspects of this ISC picture (proposed by Bryce Korbin and Maxwell Block). Current collaborations with Benchen Huang (in the group of Prof. Giulia Galli) aim to understand modifications to the spin-orbit coupling under different stress profiles.

Factors at play in the physics of contrast inversion include:

- **Stress induced perturbations to spin-orbit coupling:** The upper branch of the ISC ($^3E \rightarrow {}^1A_1$ in Fig. 1.4) is understood to be driven by spin-orbit coupling [73]. The $|^3E, m_S = 0\rangle$ state is not coupled to the singlet manifold under this mechanism. However, perturbations to the spin-orbit coupling term under stress may lead to transitions from the $|^3E, m_S = 0\rangle$ spin states to the singlet manifold, resulting in diminishing fluorescence.
- **Spin-stress coupling in the $^3E$ excited state:** The observation of changes in contrast under the application of magnetic fields underpins the role of spin. The orbitally averaged zero-field splitting of the NV spin in the excited electronic state is measured to be $\sim (2\pi) \times 1.42\,\text{GHz}$ [40]. However, significant changes to the orbital energies due to stress ($\sim$ THz/GPa) may invalidate our present model of orbital averaging in the excited state [85]. The spin-stress coupling in the excited state is poorly understood and could be diagnosed further through quantitative contrast measurements.

An empirical understanding of the interplay between stress and magnetic fields in the determination of positive contrast is a crucial next step in solving this puzzle. However, our progress in this direction was serendipitously cut short. In the effort to understand the ISC mechanism, our exploration of published literature uncovered a neat solution to the problem of NV sensing at extreme pressures.

## 6.4 The home run...

In our search to understand the goings on of contrast inversion, we came across previous work by Goldman *et al.* [45, 44] on the intersystem crossing (ISC) mechanism (Fig. 1.4). Specifically, they modeled the upper branch of the ISC ($|^3E\rangle \rightarrow |^1A_1\rangle$) mediated by spin-orbit coupling in the NV center. Resting on the idea that ISC dynamics were driven by electron-phonon coupling, they hypothesized that the transition rate from the $|^3E\rangle$ to the singlet $|^1A_1\rangle$ state would "effectively" depend on the energy difference between these two levels ($\Delta$ in Fig. 6.9 (b)). Learning about their findings was a significant turning point in our project. Taking this model to be right in spirit, we now interpreted the loss of contrast in hydrostatic and [100] stress conditions due to the increase in $\Delta$ and a consequent reduction in the ISC transition rate. Crucially, a stress profile that could reduce $\Delta$ would retain (if not enhance) cwODMR contrast up to the highest pressures (Fig. 6.9).

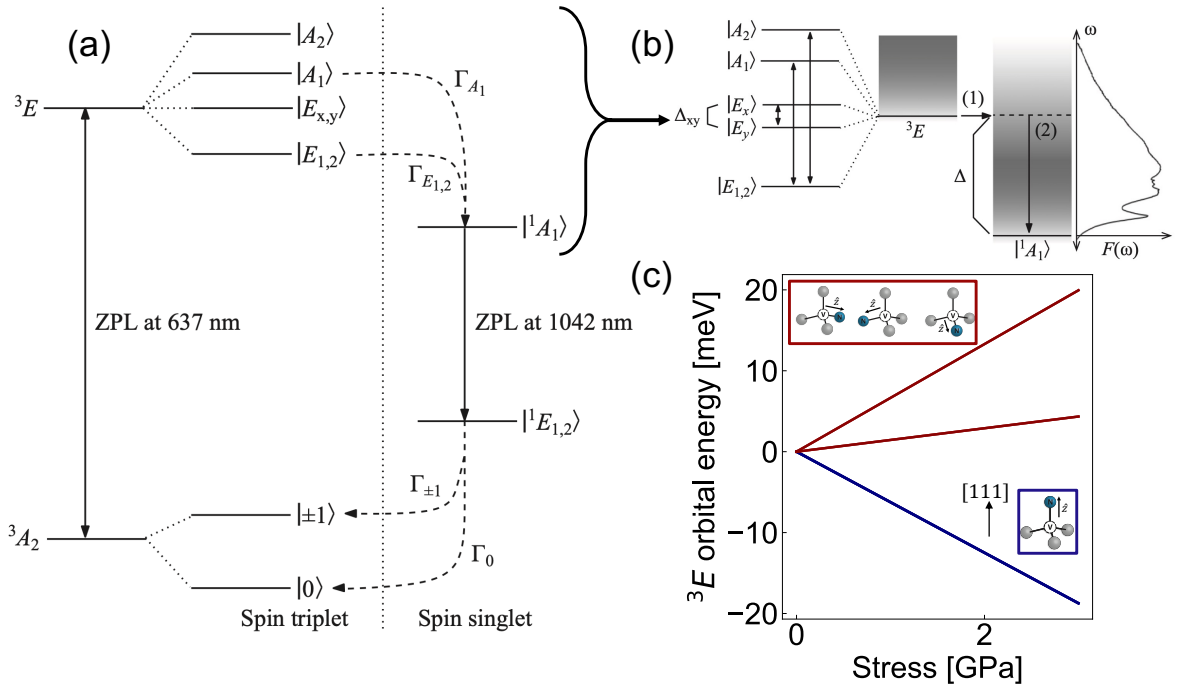


Figure 6.9: **Contrast, Stress, and the intersystem crossing:** (a) A detailed schematic of the intersystem crossing (ISC) reproduced from [45]. $\Gamma_{A_1}$ and $\Gamma_{E_{1,2}}$ represent the transition rates from the sublevels of the $^3E$ excited state to the $|^1A_1\rangle$ singlet state. Goldman *et al.* modeled the former transition ($|A_1\rangle \rightarrow |^1A_1\rangle$) as a first-order process driven by spin-orbit coupling. The latter transition occurs at second order due to the electron-phonon mixing within the $^3E$ manifold and subsequent spin-orbit transition to the $|^1A_1\rangle$ state. (b) The channel to the singlet state was modeled as a resonant transition from the $^3E$ manifold to the phononic excitations of the $|^1A_1\rangle$ state. The transition rate depends on the density of phononic excitation states $\rho(\Delta)$ resonant with the $^3E$ manifold (shown here as a vibrational overlap function $F(\omega)$ computed using the optical spectrum of the $|^3E\rangle \rightarrow |^3A_2\rangle$ emission). A decrease in $\Delta$ increases the density of states on resonance and enhances the ISC transition. (c) Studies by Davies and Hammer [26] show that stress along the [111] crystal axis reduces the energy of the $^3E$ orbital for one of the NV groups (blue), likely decreasing $\Delta$ in the ISC channel shown in (b). Based on the ISC picture, this NV group may show contrast retention at the highest pressures.
**Note:** Image (a) and (b) are reproduced from [45].

One of the earliest publications on the NV center (predating its identification) carefully measured its optical properties under different stress conditions [26]. In this work, Davies and Hammer discovered that for a [111] stress profile, the electronic excited state $|^3E\rangle$ red shifted towards the ground $|^3A_2\rangle$ state (Fig. 6.9 (c)) for the NV group oriented along the

[111] axis. Since the singlet state is built out of the same $|e_{x,y}\rangle$ orbitals as the triplet ground state, this closing of the gap between the energies of the $|a_1'\rangle$ orbitals and the $|e_{x,y}\rangle$ orbitals suggested that $\Delta$ would decrease under a [111] stress. Furthermore, for the [111] NV group, it was unlikely that a symmetry-preserving [111] stress would give rise to any contrast inversion effects. At long last, we had a possible solution to NV sensing up to megabar pressures.

Remarkably, the feasibility of this technique was undoubtedly verified on our first attempt to test this idea with a [111] cut anvil (Fig. 6.10). More recent studies at pressures nearing $\sim 150\,\text{GPa}$ have achieved DC sensitivity of $\approx 50\,\mu\text{T}/\sqrt{\text{Hz}}$ and pulsed measurements with Rabi frequencies $\Omega \gtrsim (2\pi) \times 5\,\text{MHz}$ (Fig. 1.7).

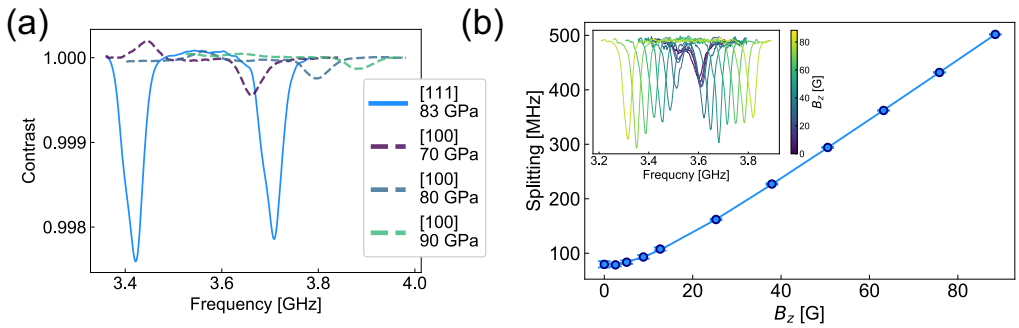


Figure 6.10: **NV sensing up to megabar pressures using [111] cut anvils:** (a) A comparison of cwODMR contrast for [111] cut culet at $\sim 80\,\text{GPa}$ with that for [100] cut culet at the same pressure range shows clear contrast retention in the former case. (b) Applying an axial magnetic field ($B_Z$) in a [111] cut culet shows a clear evolution of the Zeeman splitting in the [111] NV group verifying the integrity of our high-pressure signal. A low fields, the splitting due to symmetry breaking stress adds in quadrature with the Zeeman splitting, giving a total splitting of $\Delta\nu = \sqrt{(2E)^2 + (2\gamma B_Z)^2}$. At large fields, the splitting due to the magnetic field dominates and grows linearly. The inset shows the cwODMR spectra for this data set. cwODMR and pulsed measurements at $\sim 120\,\text{GPa}$ for a [111] cut culet are shown in Fig. 1.7.

## 6.5 The road ahead...

Despite the success of our efforts in pushing NV sensing to megabar pressures, many open questions remain. Most importantly, a physical picture of the electronic excited state under stress and magnetic field that leads to contrast inversion still needs to be completed. Nevertheless, based on our understanding of the ISC model proposed by Goldman *et al.* [45], a few comments are in order concerning the advantages of different culet cuts for sensing stress and magnetic fields under pressure.

- **[100] cut culet**: Under uniaxial [100] stress, the electronic excited state splits as shown in Fig. 6.11 (a). While this can lead to reduction and inversion of contrast, the degeneracy of the four NV groups under stress can simplify the interpretation of the cwODMR spectrum. In this case, a direct measurement of the $\{\sigma_{ZZ}, \sigma_{\perp}\}$ stress components provides a clean technique for pressure calibration. This can be advantageous for experiments up to $\sim 50\,\mathrm{GPa}$, where a thorough measurement of the full stress tensor using carefully applied magnetic fields is unnecessary.

- **[110] cut culet**: In the case of uniaxial [110] stress, there are two sets of doubly degenerate NV groups. Although the stress breaks the symmetry for both sets, their behaviors are dramatically different. For two NV groups with their $\hat{z}$ axes lying in the plane of the culet, the stress is wholly transverse (shown in red in Fig. 6.11 (b)). In this set of NV groups, both branches of the $^3E$ excited state orbitals are blue shifted (suggesting an increase in $\Delta$ in Fig. 6.9 (b)) and a consequent loss in contrast. However, for the other set, comprising two NV groups with their $\hat{z}$ axes lying in the plane perpendicular to the culet, the $^3E$ excited state orbitals are red-shifted (suggesting retention of contrast to higher pressures). Our measurements are consistent with this picture; wherein at high pressures ($\gtrsim 30\,\mathrm{GPa}$), we see nearly degenerate resonances stemming from two NV groups (ostensibly from the second set). This ability to measure four numbers (shift and splitting of two NV groups) with better SNR than in [100] cut culets affords the ability to perform vector magnetometry at high pressures. In addition, with a little work and knowledge of the orientation of the NV groups relative to the lab frame, it may also be feasible to extract all three diagonal stress components and some measure of the shear stress in the culet.

- **[111] cut culet:** The 'winning strategy' for sensing up to the highest pressures (see Fig. 1.7) comes at the cost of sacrificing signals from the remaining three NV groups that are not oriented along the loading axis. With our ability to measure just two numbers (shift and splitting of the [111] NV group), it is only possible to get an estimate of the combined symmetry-preserving stresses $(\sigma_{ZZ}, \sigma_{\perp})$ and symmetry breaking stresses $(\sigma_{XX} - \sigma_{YY}, \sigma_{XZ}, \sigma_{YZ}, \sigma_{XY})$. As detailed in the previous chapter, further assumptions must be made about the nature of the stress depending on the details of the experiment. In the case of magnetometry, it will only be possible to measure the axial and transverse components of the magnetic field $(B_Z, B_{\perp})$. The latter component is suppressed by the zero-field splitting $D_{gs}$ and the magnitude of the symmetry-preserving stress. Nevertheless, for most of the experiments at megabar pressures, this may be a sufficient means of probing both magnetism and stress.

In summary, there is much opportunity for further work in high-pressure sensing based on NV centers (and more broadly using color centers) [48]. NV sensing up to megabar pressures enables studies of crystal stress for different culet cuts and pressure media on the one hand, and measurements of magnetism in various condensed matter systems on the other. The ability to do pulsed measurements up to these pressures lends access to the vast array of

quantum sensing protocols demonstrated hitherto at ambient pressures. It will be exciting to see further applications of this work!

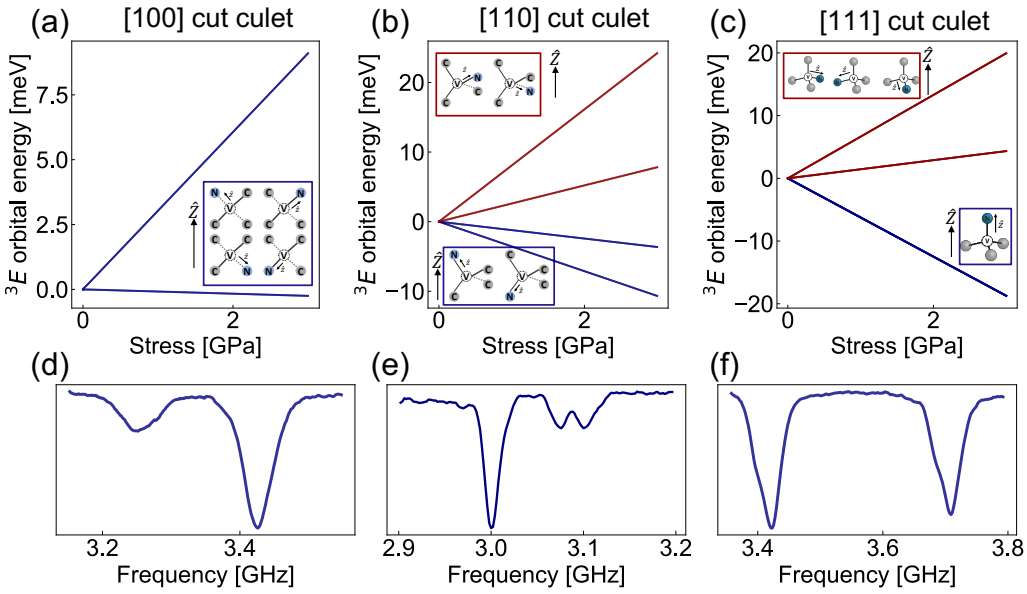


Figure 6.11: **A comparison of culet cuts for high-pressure sensing:** (a-c) Based on measurements by Davies and Hammer [26], we can predict the splitting and shifting of $^3E$ orbitals of the NV center for different stress profiles (Insets show the orientation of different NV groups relative to the loading axis $\hat{Z}$). (a) A [100] uniaxial stress projects equally on all four NV groups. (b) A [110] uniaxial stress gives two sets of doubly degenerate NV groups. For groups in the culet plane (red), the $^3E$ orbitals are blue-shifted to higher energies. In contrast, for NV groups in the plane perpendicular to the culet (blue), the $^3E$ orbitals are red-shifted to lower energies. In the former case, we expect a reduction in the ISC rate and consequent loss of contrast. In the latter case, we expect some contrast retention up to high pressures. (c) For a [111] cut culet, the symmetry is preserved for one of the NV groups (blue), and the orbital energies are red-shifted. Increase in orbital energies for the other three groups (red) leads to a loss of contrast. (d-f) cwODMR spectra for different stress profiles. (d) In the [100] case, all groups are degenerate, showing a shift and a splitting due to stress. (e) cwODMR spectrum at $\sim 40$ GPa for a [110] cut culet shows resonances from two nearly degenerate NV groups. An applied magnetic field often shows four clear resonances (see Fig. 6.7), possibly belonging to the NV groups oriented in the plane perpendicular to the culet. (f) For a [111] cut culet, the resonance of the [111] NV group survives above megabar pressures.

**Note:** The spectrum in (f) was taken with an applied $\vec{B}$ field. The spectra in (d,e) were taken with zero background field.

# Chapter 7

# Imaging magnetism in hydride superconductors at megabar pressures

At a high level, the two hallmarks of superconductivity are:

- a sharp drop in the sample resistance to $R = 0$ on cooling below a critical temperature
- the expulsion of any applied magnetic field ($\vec{H}$) from the bulk (Meissner effect)

These remarkable properties are engendered by a phase transformation wherein electrons at the Fermi surface of the material form bound (Cooper) pairs [101].

At a macroscopic level, there are two intrinsic length scales in this problem [101]. The coherence length ($\xi$) provides a scaling for the size of the cooper pairs. The penetration depth ($\lambda$) defines the characteristic scale over which an external magnetic field decays within the superconductor. Within the Ginzburg-Landau (GL) theory framework, the relationship between these lengths scales ($\kappa = \lambda/\xi$) determines the macroscopic behavior of superconducting samples. In the case of type I superconductors ($\kappa < 1/\sqrt{2}$), magnetic fields do not permeate the bulk sample in the superconducting state [101]. Intercalating regions of superconducting and normal phases can exist in the intermediate state, but the applied field is still fully expelled from the interior of the superconducting regions. For type I materials, superconductivity is destroyed when applied magnetic fields surpass the critical field ($H_C(T)$). For type II superconductors ($\kappa > 1/\sqrt{2}$), qualitatively different features emerge in the presence of magnetic fields. In these materials, there are two critical field parameters. For $H < H_{C_1}(T)$, these samples show the characteristic Meissner effect (similar to type I materials). For $H > H_{C_2}(T)$, superconductivity is destroyed, and the sample reverts to the normal state. Interestingly, for $H_{C_1}(T) < H < H_{C_2}(T)$, these materials exhibit the mixed state wherein the applied field permeates the bulk superconductor in the form of vortices [101].

At a microscopic level, the physics of the pairing mechanism distinguishes between conventional and unconventional superconductors. In conventional (or BCS superconductors), electron pairing can be understood within the framework of BCS (Bardeen-Cooper-Schrieffer)

theory [101]. In contrast, the microscopic pairing mechanism for unconventional superconductors is a longstanding open problem in physics. Elemental superconductors are BCS superconductors, whereas high $T_C$ materials are unconventional superconductors. This simplistic classification belies the myriad ways superconducting behavior is subject to sample quality (i.e., disorder) and geometry.

The proposal and observation of superconductivity in high pressure hydrides naturally invokes two crucial scientific questions. First, it is imperative to determine the type of superconductivity in these materials and map out the $BT$ phase diagram. Second, despite modeling these materials as BCS superconductors, it is essential to verify the signatures of BCS pairing. However, at a more fundamental level, it is necessary to incontrovertibly establish whether these materials are indeed superconductors by *simultaneously* measuring transport and magnetism [47].

Surveying the landscape of the proliferating work on so-called 'superhydrides' [81, 89, 109], numerous studies have already noted a sharp drop in sample resistance in several such materials. In comparison, studies detailing the magnetic behavior are markedly fewer [34, 50, 97, 102]. This is because the application of megabar pressures constrains sample size (order $\sim 10\,\mu\text{m}$) and generates enormous pressure gradients, complicating the subtraction of background signals [34, 97]. Additionally, the standard synthesis technique involving laser-heating results in complex spatial geometries precluding a thorough understanding of sample inhomogeneities [97]. We combat some of these issues using the NV sensing platform. Specifically, performing *in situ* magnetometry in the proximity of the sample obviates the need for background subtraction. Furthermore, fabricating of shallow layer ($\sim 50\,\text{nm}$) of NV centers at culet surface avoids averaging over the exorbitant stress gradients through the diamond. Finally, spatially resolved measurements with sub-micron resolution allow us to observe inhomogeneities in sample response directly.

The promising first loading with a [111] cut culet gave us confidence in our approach (Fig. 6.10). We cast our net in the hunt for a hydride superconductor that fit our experimental constraints. Initially, we were restricted to using flat culet because it was impossible to source beveled diamonds with [111] crystal cut (limiting us to pressures $\lesssim 100\,\text{GPa}$). Furthermore, we were more interested in looking at materials with $T_C \approx 100\,\text{K}$ (or higher) because of the persistent challenges of cooling a DAC with a large thermal mass. Prof. Viktor Struzhkin suggested we look at Cerium Hydride [21] and referred us to Prof. Xiaoli Huang and Wuhao Chen. Transport measurements on Cerium Hydride loadings suggested the possibility of realizing two main hydride complexes under pressure:

- the $Fm\bar{3}m$-$CeH_{10}$ phase showed a $T_C = 115\,\text{K}$ at pressures of $\sim$95 GPa
- the $P6_3/mmc$-$CeH_9$ phase showed a $T_C = 57\,\text{K}$ at pressures of $\sim 88\,\text{GPa}$ with $T_C$ increasing to 100 K at 130 GPa on further compression

In all respects, it was the ideal compound for our study.

As a beginning graduate student, my first meeting with Norm involved a fleeting mention of developing a platform to study magnetism in hydride superconductors [34]. At long last, we were ready to set out on that road.

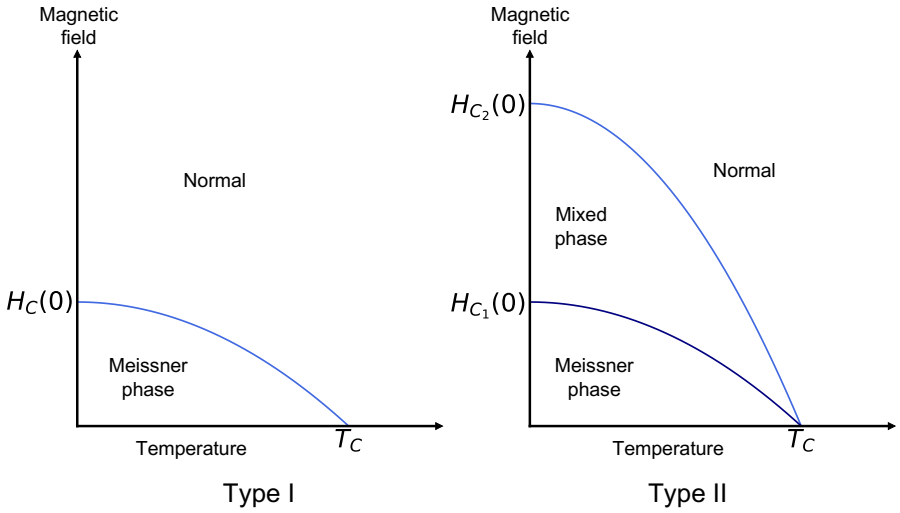


Figure 7.1: **Phase diagram of type I and type II superconductors:** Type I superconductors (left) expel magnetic fields from the sample interior (Meissner phase). Applying fields larger than $H_C(T)$ destroys superconductivity in the material. In contrast, type II superconductors (right) have two critical fields. Below $H_{C_1}(T)$, these materials are in the Meissner phase showing complete field expulsion in the bulk. However, for $H_{C_1}(T) < H < H_{C_2}(T)$, these materials exhibit field penetration through the bulk sample in the form of vortices (mixed phase). Type II materials can remain superconducting up to much higher fields of $H_{C_2}(T)$.

**Note:** Superhydrides are believed to be type II superconductors because transport measurements show consistent resistance drops at high fields of $1 - 10$T (suggesting typical upper critical field values $H_{C_2}(0) \gtrsim 20\,\mathrm{T}$) [21]. In the remainder of the chapter, I will use the phase diagram of type II materials when explicating the studies of magnetism.

**Note:** I am actively undertaking the study at the time of writing this thesis. While my description may meander from observational to speculative, I aim for completeness with the hope that any mistakes here will be corrected in our publication (also in preparation).

## 7.1 Sample preparation

A 23 mm miniature panoramic DAC [41] was used for all loadings. For NV measurements, we sourced type Ib anvils with [111] crystal cut culet (from SYTNEK Corp. and Almax

easylab) with culet diameters of 100 µm beveled at 8.5° up to 300 µm. The anvils were implanted with $^{12}C^{+}$ ions and annealed to create a layer of NV ensembles 50 nm from the surface following the description in Section 1.1. The type Ib anvils were glued to the cylinder side of the DAC. The opposing (piston) anvils were [100] crystal cut type Ia diamonds with the same culet design. Four Molybdenum (Mo) leads were sputtered on the anvil to perform transport measurements (Fig. 7.2 (a)). A Pt wire on the cylinder side was used to deliver microwaves for NV studies.

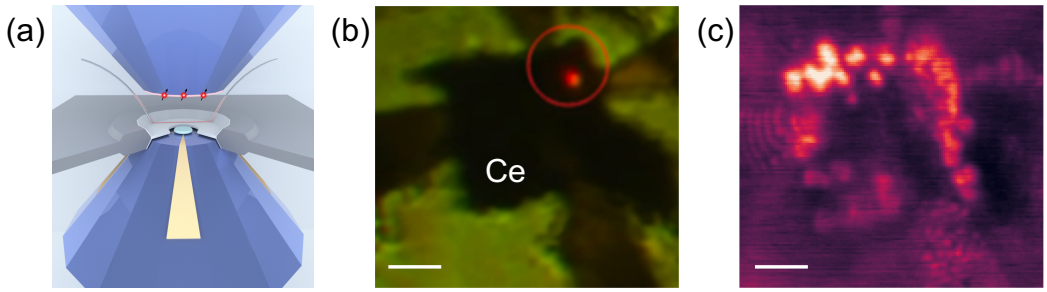


Figure 7.2: **Loading and sample synthesis:** (a) A schematic of the sample showing type Ib anvil with NV centers (above), a Pt wire, and the opposing type Ia anvil (below) with transport leads. The Ce metal sample was positioned to make electrical contact with the leads. An insulating gasket using Calcium Fluoride ($CaF_2$) was fashioned out of a rhenium foil. The sample chamber was filled with Ammonia Borane ($NH_3BH_3$). (b) An optical image showing the Ce sample and transport leads. The sample was heated by rastering a 10 W laser (red spot) to induce the decomposition of Ammonia Borane. The emitted hydrogen can combine with the sample to form hydrides. (c) Confocal fluorescence scan taken after laser heating over the same sample region as (b). Interference fringes show the four transport leads in the corners of the sample. Distinct bright regions around the sample show markedly higher fluorescence suggesting the creation of NV centers due to laser heating. In (b) and (c), white scale bars denote 10 µm.

Wuhao Chen synthesized the sample at Jilin university following the procedure in [21]. An insulating gasket (using Calcium Fluoride as insulation) was fashioned out of rhenium foil to compress a Cerium (Ce) sample and powdered Ammonia Borane ($NH_3BH_3$). The sample was compressed to $\sim$ 130 GPa pressures and laser heated to induce the decomposition of the Ammonia Borane into cubic boron nitride and hydrogen ($NH_3BH_3 \rightarrow cBN + 3H_2$). The reaction between hydrogen and Ce metal yields a complex of Cerium hydrides. The formation of one of the target compounds ($CeH_9$) was verified through transport measurements (Fig. 7.3 (b)).

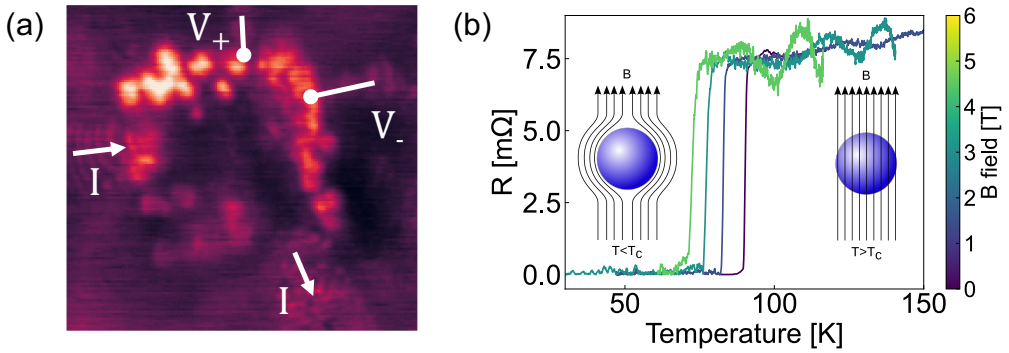


Figure 7.3: **Verification of sample synthesis using transport:** (a) Fluorescence scan of the sample showing leads used for current flow and voltage pickup. (b) Transport measurements performed using the delta technique at Jilin University (by Wuhao Chen). The sample shows a clear drop in resistance at $\sim 90\,\mathrm{K}$. Application of $\sim 1\,\mathrm{T}$ scale magnetic fields suppresses $T_C$, suggesting superconducting behavior. The noise source in the high field measurements is not completely understood (likely due to inductive pickup or hall currents). (Inset) Illustrations show the projected magnetic response of the sample to applied magnetic fields in the normal state (right) and superconducting state (left) (images sourced from [24]). The sample expels the applied field from the interior in the Meissner phase (left).

### Laser heating and NV creation

In addition to the shallow layer of NV ensembles fabricated on the anvil, the focusing of a high-power laser beam for sample synthesis serendipitously created more NV centers at the culet [19]. Although it was non-trivial to determine the exact depth and distribution of the NV centers created through the laser heating process, this high density region showed better fluorescence and contrast properties. In addition, the potential proximity of these centers to the target hydride compound allowed for greater signal strengths. Fig. 7.4 (c) compares the cwODMR spectrum of NV centers in the two regions.

Large shear stresses (on the order of $\sim 10\,\mathrm{GPa}$) and gradients thereof are expected due to contact between Ce metal and the culet surface at megabar pressures. The shear stress manifests as a splitting ($\gtrsim 100\,\mathrm{MHz}$) in the cwODMR spectrum. However, NV centers in the laser heated regions showed markedly smaller splittings, likely due to local stress relaxation at high temperatures ($\gtrsim 1000\,\mathrm{K}$). This was also advantageous for magnetic sensing because symmetry-breaking stress and magnetic field terms in the NV Hamiltonian (Eq. 3.1) do not commute.

**Note:** We studied two samples prepared in this manner. For the second sample, thermal cycling in the cryostat caused the diamonds to fail before all magnetic studies could be completed. Nevertheless, the magnetic behaviors of both samples were qualitatively similar.

For clarity, I will primarily focus on the first sample, which was studied in greater detail. Where appropriate, I may include supporting data from the second sample. Sample 1 was at pressures $\approx 130-140$ GPa while sample 2 was at pressures $\approx 120-130$ GPa (determined from culet Raman [3] and NV measurements) .

**Note:** Due to the nature of the synthesis technique, the target superconducting compound is not uniformly distributed across the sample. A good fraction of the laser heated regions did not show clear magnetic signatures of superconductivity, suggesting that sample synthesis is stochastic.

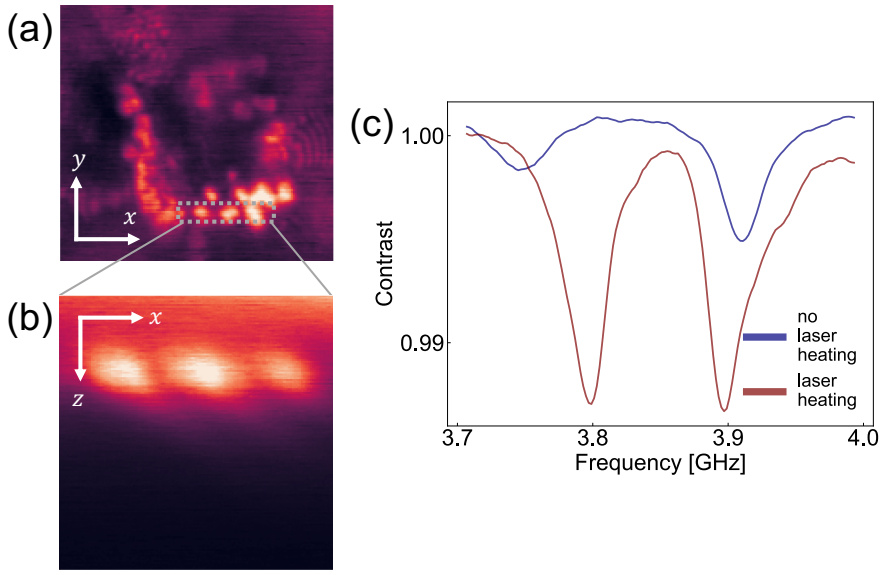


Figure 7.4: **NV creation through laser heating:** (a) Confocal fluorescence scan of the sample. (b) A cut along the $xz$ plane across laser heated points (grey box) shows dense pockets of NV centers. (c) NV centers in the laser heated regions show markedly higher contrast. Furthermore, the stress splitting ($2E = 2\sqrt{E_x^2 + E_y^2}$) is lower in these regions, likely due to local stress relaxation on laser heating.

## 7.2 Experimental setup

All measurements were performed on a confocal fluorescence microscope integrated with a closed cycle Helium cryostat (Attocube attoDRY800). The details of the confocal assembly are already provided in Fig. 1.5. Magnetic fields were applied along the loading axis ($\hat{z}$ for the [111] NV group) using a custom-built electromagnet (Woodruff Scientific) assembled outside the vacuum shield of the cryostat (Fig. 7.5 (a)).

**Note:** In the remainder of this chapter, I will exclusively consider the [111] NV group. As

such, any mention of NV splitting will refer to this group of NV centers only. In this case, the lab frame $\{\hat{X}, \hat{Y}, \hat{Z}\}$ coincides with the NV frame $\{\hat{x}, \hat{y}, \hat{z}\}$.

## Field calibration

Due to small changes in the coil placement between cooldowns, we regularly calibrated the magnetic field from the electromagnet (Fig. 7.5 (a)). Field calibration was performed by measuring the splitting of the culet NV centers for different currents applied to the electromagnet. The Hamiltonian for the NV center is given by

$$H = \left(D_{gs} + D(\overleftrightarrow{\sigma})\right) S_z^2 + E(\overleftrightarrow{\sigma})(S_x^2 - S_y^2) + \gamma \vec{B} \cdot \vec{S} \tag{7.1}$$

where $D_{gs} = (2\pi) \times 2.87\,\text{GHz}$ is the zero-field splitting and $\gamma = (2\pi) \times 2.8\,\text{MHz/G}$ is the gyromagnetic ratio. As mentioned earlier (Section 3.1), the symmetry preserving stress parameter manifests as a shift $D(\overleftrightarrow{\sigma})$ in the cwODMR spectrum whereas the symmetry breaking stress splits the $|m_S = \pm 1\rangle$ states by $2E(\overleftrightarrow{\sigma})$ and mixes them into $|\pm\rangle = (|m_S = +1\rangle \pm e^{i\phi_E} |m_S = -1\rangle)/\sqrt{2}$.

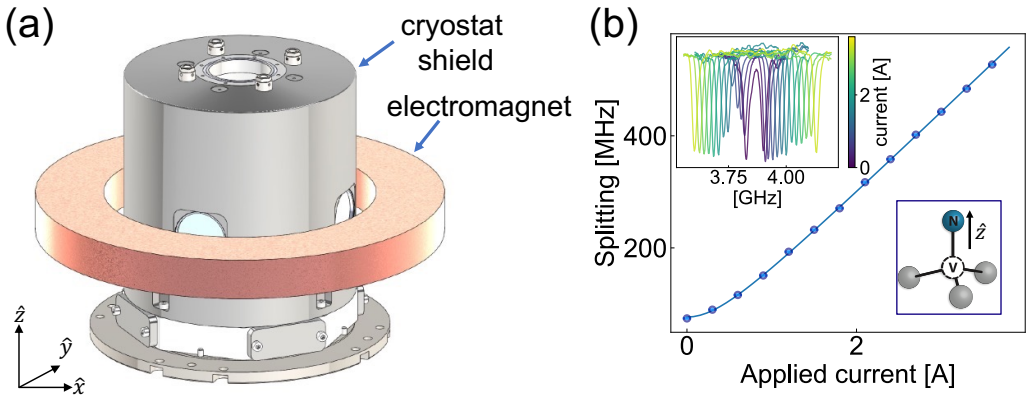


Figure 7.5: **Calibrating magnetic fields:** (a) Schematic of the experimental apparatus showing the vacuum shield of the cryostat and the electromagnet. The electromagnet is coaxial with the cryostat and the DAC, with the dominant field component along the $\hat{z}$ axis. The applied field aligns with the quantization axis of the [111] NV group. (b) Calibration of the magnetic field, performed at the start of every cooldown, involved studying the cwODMR splitting as a function of the applied current (inset shows the measured cwODMR spectra). The Zeeman splitting due to the magnetic field ($B_z$) adds in quadrature with the splitting due to the symmetry breaking stress ($2E$), giving a hyperbolic profile ($\Delta\nu = \sqrt{(2E)^2 + (2\gamma B_z)^2}$). The measured splitting shows excellent agreement with the model with comparable $B_z/I$ values at several points on the culet.

**Note:** The eigenstates are determined by the ratio of $E_x$ and $E_y$ stress terms (i.e., $\phi_E = \arctan(E_y/E_x)$). However, for this project, it is sufficient to consider the overall symmetry breaking stress parameter $E = \sqrt{E_x^2 + E_y^2}$.

Applying a magnetic field along the quantization axis of the NV center ($\hat{z}$) competes with the symmetry breaking stress. The total splitting ($\Delta\nu$) can therefore, be expressed as

$$\Delta\nu = \sqrt{(2E)^2 + (2\gamma B_z)^2} \tag{7.2}$$

Neglecting the magnetic response in the sample, the effective magnetic field is directly proportional to the current applied in the electromagnet ($B_z \propto I$). Measuring this splitting as a function of this current, therefore, serves as a calibration of the $B_z$ field experienced at the culet (Fig. 7.5 (b)).

**Note:** First, any small transverse magnetic field component ($B_\perp$) manifests in second order and is further suppressed by the dominant axial ($B_z$) field (in addition to the zero field splitting and symmetry preserving stress terms). Second, due to the separation of scales between the culet size ($\approx 100\,\mu\text{m}$) and the dimensions of the magnet ($\approx 50\,\text{cm}$), the applied field is uniform over the sample region to a good approximation. We verify this directly by performing field calibration at several spatial points in the sample region. Third, placing the electromagnet outside the cryostat ensures that this field calibration is independent of the sample temperature. We verify this by performing field calibration at several sample temperatures far above the superconducting transition ($T \gg T_C$). Finally, we can control for local changes due to parasitic paramagnetism by probing different spatial points. Our measurements verify that sample paramagnetism is neglible.

**Note:** In the following sections, I will be careful about the notation between the field generated by the electromagnet (Fig. 7.5 (a)) and the field measured by the NV center (Eq. 7.2). The former (referred to as $\vec{H}$) constitutes a uniform background field. The latter (referred to as $\vec{B}$) is the sum of the uniform background field ($\vec{H}$) and the local perturbations due to the magnetic response of the sample ($\vec{M}$). In the normal state ($T > T_C$), we neglect the sample's magnetization ($\vec{M} \approx 0$). Therefore, the field measured by the NV center everywhere in the sample region is equal to the background field ($\vec{B} = \vec{H}$). This is also true for $T < T_C$ in spatial regions of the sample without any superconducting material (see Fig. 7.7 (c)). However, for specific regions in the sample where the target superconducting compound is present, the local magnetic field measured by the NV centers ($\vec{B}$) will be markedly different from the background field ($\vec{H}$).

## Sample thermalization and cooling

Sample thermalization at cryogenic temperatures proved an important consideration in the experiments. Indeed many initial cooldowns yielded null results because of poor sample thermalization. This can be attributed to several factors:

- Large thermal mass of the DAC body

- Poor thermal contact between the DAC body and the cold finger
- Diminishing phonon mediated thermal conductivity in diamond at cryogenic temperatures ($\lesssim 100\,\mathrm{K}$) [14]

A combination of thermal links was used to ensure better sample cooling. The first link (custom fabricated by Four Nine Design) was strapped to the cell body at one end and the cold finger of the cryostat on the other (Fig. 7.6 (a)). The second link, cut out of Indium (In) foil, was attached between the gasket and the DAC body (Fig. 7.6 (b)) to mitigate the diminishing thermal conductivity of the diamond below 100 K.

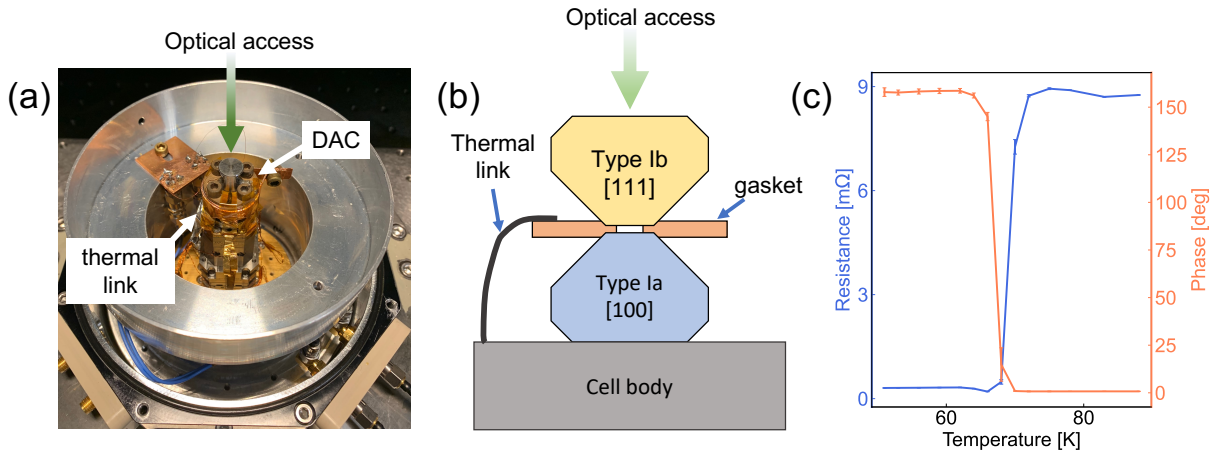


Figure 7.6: **Thermal linking:** (a) A custom thermal link (Four Nine Design) between the cell body and the cold finger of the cryostat allowed for better thermalization. The thermal link was secured to the cell body using a girdle machined out of a copper plate. (b) A second thermal link was attached between the metal gasket and the cell body to account for the diminishing thermal conductivity of diamond below 100 K. The link was cut out from Indium (In) foil and attached at either end by cryogenic epoxy (Stycast® 2850FT). (c) Lock-in measurements show a drop in sample resistance at $\sim 70\,\mathrm{K}$ at zero applied magnetic field. This resistance drop is accompanied by a jump in the measured phase from 0° to $\sim 150°$ deep in the superconducting state. The transition point is $\sim 20\,\mathrm{K}$ lower than the true $T_C$ of the sample due to the thermal gradient between the cold finger (location of temperature reading) and the high pressure sample.

Despite extensive thermal linking, we observed a temperature gradient of $\sim 20\,\mathrm{K}$ between the temperature reading at the cold finger and the high pressure sample. Independent transport measurements in a different cryostat with better sample thermalization were used to ascertain the true transition temperature of the sample (Fig. 7.3).

### Lock in transport measurements

Simultaneous transport and NV measurements require careful sample loading to ensure no electrical contact between the transport leads, MW wire, and gasket. In conjunction with NV magnetometry, sample resistance was monitored using lock-in measurements. A Zurich instruments MLFI (DC-500 kHz) lock-in amplifier was used to drive a voltage-controlled current source (Stanford Research Systems CS580). We performed lock-in measurements at 17.7 Hz using the leads shown in Fig. 7.3 for current flow and voltage pickup. The amplitude signal of the lock-in measurements showed a clear drop in sample resistance, and the phase signal concurrently showed a marked deviation from purely resistive behavior. This transition of the sample was observed near 70 K ($\sim$ 20 K below true $T_C$) due to the temperature gradient between the cold finger and the high pressure sample (Fig. 7.6 (c)).

## 7.3 Magnetism in a hydride superconductor

One of the necessary signatures of superconductivity is the expulsion of magnetic flux from the bulk (Meissner effect). Despite this apparent simplicity, the interplay of sample geometry and disorder in real materials gives rise to an array of qualitatively behaviors [77, 71]. There are several standard protocols for tackling the various questions on the nature and type of superconductivity. These approaches aim to study the material's behavior in the superconducting state when taking different paths in $H\,T$ phase space.

### Zero field cooling: Meissner effect

In the first study, we cooled below $T_C$ without any applied field ($\vec{H} = 0$). Following this zero-field cooling (ZFC) deep into the superconducting phase, we applied a uniform background field ($H_z$) and studied the magnetic response of the sample. Near the superconductor, we expect a local variation in the $\vec{B}$ field (here, $\vec{B} = \vec{H} + 4\pi\vec{M}$ is the magnetic flux density that determines the NV splitting). In particular, on top of the superconductor, we expect $B < H$ indicative of Meissner suppression. In contrast, parts of the sample region without target hydride compound should yield NV splitting consistent with $\vec{B} \approx \vec{H}$.

For all spatial points, we can predict the change in NV splitting with the applied background field ($H_z$) by knowing the symmetry breaking stress parameter ($E$). At temperatures $T > T_C$, all points surveyed on the sample show good agreement with this predicted response. However, we observe a clear variation in the local magnetic field across the sample on ZFC. In particular, specific regions on the sample show a consistent suppression of the splitting from predictions. Specifically, at points of largest suppression (for sample 1) we extract $B/H \sim 0.7$. This suggests that while the sample may completely expel the background field from the bulk (leading to $\vec{B} = 0$ in the interior), the NV ensembles are somewhat further away (in $z$) from the sample.

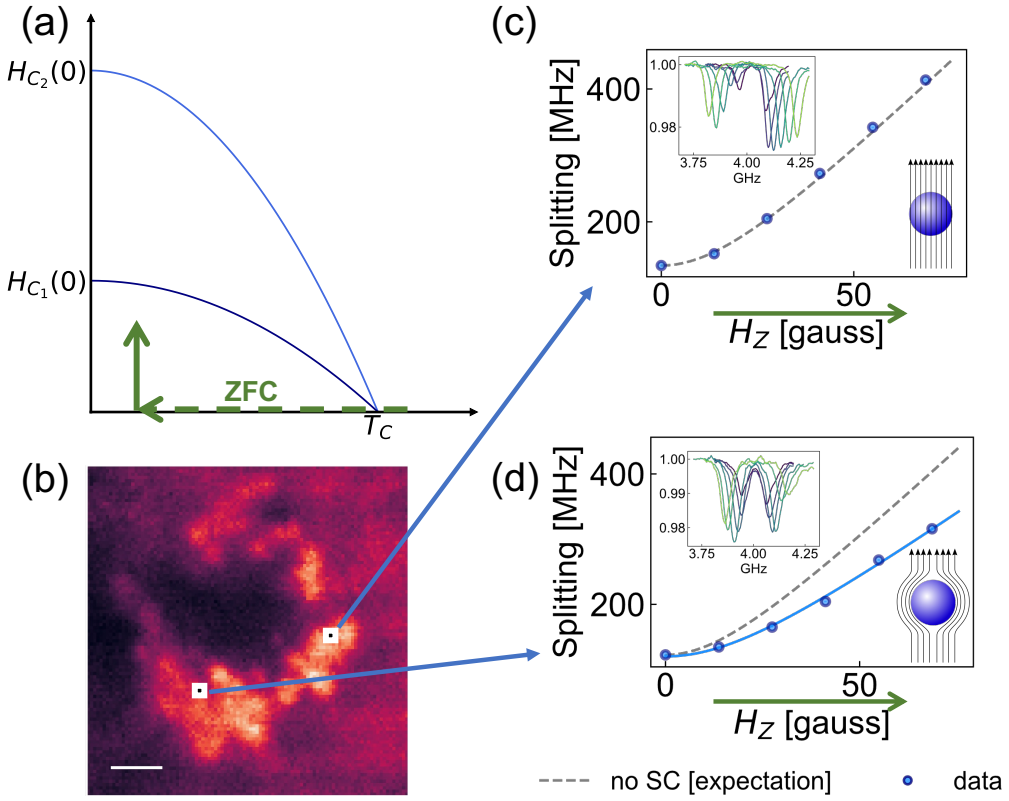


Figure 7.7: **Observation of Meissner effect on ZFC:** (a) Phase diagram of a type II superconductor. The ZFC path (green broken arrow) involves cooling below $T_C$ at zero applied background field. Deep in the superconducting state following ZFC, the sample resists the permeation of applied fields (Meissner effect). We test this by ramping up a background $H_z$ field (solid green arrow) and studying the evolution of the splitting. (b) Confocal scan of the sample showing laser heated regions (bright areas). The NV splittings at two representative points show markedly different behavior on ZFC. White Scale bar denotes 10 µm. (c) A study of NV splitting with applied $H_z$ field (green arrow on abscissa connects to the path taken in phase map). At this spatial point, the NV splitting data follows the expectation based on the calibrated applied field. This behavior is consistent with no superconductivity (SC) in this region (grey line) where $B_z \approx H_z$. Insets show the cwODMR data (top) and illustration of the inferred sample behavior at this point (bottom) [24]. (d) A study of NV splitting with applied $H_z$ field shows clear suppression. We can extrapolate the expected (no SC) response (gray line) in this sample region by noting the splitting ($2E$) at zero applied field. However, the observed splittings (blue data points) show a marked deviation from this expectation , suggesting local suppression of the applied field due to the Meissner response of the sample. Fitting a hyperbolic profile to the splitting $\Delta\nu = \sqrt{(2E)^2 + (2\gamma\, B_z)^2}$ (blue line) gives $B_z/H_z \approx 0.7$. Insets show cwODMR spectra and inferred magnetic response of the sample [24].

### Spatial Studies

Spatially resolved ZFC measurements (Fig. 7.7 (a)) can allow us to identify extent of the Meissner response. In particular, a line cut along the laser heated region shows a spatially varying suppression ($B/H$ ratio) of the applied field (Fig. 7.8). Our measurements clearly show that laser heating does not create the target hydride complex uniformly across the sample. In fact, most laser heated regions in the sample do not show such marked suppression, symptomatic of stochastic synthesis of the sample. The ability to locally survey the magnetic response of the sample can be leveraged in honing successful synthesis recipes for future loadings.

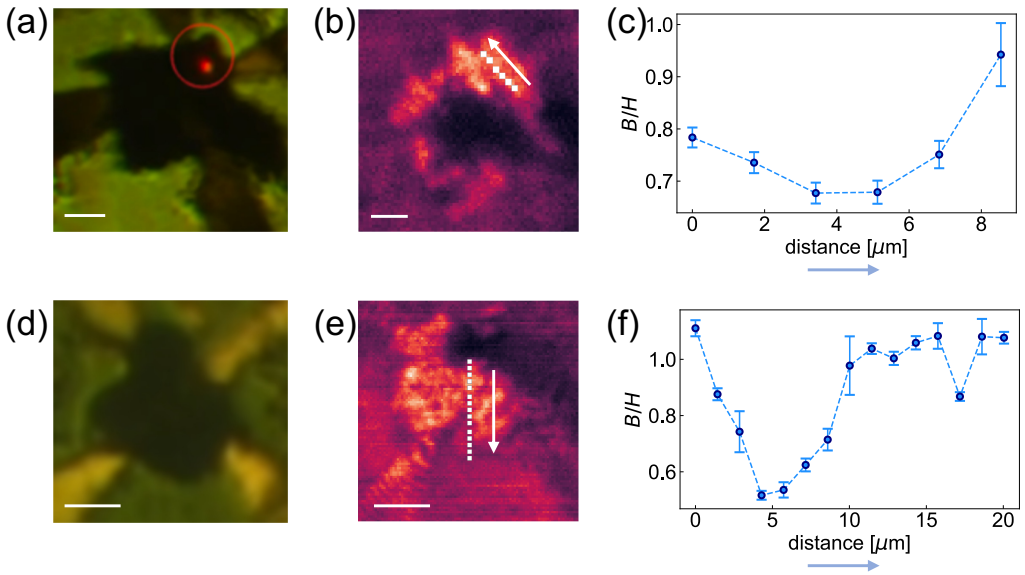


Figure 7.8: **Spatial studies of Meissner suppression:** (a) Optical microscope image of sample 1 showing Cerium metal and transport leads. (b) Confocal image of sample 1 (partially rotated with respect to (a)). Performing ZFC measurements of the type in Fig. 7.7 along a line cut (white points) allows us to observe the spatial extent of the Meissner suppression. (c) The ratio of $B/H$ obtained along the line cut in (b). The white arrow in (b) gives the direction of increasing distance. The measurement shows that the sample size is of the order of $\lesssim 10\,\mu$m. Studies on sample 2 (d-f) yield similar results. In all images, white scale bars denote $10\,\mu$m.

### Temperature Studies

After having identified the regions of the sample showing clear suppression of the applied field, the natural next step is to measure the temperature dependence of this suppression. We start with a ZFC sample and apply a background magnetic field (Fig. 7.7 (a)). At a high

enough field ($H_Z \sim 80\,\mathrm{G}$), the difference between the expected splitting (without SC) and the measured splitting (due to local Meissner suppression) is $\gtrsim 100\,\mathrm{MHz}$ (inset of Fig. 7.9 (a)). At this step, we fix the applied field and measure the change in the splitting when ramping up the temperature (taking a path shown by the solid green arrow in Fig. 7.9 (a)). We measure a clear increase in the splitting as we approach $T_C$ of the sample. Consistent with our expectations above $T_C$, the applied $H_Z$ field (without any suppression) determines the NV splitting. Crucially, concomitant with this loss of field suppression, simultaneous transport measurements show a sharp jump in the sample resistance. Our measurements probe the dual hallmarks of superconducting behavior, providing clear evidence of superconductivity in a superhydride material.

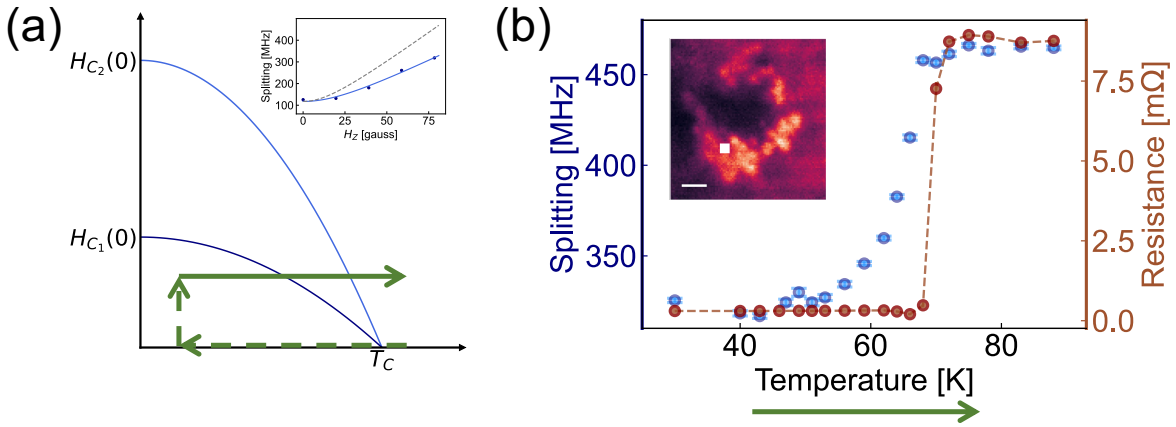


Figure 7.9: ***Simultaneous* transport and magnetism studies on ZFC:** (a) Path taken in phase space. Green broken arrows show preparatory steps. Starting in the normal state, we perform ZFC and then apply a background $H_z$ field. Fixing the applied field at $\sim 80\,\mathrm{G}$, we increase the temperature (green solid arrow). (Inset) Due to the Meissner effect, the NV splitting is suppressed near the superconductor with the difference in observed and expected splitting being $\gtrsim 100\,\mathrm{MHz}$. (b) Simultaneous transport and magnetometry measurements show an increase in the NV splitting and a sharp rise in the sample resistance. Image in the inset shows the spatial point (white square) at which the NV splitting was monitored. White scale bar denotes $10\,\mu\mathrm{m}$.

**Note:** The considerably gradual transition in magnetic behavior is possible due to several causes. On the one hand, it may show a dependence of the penetration depth with temperature. Specifically, near $T_C$, the penetration depth of the sample may be larger, allowing for more of the applied field to permeate the sample. Consequently, there would be less suppression at the location of the NV centers. On the other hand, the onset of this increase in splitting (near $\sim 50\,\mathrm{K}$) may be indicative of the system crossing $H_{C_1}(T)$. At this point, the applied field may permeate the sample as vortices. As we continue to

investigate the exact cause, we note (at a very crude level) that the temperature profile of sample magnetism is more characteristic of type II superconductors [77].

## Field cooling: evidence of flux trapping

Ostensibly, a high pressure superhydride is a dirty mesoscopic superconductor, suggesting that an interplay of sample geometry and disorder dictates it's behavior. For such a system, we expect qualitatively different effects on field cooling (FC) compared to ZFC [47]. Specifically, when cooling through the superconducting transition with an applied field, we can traverse the mixed state for temperatures where $H_{C_1}(T) < H < H_{C_2}(T)$. The vortices formed in the mixed state can subsequently get 'pinned' to sample defects on further cooling to temperatures where $H < H_{C_1}(T)$ [71]. Instead of showing Meissner effect deep in the superconducting phase, these pinned vortices allow the applied field to penetrate the sample. Remarkably, the supercurrents maintaining the vortices can persist even when the applied external field ($H_Z$) is quenched. Vortex pinning, therefore, freezes an effective magnetic moment into the sample that NV centers can subsequently measure at the culet.

**Note:** In addition to vortex pinning in type II superconductors, both type I and type II materials may show flux trapping due to sample geometry. The applied field can permeate the sample on field cooling through macroscopic holes in the hydride complex. When this applied field is quenched, the supercurrents around these holes can persist, leading to qualitatively similar effects as vortex pinning. Work distinguishing between these two cases in our high pressure sample is ongoing.

### Temperature studies

Cooling below the superconducting transition with an applied field ($H_z \sim 80\,\mathrm{G}$), we monitor sample resistance and NV splitting at four different spatial points on the culet (Fig. 7.10). In this case, we observe a considerably weaker transition signal with a change in the splitting of $\approx 15\,\mathrm{MHz}$ (in comparison to the ZFC case where the change in splitting was $> 100\,\mathrm{MHz}$ for the same applied field). Nevertheless, the profile of the measured splitting against temperature shows a clear transition point concurrent with a drop in sample resistance. Changes in the local magnetic field manifest as a decrease (increase) in the splitting at points within (at the edge) of the superconducting (SC) region of the sample. In contrast, a spatial point far from this SC region does not show any perceptible change in splitting across the transition.

### Field quenching

Quenching the applied background field (taking $H_z \to 0$) after field cooling, we measure cwODMR spectra at the same four spatial points on the culet (Fig. 7.10 (b)). In this case, the trapped flux in the sample manifests as a locally varying magnetic field. On the SC region of the sample, the measured splitting is higher than $2E$ (given by the symmetry breaking

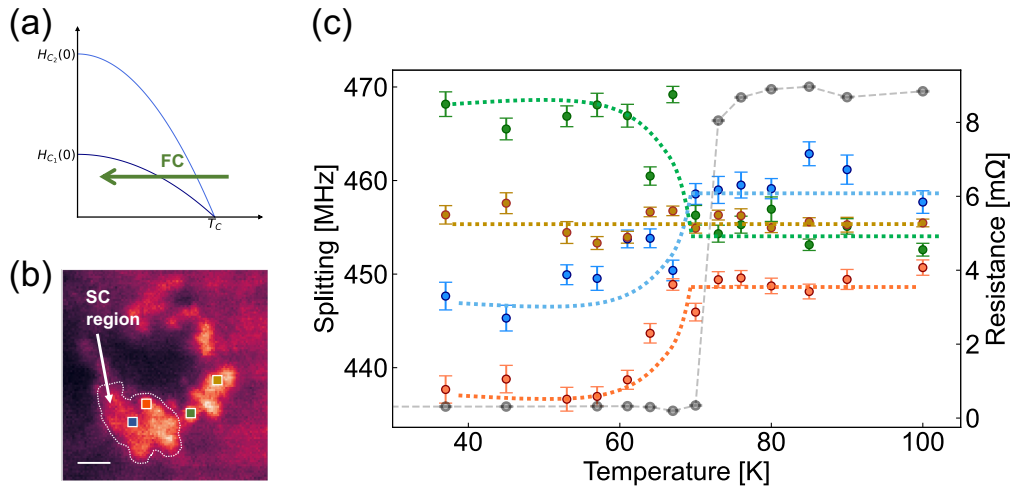


Figure 7.10: **FC studies across the superconducting transition:** (a) The path taken along the phase diagram for FC temperature sweep. (b) Confocal scan of the sample showing the superconducting (SC) region enclosed in white broken lines. White scale bar denotes 10 µm. The NV splitting was surveyed at four spatial points (color-coded to data in (c)). (c) On field cooling, we observe a decrease in the NV splitting at points on the superconducting region (blue and red) and an increase in the NV splitting at the edge of this region (green). The onset of these changes roughly corresponds to a drop in the resistance of the sample (grey). There is no perceptible change in the splitting across $T_C$ for a point far away from the superconducting region. Colored broken lines are a guide to the eye showing the splitting profile at each spatial point.

stress previously measured on ZFC). Away from the SC region, there is no difference between ZFC and FC measurements. Our measurements (Fig. 7.11) clearly show, for the first time, flux trapping in a superhydride system on field cooling [47].

## Field Cooling: applying negative fields

The flux trapped in the superconductor on field cooling defines some (hysteretic) notion of field direction. Specifically, this trapped flux will be oriented along the direction of the applied background field ($\vec{H}$) during FC. By reversing this background field's direction relative to the trapped flux, we can directly measure the competition between the two. In particular, we start at $H_z = 0$ after FC, where the overall magnetic moment due to flux trapping manifests as a splitting $\Delta\nu > 2E$ in the SC region (where $E$ is the symmetry breaking stress parameter measured at the same spatial point on ZFC). By applying negative fields (direction of $H_z$ opposite to trapped flux as shown in Fig. 7.12 (b)), we first measure a

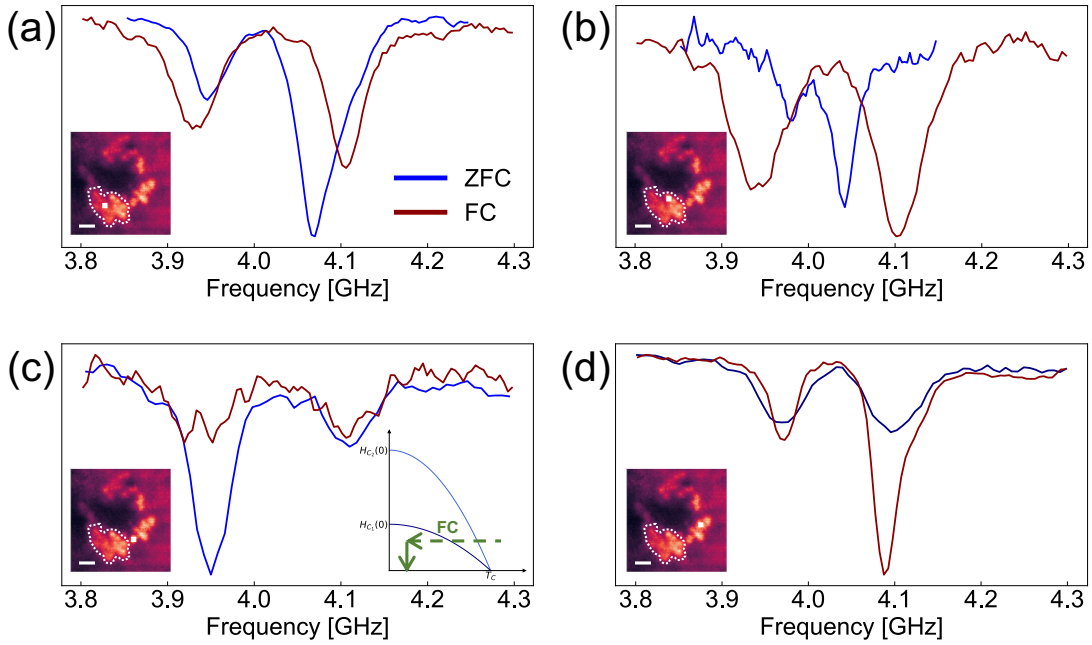


Figure 7.11: **Comparison of measurements at $H_z = 0$ after ZFC and FC:** cwODMR spectra on ZFC (FC) shown in blue (red) at four spatial points. Insets show the spatial point (white dot) corresponding to the measured spectra. Details of the confocal map in the inset are identical to Fig. 7.10 (b). Points (a) and (b) on the SC region clearly show a larger splitting on FC compared to ZFC, suggesting the presence of a local magnetic moment due to trapped flux in the sample. In contrast, points (c) and (d) do not show any perceptible difference between ZFC and FC, serving as a control for parasitic background fields. The right inset in (c) shows the path taken in the phase map for these measurements.

decrease in the splitting down to $\approx 2E$. This is because the applied $H_z$ field competes with the magnetic field due to the trapped flux at the location of the NV center. On increasing the magnitude of this negative background field, we see an increase in the NV splitting (Fig. 7.12 (c) and (d)).

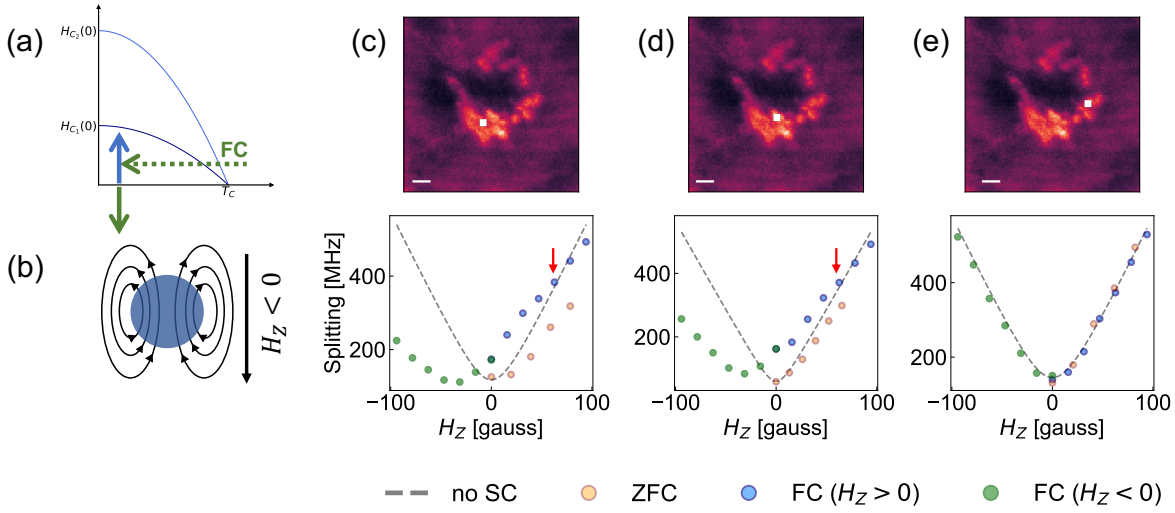


Figure 7.12: **Flux trapping in negative fields:** (a) The measurement protocol comprises field cooling (FC) deep into the superconducting phase and then quenching the background field. Subsequently, we tuned both magnitude and direction of $H_z$, applying both positive (blue) and negative (green) fields. (b) An illustration showing the application of negative fields. The direction of the applied $H_z$ during FC is frozen into the sample as a trapped flux. A negative applied field is oriented opposite to this direction and therefore competes with the 'effective' magnetic moment of the sample. (c-d) Plots showing the spatial location where the study was performed (top) and the observed profile of the NV splitting in different cases (bottom). Spatial points in (c) and (d) probe the SC region of the sample, while point (e) is located away from this region and serves as a control. For points (c) and (d), we see clear suppression of the applied magnetic field on ZFC (orange data points) relative to the expectation in the absence of a superconductor (grey line). In contrast, the splitting at point (e) closely follows the 'no SC' expectation. On FC and quenching the magnetic field, we measure NV splitting to be higher than $2E$ (given by the symmetry breaking stress) at points (c) and (d) due to trapped fluxes in this region. On applying positive fields (blue), we do not see a clear suppression of the splitting until the applied field magnitude exceeds the value at which field cooling was performed ($\sim 80$ G shown by red arrow). Most interestingly, on applying negative fields, we directly see the competition between the trapped flux and the background field manifest in the NV splitting. At small magnitudes of negative field, the NV splitting (green) at points (c) and (d) first decreases down to $\sim 2E$. On further increasing the magnitude of the negative field, the splitting increases but is suppressed with a $B/H$ ratio comparable to the case of ZFC. Crucially for the control point (e), we do not see any difference between the three scenarios, and the splitting closely follows the 'no SC' expectation in all cases.

### Temperature studies

Sweeping the temperature at negative fields, we observe an increase in the NV splitting on the SC region at $T_C$ (up to values consistent with the applied background field). Coincident with this jump in splitting, we observe an increase in the sample resistance (and phase), indicating that the sample reverts to the normal state (Fig. 7.13).

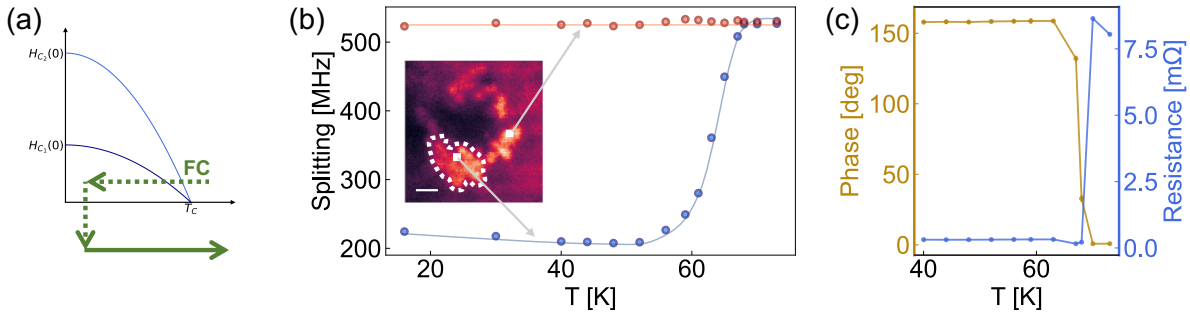


Figure 7.13: **Temperature sweep at negative fields after FC:** (a) Path taken in the phase map. We sweep the temperature after applying negative fields to a FC sample. The applied background field $H_z$ competes with the trapped flux in the superconductor. (b) We survey two spatial points on the sample (inset). A point away from the SC region of the sample yields an NV splitting consistent with the applied background field ($H_z$) (orange data points). This is the same spatial point measured in Fig. 7.12 (e). The splitting does not show any marked change on increasing temperature across the transition point. A point in the SC region (surveyed in Fig. 7.12(c)) shows a clear increase in splitting reaching values consistent with $H_z$ at $T \sim 70\,\mathrm{K}$. (c) Simultaneous lock-in measurements of transport yield sample resistance and phase consistent with the superconducting transition at $T \sim 70\,\mathrm{K}$. In (b) and (c), $T$ is the temperature measured at the cold finger of the cryostat. The true sample temperature is $\sim 20\,\mathrm{K}$ higher due to a thermal gradient in the DAC.

### Magnetic field sweeps

We can study the energy landscape of vortex pinning by sweeping the background magnetic field after field cooling to different temperatures (Fig. 7.14 (a)). For these measurements, we consistently field cool the sample at $\sim 100\,\mathrm{G}$. We maintain the same field direction (fixed in the lab frame) during each FC cycle. Deep in the SC phase ($T \ll T_C$), we observe the trapped flux remains pinned to the sample even on sweeping to large negative field values ($|H_z| > 100\,\mathrm{G}$). However, closer to the transition point, a background field swept through the same parameter regime strongly modulates the energy landscape allowing the pinned flux to escape the sample. In Fig. 7.14 (b), we see that for $T \sim 65\,\mathrm{K}$, the NV splitting at negative fields deviates from measurements deep in the SC phase. Increasing the magnitude

of the negative field allows flux lines oriented in the negative field direction to permeate the sample. This is evidenced by the change in the splitting on sweeping back to positive field regimes.

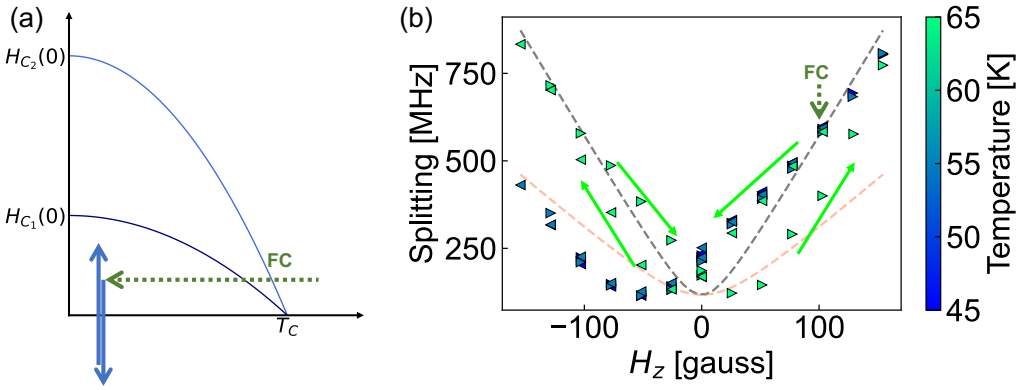


Figure 7.14: **Sweeping magnetic fields on field cooling:** (a) The path taken in the phase map involves field cooling at $\sim 100\,\mathrm{G}$ to a fixed temperature below the transition point followed by sweeping the magnetic field - first to negative and then back to positive values. (b) The evolution of the NV splitting in comparison to cases of ZFC (broken red line) and no SC expectation (broken gray line) is shown for three temperature points. At $T \ll T_C$ (45 K and 50 K), we see the retention of the trapped flux in the sample even on changing sweeping the fields to large (negative values). However, for $T \sim 65\,\mathrm{K}$, the trapped flux at positive fields is not as strongly pinned when the background field is swept to negative values. At large negative values of the field, flux lines along the negative field direction permeate the sample. Sweeping the field back to the positive direction, we now see the opposite effect wherein the trapped flux along the negative field direction competes with the background field at the NV location.

## 7.4 Conclusion

In this chapter, I outlined our study of superconductivity in a high pressure superhydride system. Using NV magnetometry in synergy with transport, we simultaneously probe the two defining characteristics of superconductors at pressures nearing $\sim 150\,\mathrm{GPa}$. Our measurements can identify local magnetic field suppression indicative of the Meissner effect. In contrast to inductive measurements that integrate the signal from the entire sample [50, 34, 97], this technique can identify points in the sample where the target hydride complex has been successfully synthesized. We see qualitatively different behaviors on ZFC and FC studies characteristic of disordered superconductors. We uncover clear evidence of flux trapping

on FC. Our ZFC measurements show consistent signatures of spatially resolved Meissner suppression in two separate samples.

From the standpoint of materials characterization, our current work has several immediate extensions. First, integrating such studies with widefield experiments will be a crucial step for increasing data throughput and providing a better idea of the spatial properties of the sample. Second, by tuning temperature and vector magnetic fields one can tailor different paths in the phase diagram to extract characteristic parameters such as $\lambda$ and $\xi$. Third, using DC magnetometry through cwODMR measurements, we can probe slow dynamics of the superconductor, such as flux creep [101]. Finally, by leveraging AC magnetometry, we can measure the spectral characteristics of noise, and AC susceptibility [110] across the transition point to further probe microscopic properties such as the pairing mechanism [31]. I end this thesis with a figure to demonstrate the viability of AC sensing at megabar pressures. Although I am excited about its prospects, I will likely not be able to embark on that leg of the study. Nevertheless, I am confident it won't be long until they are carried out!

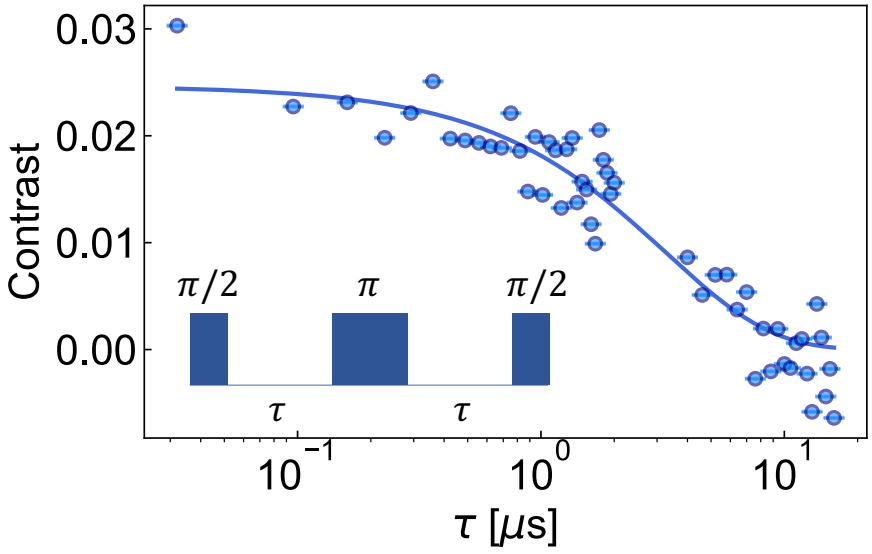


Figure 7.15: **Looking ahead:** Spin echo measurement performed on sample 2 at $\sim$ 130 GPa. A simple exponential fit gives $T_2^{\text{echo}} \approx 3\,\mu\text{s}$ at these pressures. The inset shows the microwave pulse sequence for the measurement. Coherent measurements are a powerful way to perform AC magnetometry to diagnose interesting features such as critical noise across phase transitions [18]. I am sure that future work on superhydrides and other high pressure systems, using a plethora of quantum sensing techniques such as this, will uncover exciting insights!

# Chapter 8

# Next steps...

In this thesis, I have described several studies on high pressure metrology application of NV color centers in diamond. We performed proof of principle demonstrations of diffraction-limited imaging of magnetic and stress fields in high pressure environments. We also demonstrated the use of this platform between room temperature and cryogenic temperatures. Furthermore, we built upon previous work on the inter-system crossing [45] of the NV center to extend the application of these sensing techniques to megabar pressures. At pressures nearing $\sim 150\,\mathrm{GPa}$, we achieved a sensitivity of $\approx 50\,\mu\mathrm{T}/\sqrt{\mathrm{Hz}}$. This platform will find applications in condensed matter and geophysical investigations. In this brief epilogue, I will recapitulate some thoughts on future work. I source my comments from the final sections of each chapter, where I already discuss these matters in some detail. Nevertheless, some key advantages, extensions, and applications are worth highlighting a second time.

At the level of NV physics, some interesting studies can be designed to look at the effect of stress on the excited state orbitals and the intersystem crossing. In particular, playing with different excitation wavelengths, it may be possible to identify ISC transition rates from different orbital states. Furthermore, by tuning polarization and excitation wavelengths, it may be possible to perform stress calibration and sensing using orbital states in high stress regimes (similar to work in [16]).

At a technological level, NV sensing under pressure can be extended in many ways. First, the characterization and application of pulsed measurements can extend quantum sensing techniques already demonstrated under ambient conditions to high pressure studies [9, 110]. Second, circuit design for the application of MW with better control (such as rotation of MW polarization [4]) can allow us to improve efficiency in stress tensor measurements. Third, by using double beveled anvils, we can explore the extension of NV experiments to multi-megabar pressures [78].

For condesed matter experiments, tuning pressure as a thermodynamic parameter allows us to explore interesting phases [46] and synthesize novel materials [34]. In the former case, the ability to characterize systems *in situ* and leverage sensing modalities (such as $T_1$ relaxometry [18]) can provide new techniques to probe condensed phases. In the latter case, reliable and efficient characterization methodologies (demonstrated in the context of super-

hydrides in this thesis) can be leveraged to optimize synthesis recipes. With the discovery of more hydrides and the ability to synthesize them with better control, I am hopeful that these materials (with near room temperature $T_C$) might someday be technologized as useful materials in their own right.

For geophysical investigations, where the high pressure phases of materials are of crucial importance, there are some immediate applications of NV color centers. First, as an *in situ* pressure calibrant, the NV center can allow us to measure the pressure in the sample chamber directly. In particular, the ability to measure shear stress at the diamond-sample interface can allow for a more accurate characterization of sample response to static stress. By obviating the requirement of loading ruby spheres into the chamber, this process not only simplifies loading techniques but also allows for more homogeneous samples. Second, the ability to image the stress components allows for better characterization of stress gradients. On the one hand, this can enable anvil design that enables more homogeneous pressure application. On the other hand, this ability may be crucial in studies where stress gradients themselves are of central importance (e.g., rotational DACs) [63]. Finally, as we have shown in this thesis (chapter 5), directly imaging changes in stress components across pressure induced events (e.g., volume collapse, acoustic emissions, phase nucleations) can reveal interesting connections between stress environments and sample response. In combination with other standard high pressure tools (such as XRD), *in situ* NV measurements in tabletop experiments can allow us to cast a wider net on scientific inquiries.

# Bibliography


[1] V. M. Acosta et al. "Temperature Dependence of the Nitrogen-Vacancy Magnetic Resonance in Diamond". In: *Phys. Rev. Lett.* 104 (7 Feb. 2010), p. 070801. DOI: 10.1103/PhysRevLett.104.070801. URL: https://link.aps.org/doi/10.1103/PhysRevLett.104.0708012.

[2] Yuichi Akahama and Haruki Kawamura. "Pressure calibration of diamond anvil Raman gauge to 310 GPa". In: *Journal of Applied Physics* 100.4 (2006), p. 043516.

[3] Yuichi Akahama and Haruki Kawamura. "Raman study on the stress state of [111] diamond anvils at multimegabar pressure". In: *Journal of applied physics* 98.8 (2005), p. 083523.

[4] TP Alegre et al. "Polarization-selective excitation of NV centers in diamond". In: *arXiv preprint arXiv:0705.2006* (2007).

[5] DJ Andrews. "Equation of state of the alpha and epsilon phases of iron". In: *Journal of Physics and Chemistry of Solids* 34.5 (1973), pp. 825–840.

[6] N. W. Ashcroft. "Metallic Hydrogen: A High-Temperature Superconductor?" In: *Phys. Rev. Lett.* 21 (26 Dec. 1968), pp. 1748–1749. DOI: 10.1103/PhysRevLett.21.1748. URL: https://link.aps.org/doi/10.1103/PhysRevLett.21.1748.

[7] Nabeel Aslam et al. "Photo-induced ionization dynamics of the nitrogen vacancy defect in diamond investigated by single-shot charge state detection". In: *New Journal of Physics* 15.1 (2013), p. 013064.

[8] A-L Auzende et al. "High-pressure behaviour of serpentine minerals: a Raman spectroscopic study". In: *Physics and Chemistry of Minerals* 31.5 (2004), pp. 269–277.

[9] John F. Barry et al. "Sensitivity optimization for NV-diamond magnetometry". In: *Rev. Mod. Phys.* 92 (1 Mar. 2020), p. 015004. DOI: 10.1103/RevModPhys.92.015004. URL: https://link.aps.org/doi/10.1103/RevModPhys.92.015004.

[10] Michael SJ Barson et al. "Nanomechanical sensing using spins in diamond". In: *Nano letters* 17.3 (2017), pp. 1496–1503.

[11] William A Bassett. "Deviatoric stress: a nuisance or a gold mine?" In: *Journal of Physics: Condensed Matter* 18.25 (2006), S921.

[12] William A. Bassett. "Diamond anvil cell, 50th birthday". In: *High Pressure Research* 29.2 (2009), pp. 163–186. DOI: 10.1080/08957950802597239. eprint: https://doi.org/10.1080/08957950802597239. URL: https://doi.org/10.1080/08957950802597239.

[13] J Georg Bednorz and K Alex Müller. "Perovskite-Type Oxides—the New Approach to High-Tc Superconductivity. Nobel Lecture". In: *Angewandte Chemie International Edition in English* 27.5 (1988), pp. 735–748.

[14] R Berman, Franz Eugen Simon, and John Michael Ziman. "The thermal conductivity of diamond at low temperatures". In: *Proceedings of the Royal Society of London. Series A. Mathematical and Physical Sciences* 220.1141 (1953), pp. 171–183.

[15] Magali I Billen. "Deep slab seismicity limited by rate of deformation in the transition zone". In: *Science advances* 6.22 (2020), eaaz7692.

[16] M Block et al. "Optically enhanced electric field sensing using nitrogen-vacancy ensembles". In: *Physical Review Applied* 16.2 (2021), p. 024024.

[17] E Bourgeois et al. "Photoelectric detection of electron spin resonance of nitrogen-vacancy centres in diamond". In: *Nature Communications* 6.1 (Oct. 2015), p. 8577.

[18] Shubhayu Chatterjee, Joaquin F Rodriguez-Nieva, and Eugene Demler. "Diagnosing phases of magnetic insulators via noise magnetometry with spin qubits". In: *Physical Review B* 99.10 (2019), p. 104425.

[19] Yu-Chen Chen et al. "Laser writing of coherent colour centres in diamond". In: *Nature Photonics* 11.2 (2017), pp. 77–80.

[20] Edward H. Chen et al. "High-sensitivity spin-based electrometry with an ensemble of nitrogen-vacancy centers in diamond". In: *Phys. Rev. A* 95 (5 May 2017), p. 053417. DOI: 10.1103/PhysRevA.95.053417. URL: https://link.aps.org/doi/10.1103/PhysRevA.95.053417.

[21] Wuhao Chen et al. "High-Temperature Superconducting Phases in Cerium Superhydride with a T c up to 115 K below a Pressure of 1 Megabar". In: *Physical Review Letters* 127.11 (2021), p. 117001.

[22] Lilian Isabel Childress. *Coherent manipulation of single quantum systems in the solid state*. Harvard University, 2007.

[23] Yiwen Chu and Mikhail D Lukin. "Quantum optics with nitrogen-vacancy centers in diamond". In: *Quantum Optics and Nanophotonics* (2015), pp. 229–270.

[24] Wikimedia Commons. *Expulsion of magnetic field lines upon entering the superconducting phase*. Piotr Jaworski; ; Poznań/POLAND. 2005. URL: https://commons.wikimedia.org/wiki/File:EXPULSION.png.

[25] Jian-Hong Dai et al. "Optically Detected Magnetic Resonance of Diamond NV Centers under Megabar Pressures". In: *Chinese Physics Letters* (2022). URL: http://iopscience.iop.org/article/10.1088/0256-307X/39/11/117601.

[26] Gordon Davies and MF Hamer. "Optical studies of the 1.945 eV vibronic band in diamond". In: *Proceedings of the Royal Society of London. A. Mathematical and Physical Sciences* 348.1653 (1976), pp. 285–298.

[27] Agnès Dewaele and Lucie Nataf. "Magnetic phase diagram of iron at high pressure and temperature". In: *Phys. Rev. B* 106 (1 July 2022), p. 014104. DOI: 10.1103/PhysRevB.106.014104. URL: https://link.aps.org/doi/10.1103/PhysRevB.106.014104.

[28] Marcus W. Doherty et al. "Electronic Properties and Metrology Applications of the Diamond $NV^-$ Center under Pressure". In: *Phys. Rev. Lett.* 112 (4 Jan. 2014), p. 047601. DOI: 10.1103/PhysRevLett.112.047601. URL: https://link.aps.org/doi/10.1103/PhysRevLett.112.047601.

[29] Marcus W. Doherty et al. "The nitrogen-vacancy colour centre in diamond". In: *Physics Reports* 528.1 (2013). The nitrogen-vacancy colour centre in diamond, pp. 1–45. ISSN: 0370-1573. DOI: https://doi.org/10.1016/j.physrep.2013.02.001. URL: https://www.sciencedirect.com/science/article/pii/S0370157313000562.

[30] Florian Dolde et al. "Electric-field sensing using single diamond spins". In: *Nature Physics* 7.6 (2011), pp. 459–463.

[31] Pavel E Dolgirev et al. "Characterizing two-dimensional superconductivity via nanoscale noise magnetometry with single-spin qubits". In: *Physical Review B* 105.2 (2022), p. 024507.

[32] A. P. Drozdov et al. "Conventional superconductivity at 203 kelvin at high pressures in the sulfur hydride system". In: *Nature* 525.7567 (Sept. 2015), pp. 73–76. ISSN: 1476-4687. DOI: 10.1038/nature14964. URL: https://doi.org/10.1038/nature14964.

[33] A. P. Drozdov et al. "Superconductivity at 250 K in lanthanum hydride under high pressures". In: *Nature* 569.7757 (May 2019), pp. 528–531. ISSN: 1476-4687. DOI: 10.1038/s41586-019-1201-8. URL: https://doi.org/10.1038/s41586-019-1201-8.

[34] AP Drozdov et al. "Conventional superconductivity at 203 kelvin at high pressures in the sulfur hydride system". In: *Nature* 525.7567 (2015), pp. 73–76.

[35] Natalia Dubrovinskaia and Leonid Dubrovinsky. "Whole-cell heater for the diamond anvil cell". In: *Review of Scientific Instruments* 74.7 (2003), pp. 3433–3437.

[36] M.I. Eremets. *High Pressure Experimental Methods*. Oxford science publications. Oxford University Press, 1996. ISBN: 9780198562696. URL: https://books.google.com/books?id=3bqD0mTR0N8C.

[37] Jacopo Forneris et al. "Mapping the Local Spatial Charge in Defective Diamond by Means of N-V Sensors—A Self-Diagnostic Concept". In: *Physical Review Applied* 10.1 (2018), p. 014024.

[38] C Frohlich. "The Nature of Deep-Focus Earthquakes". In: *Annual Review of Earth and Planetary Sciences* 17.1 (1989), pp. 227–254. DOI: 10.1146/annurev.ea.17.050189.001303. eprint: https://doi.org/10.1146/annurev.ea.17.050189.001303. URL: https://doi.org/10.1146/annurev.ea.17.050189.001303.

[39] Cliff Frohlich. *Deep Earthquakes*. Cambridge University Press, 2006. DOI: 10.1017/CBO9781107297562.

[40] GD Fuchs et al. "Excited-state spectroscopy using single spin manipulation in diamond". In: *Physical review letters* 101.11 (2008), p. 117601.

[41] AG Gavriliuk, AA Mironovich, and VV Struzhkin. "Miniature diamond anvil cell for broad range of high pressure measurements". In: *Review of Scientific Instruments* 80.4 (2009), p. 043906.

[42] BK Godwal et al. "High pressure equation of state studies using methanol–ethanol–water and argon as pressure media". In: *Journal of Physics and Chemistry of Solids* 71.8 (2010), pp. 1059–1064.

[43] Narayama Golding et al. "Plastic faulting in ice". In: *Journal of Geophysical Research: Solid Earth* 125.5 (2020), e2019JB018749.

[44] Michael Lurie Goldman et al. "Phonon-induced population dynamics and intersystem crossing in nitrogen-vacancy centers". In: *Physical review letters* 114.14 (2015), p. 145502.

[45] Michael Lurie Goldman et al. "State-selective intersystem crossing in nitrogen-vacancy centers". In: *Physical Review B* 91.16 (2015), p. 165201.

[46] Sara Haravifard et al. "Continuous and discontinuous quantum phase transitions in a model two-dimensional magnet". In: *Proceedings of the National Academy of Sciences* 109.7 (2012), pp. 2286–2289.

[47] JE Hirsch and F Marsiglio. "Evidence against superconductivity in flux trapping experiments on hydrides under high pressure". In: *Journal of Superconductivity and Novel Magnetism* 35.11 (2022), pp. 3141–3145.

[48] Kin On Ho et al. "Recent developments of quantum sensing under pressurized environment using the nitrogen vacancy (NV) center in diamond". In: *Journal of Applied Physics* 129.24 (2021), p. 241101.

[49] S Hsieh et al. "Imaging stress and magnetism at high pressures using a nanoscale quantum sensor". In: *Science* 366.6471 (2019), pp. 1349–1354.

[50] Xiaoli Huang et al. "High-temperature superconductivity in sulfur hydride evidenced by alternating-current magnetic susceptibility". In: *National Science Review* 6.4 (2019), pp. 713–718.

[51] Ryuji Igarashi et al. "Real-Time Background-Free Selective Imaging of Fluorescent Nanodiamonds in Vivo". In: *Nano Letters* 12.11 (Nov. 2012), pp. 5726–5732.

[52] Kay D Jahnke et al. "Electron–phonon processes of the silicon-vacancy centre in diamond". In: *New Journal of Physics* 17.4 (2015), p. 043011.

[53] P. Jamonneau et al. "Competition between electric field and magnetic field noise in the decoherence of a single spin in diamond". In: *Phys. Rev. B* 93 (2 Jan. 2016), p. 024305. DOI: 10.1103/PhysRevB.93.024305. URL: https://link.aps.org/doi/10.1103/PhysRevB.93.024305.

[54] A Jarmola et al. "Temperature-and magnetic-field-dependent longitudinal spin relaxation in nitrogen-vacancy ensembles in diamond". In: *Physical review letters* 108.19 (2012), p. 197601.

[55] A Jayaraman. "High pressure studies: Metals, alloys and compounds". In: *Handbook on the Physics and Chemistry of Rare Earths* 1 (1978), pp. 707–747.

[56] Innokenty Kantor et al. "BX90: A new diamond anvil cell design for X-ray diffraction and optical measurements". In: *Review of Scientific Instruments* 83.12 (2012), p. 125102.

[57] Kathleen J Kingma et al. "High-pressure crystalline transformations and amorphization in $\alpha$-quartz". In: *AIP Conference Proceedings*. Vol. 309. American Institute of Physics. 1994, pp. 39–42.

[58] MB Kruger and Raymond Jeanloz. "Memory glass: an amorphous material formed from AlPO4". In: *Science* 249.4969 (1990), pp. 647–649.

[59] Y Kubo et al. "Strong Coupling of a Spin Ensemble to a Superconducting Resonator". In: *Physical Review Letters* 105.14 (Sept. 2010), p. 140502.

[60] Ngoc Diep Lai et al. "Influence of a static magnetic field on the photoluminescence of an ensemble of nitrogen-vacancy color centers in a diamond single-crystal". In: *Applied Physics Letters* 95.13 (2009), p. 133101. DOI: 10.1063/1.3238467. eprint: https://doi.org/10.1063/1.3238467. URL: https://doi.org/10.1063/1.3238467.

[61] Margarita Lesik et al. "Magnetic measurements on micrometer-sized samples under high pressure using designed NV centers". In: *Science* 366.6471 (2019), pp. 1359–1362.

[62] A. O. Levchenko et al. "Inhomogeneous broadening of optically detected magnetic resonance of the ensembles of nitrogen-vacancy centers in diamond by interstitial carbon atoms". In: *Applied Physics Letters* 106.10 (2015), p. 102402. DOI: 10.1063/1.4913428. eprint: https://doi.org/10.1063/1.4913428. URL: https://doi.org/10.1063/1.4913428.

[63] Valery I Levitas. "High-pressure phase transformations under severe plastic deformation by torsion in rotational anvils". In: *Materials Transactions* 60.7 (2019), pp. 1294–1301.

[64] Valery I Levitas et al. "High-density amorphous phase of silicon carbide obtained under large plastic shear and high pressure". In: *Physical Review B* 85.5 (2012), p. 054114.

[65] Bing Li et al. "Diamond anvil cell behavior up to 4 Mbar". In: *Proceedings of the National Academy of Sciences* 115.8 (2018), pp. 1713–1717.

[66] DR Lide. *Handbook of Chemistry and Physics, 86th edn. CRC*. 2005.

[67] Shengran Lin et al. "Temperature-dependent coherence properties of NV ensemble in diamond up to 600 K". In: *Physical Review B* 104.15 (2021), p. 155430.

[68] Gang-Qin Liu et al. "Coherent quantum control of nitrogen-vacancy center spins near 1000 kelvin". In: *Nature communications* 10.1 (2019), pp. 1–8.

[69] S. G. Lyapin et al. "Study of optical properties of the NV and SiV centres in diamond at high pressures". English. In: *Nanosystems : Physics, Chemistry, Mathematics* 9.1 (2018). Copyright - Copyright St. Petersburg National Research University of Information Technologies, Mechanics and Optics 2018; Last updated - 2018-03-21, pp. 55–57. URL: https://www.proquest.com/scholarly-journals/study-optical-properties-nv-siv-centres-diamond/docview/2015777350/se-2.

[70] Ho-Kwang Mao et al. "Solids, liquids, and gases under high pressure". In: *Rev. Mod. Phys.* 90 (1 Mar. 2018), p. 015007. DOI: 10.1103/RevModPhys.90.015007. URL: https://link.aps.org/doi/10.1103/RevModPhys.90.015007.

[71] Teruo Matsushita et al. *Flux pinning in superconductors*. Vol. 164. Springer, 2007.

[72] Y Matsuzaki et al. "Optically detected magnetic resonance of high-density ensemble of $NV^-$ centers in diamond". In: *Journal of Physics: Condensed Matter* 28.27 (July 2016), p. 275302.

[73] Jeronimo R Maze et al. "Properties of nitrogen-vacancy centers in diamond: the group theoretic approach". In: *New Journal of Physics* 13.2 (2011), p. 025025.

[74] Charles Meade and Raymond Jeanloz. "Deep-focus earthquakes and recycling of water into the Earth's mantle". In: *Science* 252.5002 (1991), pp. 68–72.

[75] Thomas Mittiga et al. "Imaging the local charge environment of nitrogen-vacancy centers in diamond". In: *Physical review letters* 121.24 (2018), p. 246402.

[76] Robert M Nadeau and Lane R Johnson. "Seismological studies at Parkfield VI: Moment release rates and estimates of source parameters for small repeating earthquakes". In: *Bulletin of the Seismological Society of America* 88.3 (1998), pp. 790–814.

[77] NM Nusran et al. "Spatially-resolved study of the Meissner effect in superconductors using NV-centers-in-diamond optical magnetometry". In: *New Journal of Physics* 20.4 (2018), p. 043010.

[78] Earl F O'Bannon III et al. "Contributed Review: Culet diameter and the achievable pressure of a diamond anvil cell: Implications for the upper pressure limit of a diamond anvil cell". In: *Review of Scientific Instruments* 89.11 (2018), p. 111501.

[79] Eric Van Oort and Max Glasbeek. "Electric-field-induced modulation of spin echoes of N-V centers in diamond". In: *Chemical Physics Letters* 168.6 (1990), pp. 529–532. ISSN: 0009-2614. DOI: https://doi.org/10.1016/0009-2614(90)85665-Y. URL: http://www.sciencedirect.com/science/article/pii/000926149085665Y.

[80] László Oroszlány et al. "Magnetism of gadolinium: a first-principles perspective". In: *Physical review letters* 115.9 (2015), p. 096402.

[81] Chris J Pickard, Ion Errea, and Mikhail I Eremets. "Superconducting hydrides under pressure". In: *Annual Review of Condensed Matter Physics* 11 (2020), pp. 57–76.

[82] Hugh O Pierson. *Handbook of carbon, graphite, diamonds and fullerenes: processing, properties and applications*. William Andrew, 2012.

[83] Bruno Reynard et al. "Elasticity of serpentines and extensive serpentinization in subduction zones". In: *Geophysical Research Letters* 34.13 (2007).

[84] Lawrence Baylor Robinson, Frederick Milstein, and A Jayaraman. "Effect of pressure on the Curie temperature of rare-earth metals. I. Gadolinium". In: *Physical Review* 134.1A (1964), A187.

[85] LJ Rogers et al. "Time-averaging within the excited state of the nitrogen-vacancy centre in diamond". In: *New Journal of Physics* 11.6 (2009), p. 063007.

[86] L Rondin et al. "Magnetometry with nitrogen-vacancy defects in diamond". In: *Reports on Progress in Physics* 77.5 (May 2014), p. 056503.

[87] Gopi K Samudrala et al. "Structural and magnetic phase transitions in gadolinium under high pressures and low temperatures". In: *High Pressure Research* 34.4 (2014), pp. 385–391.

[88] Alexandre Schubnel et al. "Deep-focus earthquake analogs recorded at high pressure and temperature in the laboratory". In: *Science* 341.6152 (2013), pp. 1377–1380.

[89] Dmitrii V Semenok et al. "On distribution of superconductivity in metal hydrides". In: *Current Opinion in Solid State and Materials Science* 24.2 (2020), p. 100808.

[90] Yan-Xing Shang et al. "Magnetic Sensing inside a Diamond Anvil Cell via Nitrogen-Vacancy Center Spins". In: *Chinese Physics Letters* 36.8 (2019), p. 086201.

[91] Maria Simanovskaia et al. "Sidebands in optically detected magnetic resonance signals of nitrogen vacancy centers in diamond". In: *Phys. Rev. B* 87 (22 June 2013), p. 224106. DOI: 10.1103/PhysRevB.87.224106. URL: https://link.aps.org/doi/10.1103/PhysRevB.87.224106.

[92] T Smart et al. "High-pressure nano-seismology: Use of micro-ring resonators for characterizing acoustic emissions". In: *Applied Physics Letters* 115.8 (2019), p. 081904.

[93] Thomas James Smart. *Structural Transitions in Materials at High Pressure*. University of California, Berkeley, 2020.

[94] Benjamin Smeltzer, Lilian Childress, and Adam Gali. "13C hyperfine interactions in the nitrogen-vacancy centre in diamond". In: *New Journal of Physics* 13.2 (2011), p. 025021.

[95] Maddury Somayazulu et al. "Evidence for Superconductivity above 260 K in Lanthanum Superhydride at Megabar Pressures". In: *Phys. Rev. Lett.* 122 (2 Jan. 2019), p. 027001. DOI: 10.1103/PhysRevLett.122.027001. URL: https://link.aps.org/doi/10.1103/PhysRevLett.122.027001.

[96] LG Steele et al. "Optically detected magnetic resonance of nitrogen vacancies in a diamond anvil cell using designer diamond anvils". In: *Applied Physics Letters* 111.22 (2017), p. 221903.

[97] Viktor Struzhkin et al. "Superconductivity in La and Y hydrides: Remaining questions to experiment and theory". In: *Matter and Radiation at Extremes* 5.2 (2020), p. 028201.

[98] K Syassen. "Ruby under pressure". In: *High Pressure Research* 28.2 (2008), pp. 75–126.

[99] RD Taylor, MP Pasternak, and R Jeanloz. "Hysteresis in the high pressure transformation of bcc-to hcp-iron". In: *Journal of Applied Physics* 69.8 (1991), pp. 6126–6128.

[100] Gergő Thiering and Adam Gali. "Theory of the optical spin-polarization loop of the nitrogen-vacancy center in diamond". In: *Physical Review B* 98.8 (2018), p. 085207.

[101] Michael Tinkham. *Introduction to superconductivity*. Courier Corporation, 2004.

[102] Ivan Troyan et al. "Observation of superconductivity in hydrogen sulfide from nuclear resonant scattering". In: *Science* 351.6279 (2016), pp. 1303–1306.

[103] Pauli Virtanen et al. "SciPy 1.0: Fundamental Algorithms for Scientific Computing in Python". In: *Nature Methods* 17 (2020), pp. 261–272. DOI: 10.1038/s41592-019-0686-2.

[104] Yogesh K. Vohra et al. "Band-Overlap Metallization of Cesium Iodide". In: *Phys. Rev. Lett.* 55 (9 Aug. 1985), pp. 977–979. DOI: 10.1103/PhysRevLett.55.977. URL: https://link.aps.org/doi/10.1103/PhysRevLett.55.977.

[105] Stéfan van der Walt et al. "scikit-image: image processing in Python". In: *PeerJ* 2 (June 2014), e453. ISSN: 2167-8359. DOI: 10.7717/peerj.453. URL: https://doi.org/10.7717/peerj.453.

[106] EJW Whittaker and Jack Zussman. "The characterization of serpentine minerals by X-ray diffraction". In: *Mineralogical magazine and journal of the Mineralogical Society* 31.233 (1956), pp. 107–126.

[107] King Yau Yip et al. "Measuring magnetic field texture in correlated electron systems under extreme conditions". In: *Science* 366.6471 (2019), pp. 1355–1359.

[108] Alexander M. Zaitsev. "Physical Classification of Diamond". In: *Optical Properties of Diamond: A Data Handbook*. Berlin, Heidelberg: Springer Berlin Heidelberg, 2001, pp. 389–393. ISBN: 978-3-662-04548-0. DOI: 10.1007/978-3-662-04548-0_7. URL: https://doi.org/10.1007/978-3-662-04548-0_7.

[109] Xiaohua Zhang et al. "Pressure-induced hydride superconductors above 200 K". In: *Matter and Radiation at Extremes* 6.6 (2021), p. 068201.

[110] Xin-Yue Zhang et al. "AC susceptometry of 2D van der Waals magnets enabled by the coherent control of quantum sensors". In: *PRX Quantum* 2.3 (2021), p. 030352.

[111] Xiaobo Zhu et al. "Observation of dark states in a superconductor diamond quantum hybrid system". In: *Nature Communications* 5 (Apr. 2014), p. 3424.

[112] James F. Ziegler, M.D. Ziegler, and J.P. Biersack. "SRIM – The stopping and range of ions in matter (2010)". In: *Nuclear Instruments and Methods in Physics Research Section B: Beam Interactions with Materials and Atoms* 268.11 (2010). 19th International Conference on Ion Beam Analysis, pp. 1818–1823. ISSN: 0168-583X. DOI: https://doi.org/10.1016/j.nimb.2010.02.091. URL: https://www.sciencedirect.com/science/article/pii/S0168583X10001862.